MICRO-STRUCTURES, MINERALOGY, AND CHEMISTRY OF PERITIDAL TUFA STROMATOLITES ALONG THE EASTERN CAPE COAST

M.J.K. Edwards

2019

MICRO-STRUCTURES, MINERALOGY, AND CHEMISTRY OF PERITIDAL TUFA STROMATOLITES ALONG THE EASTERN CAPE COAST

By

Mark Joseph Kalahari Edwards

Submitted in fulfilment of the requirements for the degree of

Master of Science

at

Nelson Mandela University

Apr 2019

Supervisor: Mr C.R. Anderson

Co-supervisors: Prof. R. Perissinotto & Dr. G.M. Rishworth

DECLARATION – PLAGIARISM

I, Mark Joseph Kalahari Edwards (student number: 212457365), hereby declare that, in accordance with Rule G5.6.3 of Nelson Mandela University, the dissertation for the degree of Master of Science entitled, "Micro-structures, mineralogy and chemistry of peritidal tufa stromatolites along the Eastern Cape coast, South Africa", is my own work and that it has not previously been submitted for assessment to another university or for another qualification.

At no point in this dissertation is another person's text, data, graphs or figures presented, unless these have been suitably acknowledged and credited to the other person.

Signed: ……

MJK Edwards

20 March 2019

Rule G5.6.3,

5.6.3 A treatise/dissertation/thesis must be accompanied by a written declaration on the part of the candidate to the effect that it is his/her own work and that it has not previously been submitted for assessment to another University or for another qualification. However, material from publications by the candidate may be embodied in a treatise/dissertation/thesis.

Table of contents

Declaration i
Stucuture of this MSc 5
Chapter 1 - Micro-structures and mineralogy of peritidal tufa microbialites along the Eastern Cape coast of South Africa
1. Introduction 7
2. Materials and methods 8
2.1 Study area 8
2.2 Geological and hydrological setting 9
2.3 Sample collection and preparation 10
2.4 Descriptive analysis and classification 11
3. Results 12
3.1 XRD analysis 12
3.2 Thin sections 13
3.3 Scanning electron microscopy 25
4. Discussion 35
4.1 Thin section analysis 35
4.2 Mineralogy and crystal morphology 38
4.3 Comparison to similar deposits 41
5. Conclusion 42
Chapter 2 - Geochemical characterisation of the peritidal tufa microbialites near Port Elizabeth, South Africa
1. Introduction 45
2. Materials and methods 46
2.1 Study area 46
2.2 Sample collection 47
2.3 Sample preparation and analysis 49
3. Results 50
3.1 Bulk rock major and trace elements 50
3.2 SEM/EDS 53
4. Discussion 58
4.1 Geochemical variation 58
4.2 Rock and water chemistry 66
4.3 Similar deposits 71
5. Conclusion 74
General conclutions and future work 76
References 79
Apendices 7985

List of Figures

Chapter 1

Fig. 1.1 Map indicating the three study sites along the Eastern Cape coast 9
Fig. 1.2 Thin section images of the various textures of waterfall deposits 16
Fig. 1.3 Thin section image of a rhizolith sample. 17
Fig. 1.4 Typical variation in grain size, sorting, and cement of beachrock samples. 20
Fig. 1.5 Thin section image of a beachrock sample. 19
Fig. 1.6 Thin section images of the various textures of beachrock 20
Fig. 1.7 Thin section images of the various textures of discharge aprons 21
Fig. 1.8 Thin section images of the various textures of barrage pools. 23
Fig. 1.9 SEM micrographs of the various meso-fabrics at the micro scale. 27
Fig. 1.10 SEM micrographs of the micro- nano-textures observed in each sample 28
Fig. 1.11 Crystal forms found within waterfall and beachrock tufa samples. 31
Fig. 1.12 SEM micrographs of the various micro-structures in colloform tufa 32
Fig. 1.13 various micro-fabrics of the tufa samples 33
Fig. 1.14 SEM micrographs of the various barrage pool crystal morphologies 34
Fig. 1.15 Diagram of the various needle-fibre calcite morpholofies 40

Chapter 2

Fig. 2.1 Map indicating the three study sites along the Eastern Cape coast 47
Fig. 2.2 Micrographs showing typical areas of analysis by SEM/EDS 54
Fig. 2.3 Micrographs of the various inclusions analysed by SEM/EDS 57
Fig. 2.4 Scatter plots of the major elements versus Al_2O_3 60
Fig. 2.5 Scatter plots of selected major and trace elements versus Al_2O_3 63
Fig. 2.6 Major and trace element patterns relative to PAAS 65
Fig. 2.7 Rare Earth Element patterns relative to PAAS 66
Fig. 2.8 Molar ratios of Mg, Sr, and Na to Ca compared to molar ratios of Forbes et al. (2010) 73

List of Tables

Chapter 1

Table 1.1 Bulk rock mineral analysis of tufa samples by XRD 12
Table 1.2 Summary of the thin section results for comparative purposes..... 14
Table 1.3 SEM micrograph analysis of tufa samples: a summary. 26

Chapter 2

Table 2.1 A summary of the samples collected and used for bulk rock major elemental analyses 48
Table 2.2 An overview of the tufa samples collected and used for SEM/EDS analysis 48
Table 2.3 Analysis of the major elements in tufa samples 51
Table 2.4 Trace element analysis of the tufa deposits 52
Table 2.5 SEM/EDS analysis of the carbonate matrix of tufa samples..... 55
Table 2.6 SEM/EDS analysis of the inclusions observed in tufa samples 56
Table 2.7 Molar ratios and identified mineral inclusions of SEM/EDS data 61
Table 2.8 Molar ratios of the carbonate matrix as identified by SEM/EDS. 68
Table 2.9 Molar ratios of elements identified by bulk rock XRF 69

Acknowledgments

Thank you to Callum Anderson, Nelson Mandela University (NMU), for his supervision, knowledge, and expertise in the geological field during this post graduate research. I would also like to thank my co-supervisors, Dr Gavin M. Rishworth and Prof. Renzo Perissinotto for their crucial input and support. Prof. Perissinotto is further thanked for his role in awarding me the research grant, provided by the Department of Science and Technology (DST) through the National Research Foundation (NRF), which funded this project. The DST/NRF (Grant UID: 84375) and NMU (Nelson Mandela Postgraduate Research Scholarship) are thanked for funding awarded to me that allowed the completion of this dissertation. The Centre for High Resolution Transmission Electron Microscopy (CHRTEM) at NMU, the Stellenbosch University Central Analytical Facilities, and the NMU Chemistry Department are thanked for all their assistance with the various analytical techniques carried out in this study.

I am grateful to all those who assisted me throughout this scientific journey, in the field and in the laboratory. These include my three supervisors as well as Richard Campbell, David Moorcroft and Antonia Liber. I would especially like to thank Willie Deysel for his constant assistance in sample preparation in the rock lab, Xandri van Niekerk for her expertise in XRD interpretation and William Goosen for his knowledge and skill regarding SEM analyses. Dr Gavin M. Rishworth is again thanked for his guidance through this research, especially for his input in drafting the dissertation. I am also extremely grateful to my family members for their backing and reassurance during my time at University. Thank you to my father, Lloyd Edwards, for guiding me toward science and through life as well as his essential contribution to my university career. To my mother, Penny Elliott, for her love, motivation, limitless support and for providing me with everything I needed to achieve my goal.

Abstract

Peritidal tufa microbialites occurring along the coast near Port Elizabeth, South Africa have been investigated from multiple disciplines and are found to be similar to supratidal tufa deposits in South West Australia. Studies have been conducted on the biological factors, geomorphology, ecosystems, and associated water chemistry. However, to date no mineralogical, micro-fabric, or geochemical analyses have been reported on these tufa deposits. This work, carried out at a previously well-studied area, provides the first study of this kind on the tufa. Chapter 1 is a mineralogical and micro-fabric analysis of the tufa deposits near Port Elizabeth for the purpose of classification and contextualisation. Chapter 2 provides the first geochemical study of these peritidal microbialites.

X-Ray diffraction (XRD) investigations reveal dominance of low-Mg calcite in the mineral make-up of the tufa. A micro-structure analysis via thin section exposes a number of fabrics, suggesting various micro-facies: phytoherm boundstone (layered), phytoherm framestone (non-layered), lithoclast, and minor metazoan tufa. Scanning electron microscopy (SEM) images show micro- to nano- scale variation in calcite grains and epitaxial forms of needle-fibre calcite (NFC). The elemental composition of the tufa deposits were examined by X-ray fluorescence (XRF), Laser Ablation Inductively Coupled Plasma Mass Spectrometry (LA-ICP-MS), and Scanning Electron Microscopy / Energy Dispersive X-Ray Spectroscopy (SEM/EDS).

XRF and LA-ICP-MS were used to analyse the bulk rock chemistry while SEM/EDS was used to scrutinize specific areas within the tufa. These observations suggest the deposits are better classified as tufa microbialites (rather than exclusively “stromatolites”) and outline similarities and disparities to the micro-fabrics of supratidal tufa deposits in South West Australia, and Cape Morgan, South Africa. Here the Port Elizabeth tufa is shown to be similar, in terms of the dominant elements (O, Ca and to a lesser extent, Mg and Sr), to the Australian deposits despite subtle dissimilarities in water chemistry. Increasing trends toward more marine tufa for many elements are also shown here and can be explained by the interaction with increased amounts of sedimentary products and/or interactions with more saline water that contains a higher TDS (Total Dissolved Salts). This is also the first study to report needle-fibre calcite formation in stromatolites and the first to geochemically analyse modern peritidal microbialites

Key words: microbialites, tufa, micro-fabric, bacterial filaments, needle-fibre calcite, geochemistry, trace elements, rare earth elements

General Introduction

Microbialites, or microbial carbonates, are widespread deposits that result from microbially mediated carbonate precipitation (Burne and Moore, 1987). They are often categorised into two main types based on their micro-fabrics; laminated types are termed stromatolites while clotted types are called thrombolites (Riding, 2000). Tufa stromatolites are defined as macroscopically layered authigenic microbial sediments that may or may not contain interlayered abiogenic precipitates (Riding, 2000). These deposits develop in freshwater and marine environments where calcium carbonate saturation is reached (Smith et al., 2011). Stromatolites often form domical or columnar meso-structures as they grow and have been documented as having a variety of internal micro-structures (Riding, 2011). Micro-fabrics are extremely important in the interpretation of stromatolite-forming processes (Riding, 2011). There are three principal types of stromatolite fabrics, namely sparry crust, fine grained crust, and hybrid crust. They are interpreted to be abiogenic, biogenic, and mixed respectively (Riding, 2011). These stromatolite fabrics are known to form in calcitic tufa deposits (e.g. Forbes et al., 2010). Tufa deposits are organic and/or inorganic deposits that form under open air conditions in cool freshwater, which can be permanently or periodically saturated with respect to calcite (Kano et al., 2003).

Actively calcifying tufa microbialites have been documented on the Eastern Cape coast of South Africa near Port Elizabeth (e.g. Perissinotto et al., 2014; Rishworth et al., 2016a; Rishworth et al., 2017; Edwards et al., 2017). These deposits form at the interface between freshwater seeps and marine penetration (Perissinotto et al., 2014). The stromatolites are located in the supratidal to upper intertidal zones, and as a result receive seawater inflow through wave overtopping at spring high tide or wave splash during storm events (Perissinotto et al., 2014). They contain finely layered carbonates precipitated via microbial mediation, leading to their classification as “tufa stromatolites” (Rishworth et al., 2016a; Smith et al., 2011; Riding, 2000). The carbonate precipitation occuring here has been shown to be influenced by physicochemical, hydrochemical, thermodynamical, and nutritional parameters (Dodd et al., 2018). The deposits along the Eastern Cape coast have been regarded as unique in their nature, due to their occurrence at the interface between fresh and marine water.

The precipitation of carbonate in tufa deposits, related to the agency of cyanobacteria, algae, mosses, plants and/or detritus, produces a range of crystal forms (Forbes et al., 2010). Perri et al. (2012) examined stromatolites near Marion Lake in South Australia and found that a micrite/microsparite crystal fabric characterises the fine-grained, well-laminated stromatolites. The microfabric of the extremely fine layers was made up of a peloidal texture, with abundant, finer aphanitic layers. The peloids and aphanitic micrite were coated in spherulitic and acicular microspar respectively, with the spherulite nuclei and the aphanitic layers being composed of coalescing nanospheres, which develop into low-Mg calcite polyhedrons (Perri et al., 2012). This micrite/sparite micro-fabric is common in tufa deposits and has been associated with changing physico-chemical conditions (e.g. Forbes et al., 2010; Kazmierczak et al., 2015).

Two types of layering were observed in the peritidal stromatolites at Cape Morgan (Eastern Cape, South Africa) by Smith et al. (2005), which are located approximately 150 km east of those near Port Elizabeth. The pioneer laminae (type 1) comprise a thicker layer made up of tightly packed vertical filaments, often arranged in a radial fashion. The climax laminae (known as type 2) cap pioneer laminae and consist of cyanophyte filaments. Type 2 layers often bind and trap diatoms and sedimentary grains (Smith et al., 2005; Reid, et al., 2000). Type 1 laminae are lighter in colour and are characterised by rapid vertical filament growth. Type 2 are thinner and darker and reflect slower horizontal growth (Smith and Uken, 2003; Smith et al., 2011). These alternating layers and fabrics may reflect the climatic variability in an area (Pedley et al., 1996). A hybrid layer, known as type 3, can also form if the hiatus in sediment accretion of type 2 mats continues over a long period. Type 3 laminae are categorized by an abundance of endolithic coccoid cyanobacteria (Baumgartner et al., 2009).

Baumgartner et al. (2009) found that the number of microbial species increases during transition from type 1 through to type 3 communities, which supports the idea that these layers reflect different stages of stromatolite development. Kawai et al. (2009) related the development of the different layers to seasonal changes in the precipitation rate of calcite (PWP; as defined by Plummer et al., 1978) and calcite packing-density (CPD). Type 1 laminae, characterized by cyanobacteria dominant growth, form well in autumn and summer while type 2 mats develop strongest in winter and spring. Seasonal changes in PWP

and CPD often enhance the porous/dense contrast of tufa deposits (Baumgartner et al., 2009).

It has been suggested that an understanding of the chemical and physical factors involved in the development of modern stromatolite formations may help improve geological reconstructions of their ancient counterparts. Smith et al. (2011), for example, found strong morphological similarities between modern tufa stromatolite facies at Cape Morgan and ancient marine stromatolites at Strelley Pool in Australia. Ancient stromatolites occurred as far back as the Archean (Hofman et al., 1999) and thrived in the Precambrian oceans (Riding, 2006) but are scarce in the Phanerozoic rock record (Mata and Bottjer, 2012). This decline is often explained by the decrease in the concentration of calcium carbonate in ocean waters (Grotzinger, 1990) and competition introduced by eukaryotic algae and metazoans (Bernhard et al., 2013; Riding, 2011). Major and trace elements have been used to infer depositional environments of ancient (Archean and Proterozoic) stromatolites (Bolhar and Van Kranendonk, 2007; Frimmel, 2009). Concentration of Rare Earth Elements (REE) and their spider diagram patterns are commonly used to infer water conditions of the ancient deposits (e.g Chagas et al., 2016; Frimmel, 2009). The micro- and nano-scale mineral fabrics of stromatolites may also hold key information regarding the role that organisms had on mat forming processes (Benzerara, et al., 2010; Spadafora et al., 2010; Perri et al., 2012). Therefore, identifying and describing these chemical components and mineral fabrics in the South African peritidal tufa stromatolites, for the purpose of characterisation and contextualisation, is the aim of this project.

Stucuture of this MSc

This dissertation includes two chapters of original work which each will be submitted for peer review as standalone manuscripts. Chapter 1 deals with micro-strcutures and mineralogy and Chapter 2 with the geochemistry of the peritidal tufa stromatolites found near Port Elizabeth. The significant findings and the context thereof are then tied together in a General Conclusion chapter. Given the format of this dissertation, there is some overlap between chapters, although this has been minimised wherever possible.

Chapter 1

Micro-structures and mineralogy of peritidal tufa microbialites along the Eastern Cape coast of South Africa

1. Introduction

Calcareous spring deposits of biogenic and abiogenic origin are widely reported and are often classified based on their internal texture, components, and geochemical attributes (Jones and Renaut, 2010). Biogenic precipitates formed with the aid of benthic microbial communities are known as microbialites, and are categorised into two types, namely, stromatolites and thrombolites (Riding, 2011). Thrombolites have a clotted and non-laminated internal fabric (Aitken, 1967), while stromatolites are macroscopically layered (Riding, 2000). Autochthonous (precipitated in situ) tufa deposits are classified in a similar fashion. Laminated phytoherm tufa deposits are known as boundstone, while non-laminated phytoherm tufa is classified as framestone tufa (reef-like framework) or microherm tufa (shrubby framework). Allochthonous (precipitated elsewhere) types of tufa are classified on the basis of their texture and organic/inorganic constituents (Ford and Pedley, 1996). Therefore, describing and identifying the internal micro-fabric of microbialites is required for their classification.

The mineralogy of microbialite deposits is a result of a complex interplay of physical, chemical and biogenic factors, such as microbial influence, growth inhibitors, and water chemistry (Jones and Renaut, 2010). A large variety of crystal morphologies, from micrite (calcite grains < 4 μm) to large palisade crystal beds and dendrite crystals, are associated with carbonate precipitation in spring systems (Jones and Renaut, 2010). Microbialites are often associated with fine-grained (micritic) and/or fibrous (sparitic) micro-fabrics (e.g. Riding 2000). The sparitic fabrics often consist of aragonite or bladed calcite whereas the micritic layers are commonly composed of low-Mg calcite (e.g. Kazmierczak et al., 2015; Pedley, 1992; Leybourne et al., 2009). The mineralogy and the micro- to nano-scale fabrics can provide information on the influence of microbes, as well as the chemical and physical factors involved in microbialite accretion (Benzerara et al., 2010). This is due to crystal precipitation being affected by varying physical, chemical, and bacterial conditions (e.g. Azulay et al., 2018; Cailleau et al., 2009; Janssen et al., 1999).

Active biogenic tufa deposits, forming at the interface between spring and marine water, near Port Elizabeth in the Eastern Cape (South Africa) have been classified based on their macro and meso structures (Edwards et al., 2017). In order to expand on this work, this

chapter focuses on structural and mineralogical features of the tufa deposits at a micro- to nano-scale. Such features are identified, described and analyzed using X-ray diffraction (XRD), thin section analysis, and scanning electron microscopy (SEM). The results of these analyses are used to classify these deposits and compare them to similar deposits such as those of South-Western Australia (Forbes et al., 2010) and Cape Morgan, South Africa (Smith et al., 2011).

2. Materials and methods

2.1 Study area

The study area, along the Eastern Cape coast of South Africa, occurs on the south west of Port Elizabeth (Fig. 1.1). Three sites previously studied by Edwards et al. (2017) were selected for this study as they include all macro-scale tufa variations that occur in the area. These sites are known as Schoenmakerskop (site B1), Seaview (site C2), and Laurie's Bay (site D). As these sites have some morphological variation with elevation above sea level (Edwards et al., 2017), samples were collected from various heights along each site's profile. The elevation profile of the tufa system was split into three categories based on the level of seep water and marine water mixing. The first is dominated by fresh water (upper, ~ 2 m), the second by mixed water (intermediate, ~ 1 – 2 m), and the third by marine water (lower, < 1 m). Measurements were taken from average mean sea level.

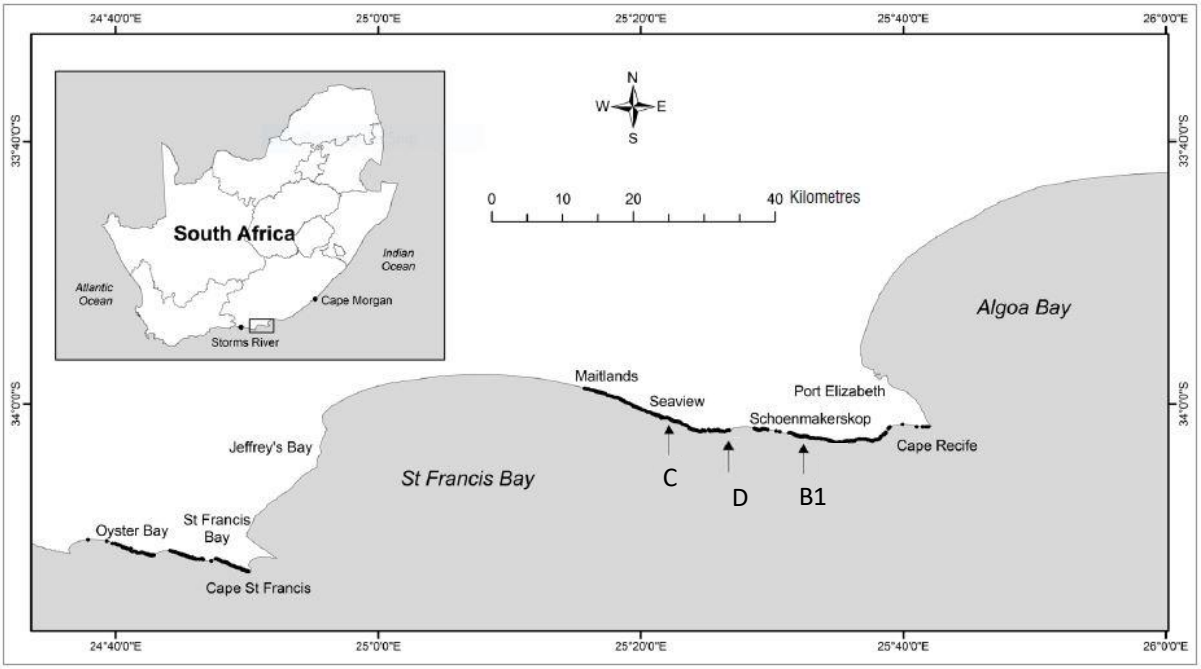

Fig. 1.1 Map indicating the three study sites along the Eastern Cape coast. Black points along the coast represent known tufa stromatolite colonies (after Perissinotto et al., 2014).

2.2 Geological and hydrological setting

The underlying geology of the study area is typified by shore platforms consisting of metasediments from the Palaeozoic Cape Supergroup at sites B and D (Council for Geoscience, 2000a, 2000b) and the Pre-Cape Gamtoos Group at site C (Council for Geoscience, 2000a). Unconformably overlying the bedrock are formations of the calcareous Cenozoic Algoa Group. Bordering the coastline of sites B and D are aeolianites of the middle to late Pleistocene Nahoon Formation (Council for Geoscience, 2000a, 2000b). These aeolianites also occur to the west of site C. Unconsolidated aeolian sands of the Holocene Schelm Hoek Formation occur inland of the study area (Council for Geoscience, 2000a, 2000b); they can stretch up to 6 km inland and have a thickness of up to 140 m (le Roux, 1989). Semi- to well-consolidated aeolian deposits of the late Pliocene to early Pleistocene Nanaga Formation occur further inland and most likely beneath parts of the Schelm Hoek Formation (le Roux, 1989).

The tufa stromatolite colonies have formed on the southern coastline where groundwater seeps flow from or near the base of the aeolian or beach deposits. Dodd et al. (2018) have shown that this groundwater, influenced by the coastal sands, has an enriched Ca/Mg HCO_3^-

component. The groundwater seep is enriched in carbonate due to its interaction with the lime rich Cenozoic deposits of the Algoa Group (Dodd et al., 2018). This high energy coastline has semi-diurnal tidal shifts of 0.5 m at neap tide and 1.8 m at spring tide (Schumann and Perrins, 1982). The spring tide shifts have been recorded to have a range of up to 2 m on occasion (Schumann, 2013).

2.3 Sample collection and preparation

Samples (n = 40) of active and inactive tufa were collected from three study sites along the coast (Fig. 1.1), between May 2016 and April 2018. Two samples that were previously collected in 2014 for a separate study were also analysed. Actively growing microbialite as well as inactive material was used for XRD analysis, while only inactive samples were used for thin section and SEM analyses. This is due to the active samples being too soft and friable to cut and grind accurately. Samples (n = 24) were dried and cut in order to reveal the internal fabric. Internal fabrics which displayed features of particular interest were then selected for petrographic examination. As these samples were friable, they were first impregnated with resin and then cut into flat sections that were used for making thin sections. A further eleven samples were cut into small blocks and coated with a conductive material for imaging via Scanning Electron Microscopy (SEM). Samples used for XRD (n = 8) were crushed and ground into a fine powder using a pestle and mortar. Approximately 5-10 g of each powdered sample was pressed into discs for XRD analysis for mineralogical identification.

During the initial sample preparation for SEM analyses a number of issues arose. The samples, intended for imaging, were prepared by breaking a piece (1 – 2 cm in length and ~ 1 cm in width and height) off the larger hand sample. Compressed air was then used to clean the samples of any loose particles. These samples were then coated with carbon, on the newly exposed surface, to allow for conduction. The first issue with these samples was that the vacuum required to run the SEM took a substantial amount of time to achieve, due to the high porosity of the samples. Another issue was that the samples were still not conductive enough to allow for high magnification imaging. In order to overcome these issues, much smaller pieces (<0.5 cm^3) were broken or cut from the hand samples, cleaned with compressed air, and then coated with gold to allow for better conduction. These

samples displayed significantly less charging at the surface and the SEM was able to reach the required vacuum at a normal rate. Overall, 10 samples were prepared for SEM imaging.

2.4 Descriptive analysis and classification

All thin section and SEM observations were compared to peer-reviewed publications. Thin section descriptions are based on the revised classification system by Jones and Renaut (2010), originally compiled by Ford and Pedley (1996). All thin section and SEM analyses are described in terms of their macro- (waterfall deposits, beachrock/conglomerate, discharge aprons, and barrage pools) and meso-structures (wrinkled laminar, laminar flat, pustular/colloform, rimstone, and columnar). For SEM analyses, the description of the various calcite morphologies is based on the model of Cailleau et al. (2009). This model divides needle-fibre calcite (NFC) into three groups: Serrated-edged types, Smooth types, and Complex types. Each group can be further divided into various types based on their three-dimensional morphology.

3. Results

3.1 XRD analysis

The results of the powdered X-Ray diffraction spectrometry of the tufa samples are displayed in Table 1.1. All samples were dominated by low-magnesian calcite (87 – 99 %) with minor amounts of halite (< 1.5 %) also present. Vaterite (7.83 %) and gypsum (0 .6 %) were each only present in one sample, XRD7 and XRD5 respectively. Quartz and feldspar are also present in sample XRD6 but do not occur in any other samples. Evaporative minerals (halite & gypsum) may form via evaporation after sample collection, however, halite and gypsum precipitation can also be expected at coastal sites. Therefore, the evaporative mineral readings herein are regarded as part of the bulk rock tufa mineralogy.

Table 1.1 Bulk rock mineral analysis of tufa samples, by XRD, for each study site. All values expressed as weight percent.

Sample	Macro- & Meso-type	Active/ Inactive	Site	Low-Mg Calcite	Halite	Vaterite	Quartz	Feldspar.	Gypsum
XRD1	Waterfall deposit & Wrinkled Laminar	Active	B1	99,32	0,68	-	-	-	-
XRD2	Waterfall deposit & Wrinkled Laminar	Inactive	B1	98,72	1,28	-	-	-	-
XRD3	Discharge Apron & Colloform growth	Active	D	98,81	1,19	-	-	-	-
XRD4	Barrage pool & Laminar flat	Active	D	98,56	1,44	-	-	-	-
XRD5	Barrage pool & Laminar flat	Inactive	D	98,19	1,21	-	-	-	0,6
XRD6	Barrage pool & Rimstone	Active	C2	89,56	1,12	-	7,63	1,69	-
XRD7	Barrage pool & Rimstone	Inactive	C2	91,17	1,00	7,83	-	-	-

3.2 Thin Sections

The thin section analysis shows a range of internal fabrics and micro-structures. Some characteristics, such as the presence of bacterial filaments, are common in all meso-structures. The internal texture and inclusions provide a unique set of characteristics for each meso-fabric (Table 1.2).

Wrinkled laminar deposits contain portions of layered sparry crust but the layering is often disrupted and therefore sectional. Laminar flat and columnar meso-types contain clear and continuous alternating layers of fine grained and sparry crust. Pustular/colloform growth also contains alternating layers but the boundaries are not well defined, leading to a moderately layered deposit. Interestingly, laminar flat growth from pool walls are also moderately layered unlike the laminar flat growth on the discharge aprons. The typical rimstone meso-type is un-layered although occasional sparry and fine grained layers are observed in the highly perforated micro-fabric. Beachrock is capped by alternating sparry and fine grained layers, but made up of shell fragments and quartz grains of varying sizes.

Exemplar sample descriptions are provided here. Waterfall deposits are separated into two types, namely wrinkled laminae deposits and rhizoliths (Edwards et al., 2017). Two samples of wrinkled laminae deposits (WL1 and WL2) and one sample of rhizolith (RH1) were taken from site B1. WL1 (Fig. 1.2A & 1.2B) contains two identifiable textures: fine grained texture with abundant void space and laminated stromatolite-like texture. The laminations observed near the bottom are made up of sparry crust, with alternating density and not alternations of sparry and fine grained crust typical of stromatolites. While both textures contain algal filaments, the laminated fabric contains far more filaments than the fine grained fenestrated tufa. WL2 (Fig. 1.2C & 1.2D) has a similar dual texture; however the boundary and algal filaments are less obvious. Portions of this sample also contain clastic sedimentary grains presumably washed in by rain or storm events. The algal filaments and sedimentary grains are encrusted with fine grained carbonate cement, which is typical of thrombolites (Fig. 1.2D). The sedimentary layer contains sub-rounded quartz grains (< 0.5 mm) and minor elongated shell fragments (< 0.3 mm). There are three distinct types of micro-fabric present in the two samples; laminated sparry and fine grained crust, fenestrated fine grained crust, as well as closely packed tufa cemented sedimentary grains.

Table 1.2 Summary of the thin section analysis for each tufa type found in the study area, for comparative purposes (macro- and meso- types, after Edwards et al., 2017)

Sample	Site	Macro type	Meso type	Texture	Inclusions
1	B1	Waterfall	Wrinkled laminar	Sectional layering, fine grained and sparry	Bacterial filaments
2	B1	Waterfall	Wrinkled laminar	Sectional layering, fine grained and sparry	Bacterial filaments and fine dark material
3*	B1	Waterfall	Rhizolith	Fine grained, no layering	Irregular fenestra, minor shell fragments (< 1 mm) and fine brown material
4	B1	Waterfall	Rhizolith	Fine grained, no layering	Bacterial filaments, sub rounded quartz grains (< 0,5 mm), and minor shell fragments (< 0,5 mm)
5*	B1	Waterfall	Wrinkled laminar	Sectional layering, fine grained and sparry	Bacterial filaments
6*	B1	Waterfall	Wrinkled laminar	Sectional layering, fine grained and sparry	Bacterial filaments, sub rounded quartz grains (< 0,5 mm), and minor shell fragments (< 0,3 mm)
7	B1	Beachrock	Laminar flat	Layered cap of fine grained and sparry crust. Lithiclastic peloidal	Sub rounded quartz grains (< 0,5 mm) and minor shell fragments (< 5 mm)
8	B1	Beach rock	Laminar flat	Layered cap of fine grained and sparry crust. Bioclastic peloidal	Shell fragments (1 - 2 mm), echinoderm spines and minor sub rounded quartz grains (< 0,5 mm)
9*	B1	Beachrock (fine)	Laminar flat	Layered cap of fine grained and sparry crust. Bioclastic peloidal	Irregular and ovoid fenestra, shell fragments (0,5 - 3,0 mm), and sub rounded quartz grains (< 1mm)
10*	B1	Beachrock (coarse)	Laminar flat	Layered cap of fine grained and sparry crust. Litho-bioclastic peloidal	Bacterial filaments, shell fragments (0,5 - 6,0mm) and sub rounded quartz grains (< 1 mm)
11*	B1	Beachrock (fine)	Laminar flat	Layered cap of fine grained and sparry crust. Bioclastic peloidal	Bacterial filaments, shell fragments and an echinoderm spine
12	B1	Beachrock	Laminar flat	Layered cap of fine grained and sparry crust. Bioclastic peloidal	Shell fragments (0,5 - 10 mm), echinoderm spines and minor sub rounded quartz grains (< 1 mm)

Sample	Site	Macro type	Meso type	Texture	Inclusions
13	B1	Beachrock	Laminar flat	Layered cap of fine grained and sparry crust. Litho-bioclastic peloidal	Sub rounded quartz grains (< 0,5 mm) and shell fragments (0,05 - 10 mm)
14*	D	Discharge apron	Colloform	Moderately layered, fine grained and sparry	Bacterial filaments and irregular and elongated fenestra
15*	D	Discharge apron	Columnar	Well layered, fine grained and sparry	Bacterial filaments and irregular and elongated fenestra
16*	D	Discharge apron	Laminar flat	Well layered, fine grained and sparry	Bacterial filaments and irregular and elongated fenestra
17	D	Discharge apron	Colloform	Moderately layered, fine grained and sparry	Bacterial filaments and minor sub rounded quartz grains (< 0,5 mm) and fine dark material
18*	C2	Barrage pool	Colloform	Moderately layered, fine grained and sparry	Bacterial filaments and minor sub rounded quartz grains (< 0,5 mm) and fine dark material
19*	C2	Barrage pool	Rimstone	Sectional layering, fine grained and sparry. Lithoclastic peloidal	Bacterial filaments, Irregular and ovoid fenestra, shell fragments (< 0,5 mm), and minor quartz grains (< 0,5 mm)
20	C2	Barrage pool	Rimstone	Sectional layering, fine grained and sparry	Bacterial filaments, Irregular fenestra, and minor quartz grains (< 0,5 mm)
21	D	Barrage pool	Laminar flat	Moderately layered, fine grained and sparry	Bacterial filaments and minor sub rounded quartz grains (< 0,5 mm) and fine dark material
22*	D	Barrage pool	Laminar flat	Moderately layered, fine grained and sparry	Irregular and elongated fenestra.
23	C2	Barrage pool	Rimstone	Fine grained, no layering. Litho-bioclastic peloidal	Irregular and ovoid fenestra, shell fragments (< 1 mm), and sub rounded quartz grains (< 0,5 mm)
24	C2	Barrage pool	Rimstone	Sectional layering, fine grained and sparry	Bacterial filaments, Irregular fenestra, and minor quartz grains (< 0,5 mm)

***Exemplar samples used herein for full descriptions**

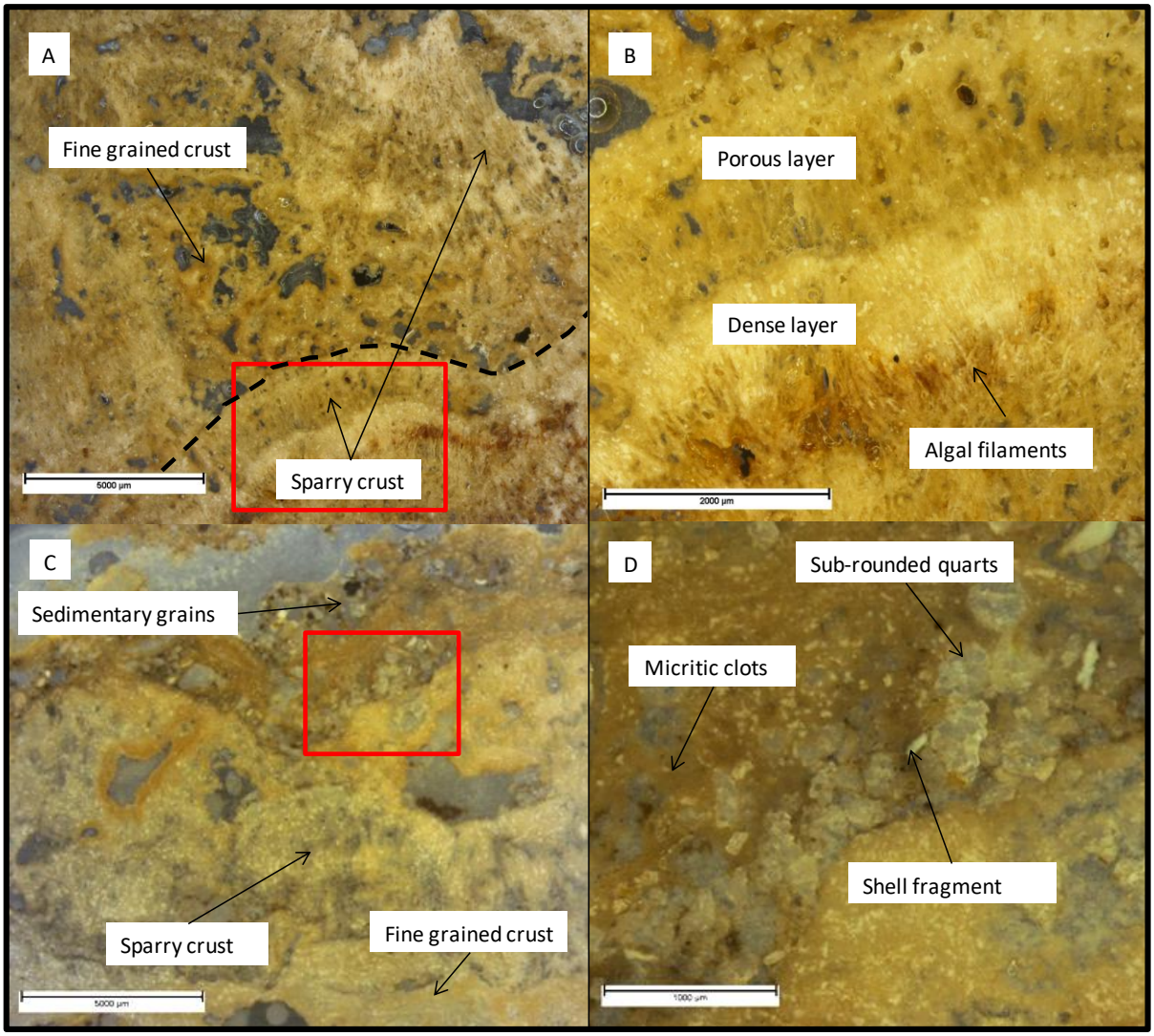

Fig. 1.2 A) waterfall sample (WF1) showing a layered section near the bottom and a thrombolite (non-layered) like texture above. A dotted black line separates the two observed textures. A red rectangle represents the limits of B. B) Sparry crust showing algal filaments within the layers. A densely packed layer underlies a darker porous layer. C) waterfall deposit sample (WF2) showing some sparry crust in the lower half of the image and clotted and grainy texture at the top. The clastic sedimentary grains are likely to be beach or dune material washed in by rain or storm events. D) Close up (red rectangle in C) of the fine grained crust showing a layer of sub-rounded quarts grains and minor shell fragments, occurring between layers of fine grained carbonate with micritic clots.

RH1 contains fine-grained tufa crust, abundant void space, dark brown material and some shell fragments (Fig. 1.3A). Edwards et al. (2017) described the rhizoliths occurring at site B1 as vegetation roots (macrophytes) and other detritus covered in a thin layer of tufa. The void spaces or irregular fenestra seen in Fig. 1.3 are likely formed when the vegetation decays. As a result of vegetation removal, the sample is mostly void space with a thin web of

fine grained tufa. The elongated shell fragments (< 1 mm) and fine brown material are poorly cemented by the tufa and appear within the irregular fenestra (Fig. 1.3B).

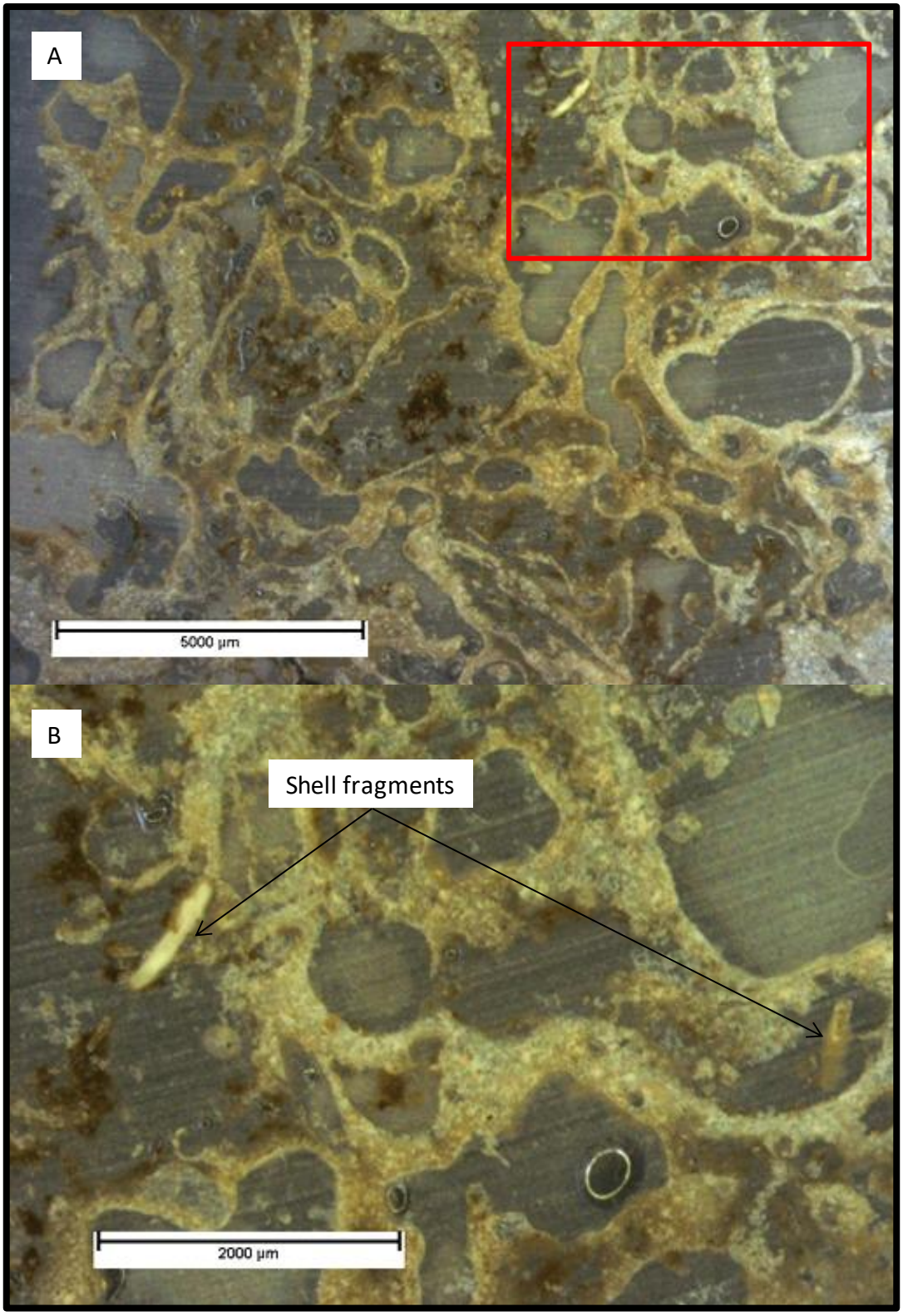

Fig. 1.3 A) Rhizolith sample (RH1) taken from site B1 showing a fenestrated fine grained tufa framework. B) Close up image of the red demarcated area showing shell fragments and fine brown material occurring within the fenestra.

Three beachrock/conglomerate samples (LF1, LF2, and LF3) were examined. The cemented beachrock/conglomerate has a range of clastic grain sizes (Fig. 1.4), which can be lithic or shell derived, and are all capped by carbonate cement (Edwards et al., 2017).

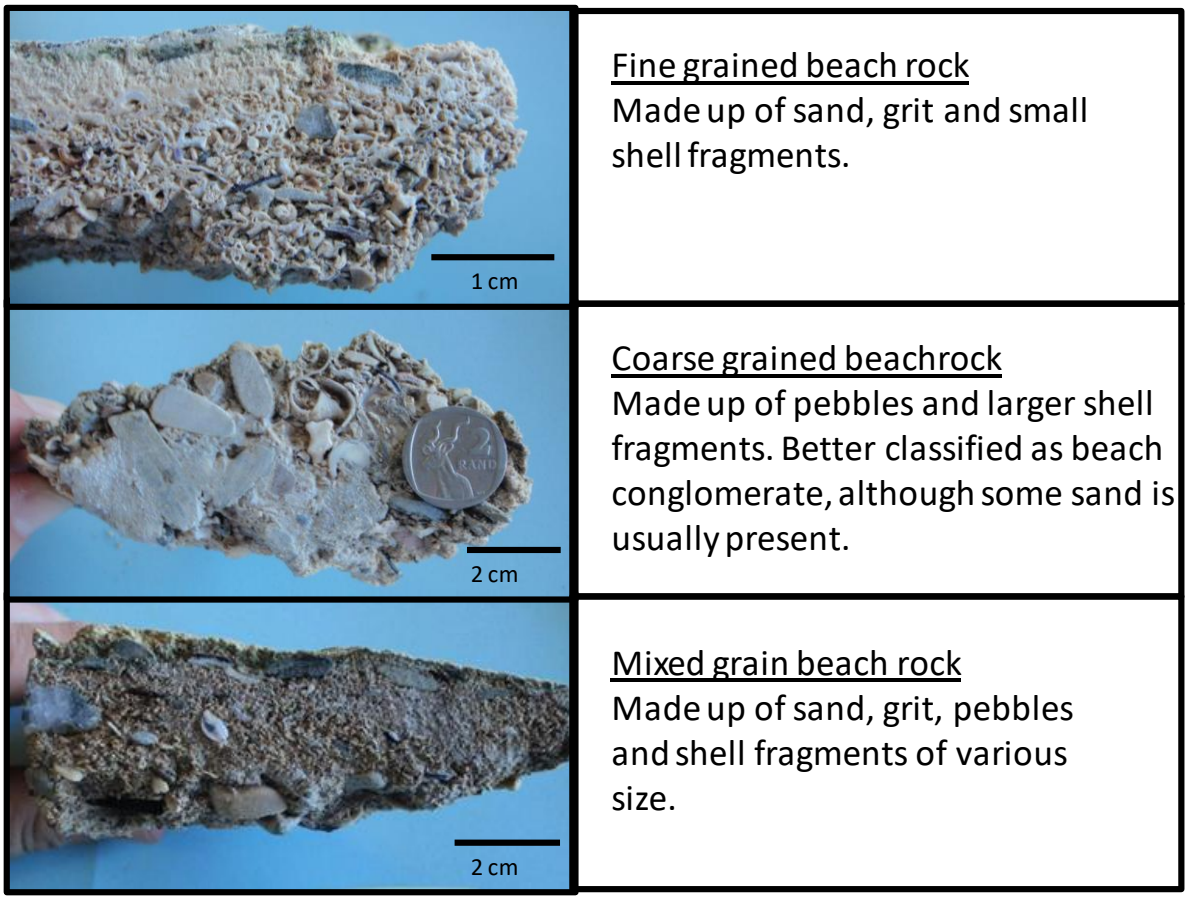

Fig. 1.4 Three beachrock/conglomerate hand samples, taken from site B1, showing the typical variation in grain size, sorting, and the degree of cementation.

LF1 contains abundant bioclasts (shell fragments) and minor quartz grains encased and cemented by fine grained tufa. The shell fragments are elongated, between 0,5 mm and 3,0 mm long and often curved. The quartz grains are sub rounded and < 1 mm in size. The bio- and lithoclasts are held together by tufa cement, forming a bioclastic peloidal texture (Fig. 1.5). Ovoid fenestra are also present in the cemented material and have been coated in a thin (~ 100 µm) layer of microcrystalline tufa. The fine grained tufa encrusting the grains is also observed to contain fenestra but with an irregular shape (Fig. 1.5).

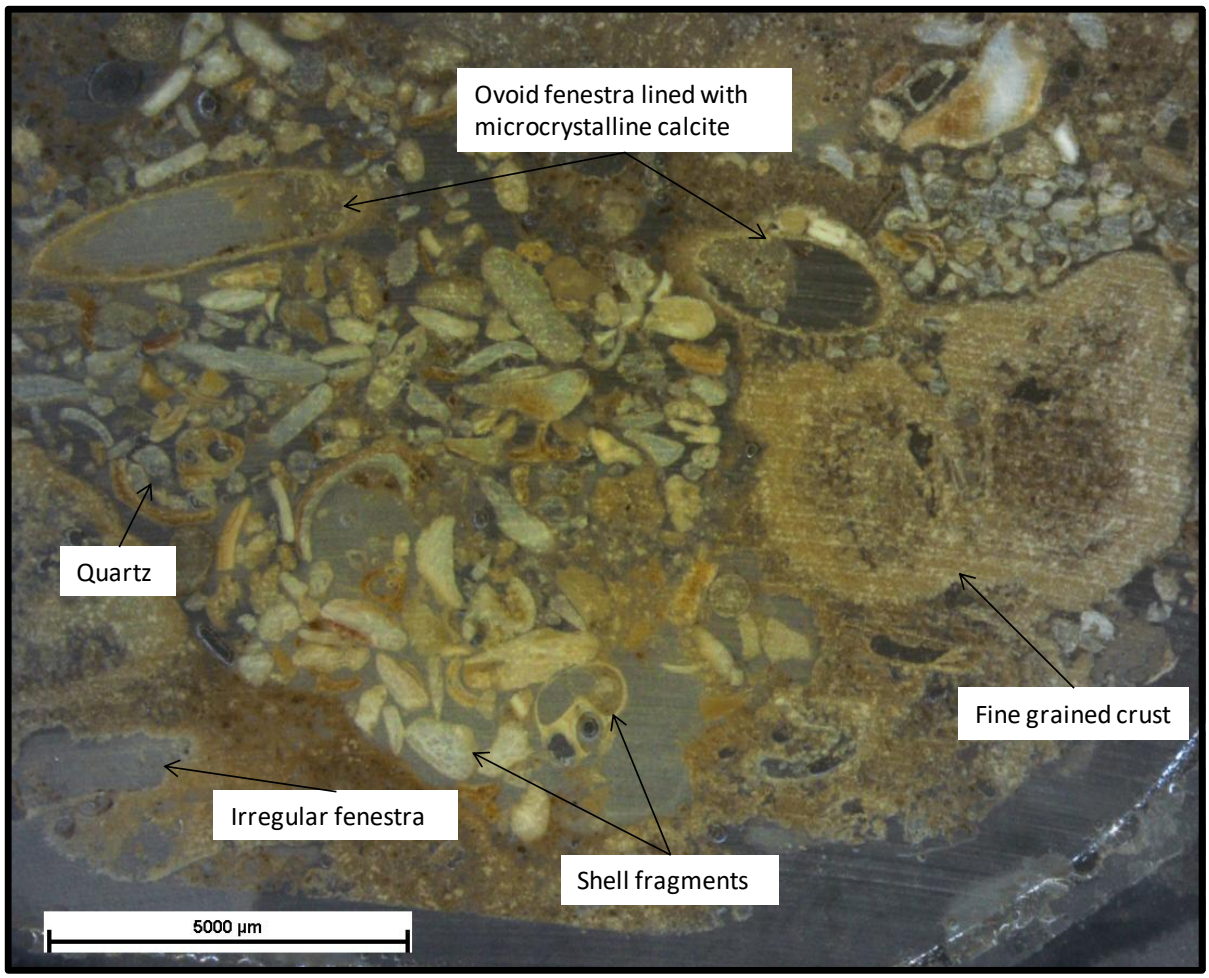

Fig. 1.5 beachrock sample (LF1) showing fine grained tufa surrounding and cementing fine (< 3 mm) shell fragments and minor quartz grains. The surrounding fine grained tufa contains irregular fenestra while the bioclastic centre contains ovoid fenestra.

LF2 contains a fine grained porous layer above a layer of quartz grains and larger shell fragments (Fig. 1.6A & 1.6B). Within the fine grained porous texture is a layered structure that appears lighter and more dense (Fig. 1.6A). The quartz grains are sub rounded and < 1 mm in size while the shell fragments can be > 5 mm in length (Fig. 1.6A). Faint sparry crust is also observed, occurring at the top of the sample above the layered structure (Fig. 1.6B). A similar micro-fabric is observed in LF3 at the top of the sample (Fig. 1.6C). The lower portion of LF3 is made up of tufa-encrusted shell fragments and other bioclasts, such as echinoderm spines of ~ 1 - 2 mm in size. The bioclasts are coated in a thin (< 200 µm thick) layer of fine grained tufa (Fig. 1.6D).

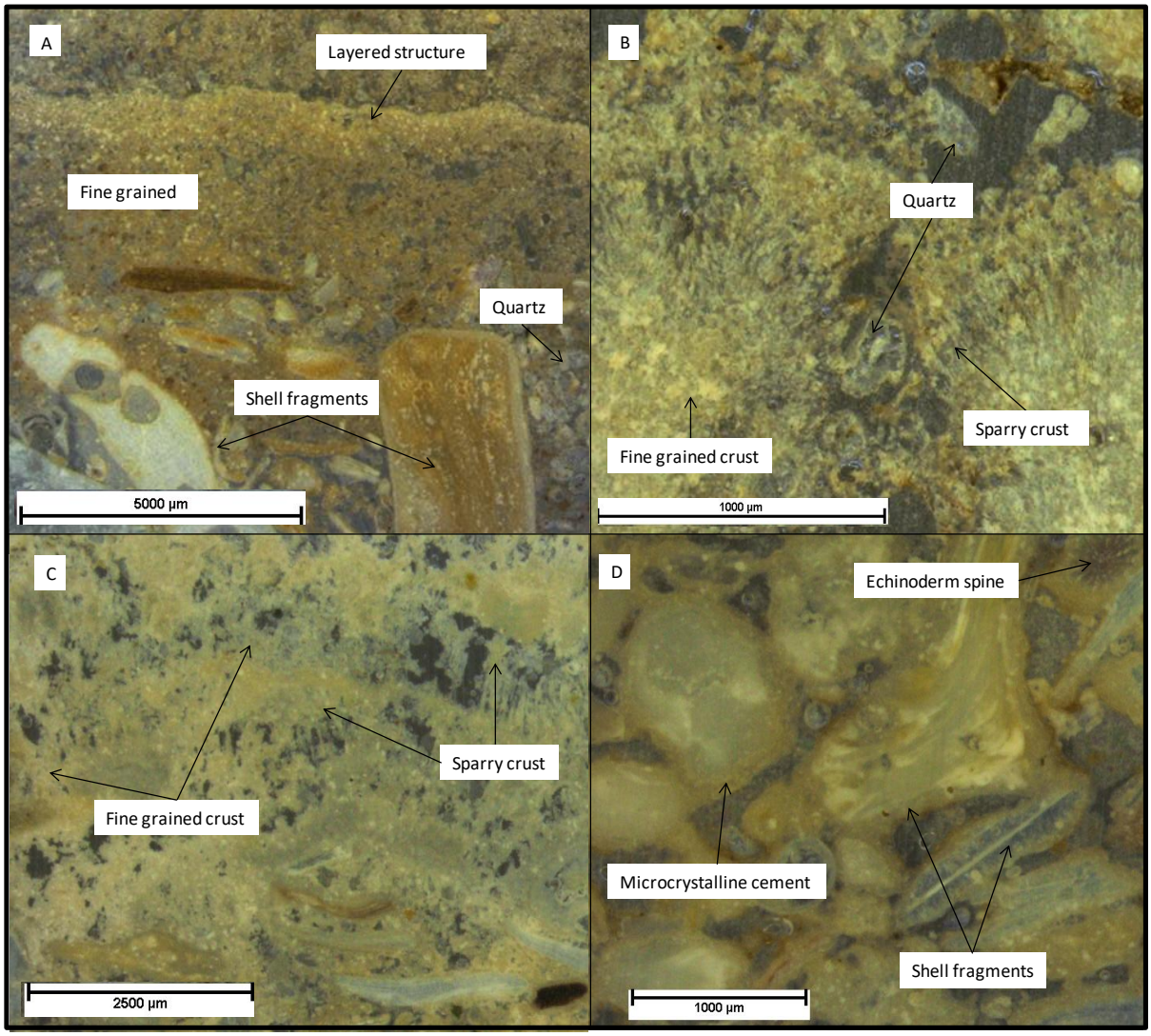

Fig. 1.6 A) Beachrock sample (LF2) showing bimodal texture. A peloidal texture, including larger shell fragments, occurs below a fine grained layered tufa cap. The fine grained section represents the upper most part of the beachrock sample. B) Zoomed in image of the upper most layer of LF2 showing sparry and fine grained crust. C) Beachrock sample (LF3) showing layers of sparry and fine grained crust occurring above tufa cemented shell fragments. D) Close up image of tufa encrusted shell fragments forming a bioclastic peloidal texture.

Three discharge apron samples were examined. Each sample has a different meso-fabric type. Sample CF1 is colloform, sample LF4 is laminar flat, and sample CG1 is columnar (Fig. 1.7). Sample (CG1) was the only example of a columnar meso-fabric found within this study area. Sample CF1 is made up of a bulbous or colloform meso-fabric that is commonly found on discharge aprons (Edwards et al., 2017). The bulbs here are moderately layered and contain alternations of fine-grained crust and porous sparry crust (Fig. 1.7A). Irregular shaped void space is common at the bulb margins and smaller elongated fenestra occur within the sparry crust layers (Fig. 1.7A). The larger fenestra are lined by darker material.

Micritic clots appear throughout the sample but are observed more commonly in fine-grained crust than in the sparry crust (Fig. 1.7A).

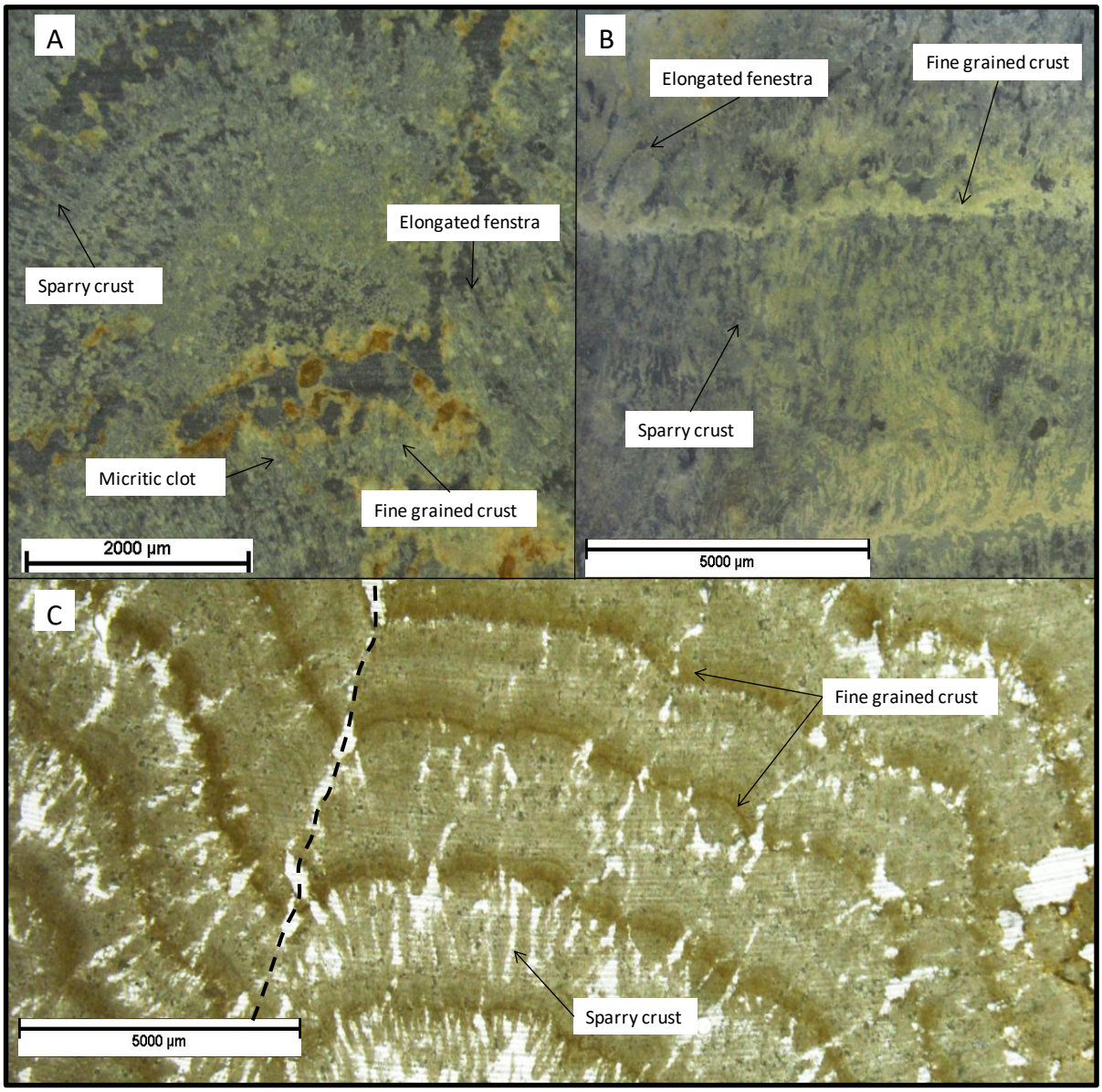

Fig. 1.7 A) Sample CF1 showing bulbous material found on a discharge apron at site D. The bulbs display a sparry crust texture and include sparite and micrite. The micrite becomes more prominent at bulb margins. B) Thin section of laminar flat meso-fabric, commonly found on discharge aprons. Sparry and fine-grained crusts are observed in regular horizontal alternations. C) Thin section image (CG1) of columnar growth showing alternations of sparry and fine grained laminae. Black dashed line represents the limit between two columns.

LF4 shows sparry crust, approximately 6 mm thick, interlayered with thinner (< 0,5 mm) fine-grained tufa. The layering is horizontal and fairly regular (Fig. 1.7B). The sparry layering (type 1) appears more porous than the fine grained crust (type 2). The fine-grained layers have irregular shaped pores while the sparry crust contains elongated fenestra (Fig. 1.7B).

Sample CG1 displays fairly regular alternations of type 1 (sparry) and type 2 (fine-grained) layers (Fig. 1.7C). The sparry layers are lighter and approximately 2 mm thick whereas the fine grained layers are darker and < 0,5 mm thick. The sparry crust also contains elongated fenestra which appear more concentrated in the lower layers (Fig. 1.7C). The fenestra near the bottom of the sample have overlapped and formed a larger irregularly shaped void.

The barrage pools occurring in the study site can be separated into two categories, back pools and front pools (Edwards et al., 2017). The back pools consist mainly of pustular and colloform growth but also exhibit laminar flat lateral growth, whereas the front pools consist of rimstone growth (Edwards et al., 2017). Two samples of back pool growth (CF2 and LF5) and two samples of front pool growth (RS1 and RS2) were examined. CF2 was taken from bulbous growth (pustular and colloform), LF5 was taken from laminar flat growth on the pool wall, and RS1 and RS2 were taken from rimstone growth.

CF2 shows alternations of both types of stromatolite crust, but the layering is disrupted at the top right by sediment (Fig. 1.8A). The fine grained layers are darker, contain abundant micritic clots, and vary in thickness from 0.2 to 1.5 mm. The 2 – 3 mm thick sparry layers are lighter, contain algal filaments and are highly porous (Fig. 1.8A). The sediment at the top right of the sample contains sub-rounded quartz grains and fine dark sediment. LF5 shows horizontal layers of fine grained and sparry crust, although the layering is not as obvious as that typically found in tufa stromatolites (Fig. 1.8B). The fine grained crust is denser, darker and contains micritic clots. The lighter sparry crust contains vertical elongated fenestra and has a thickness of 2 – 3 mm (Fig. 1.8B).

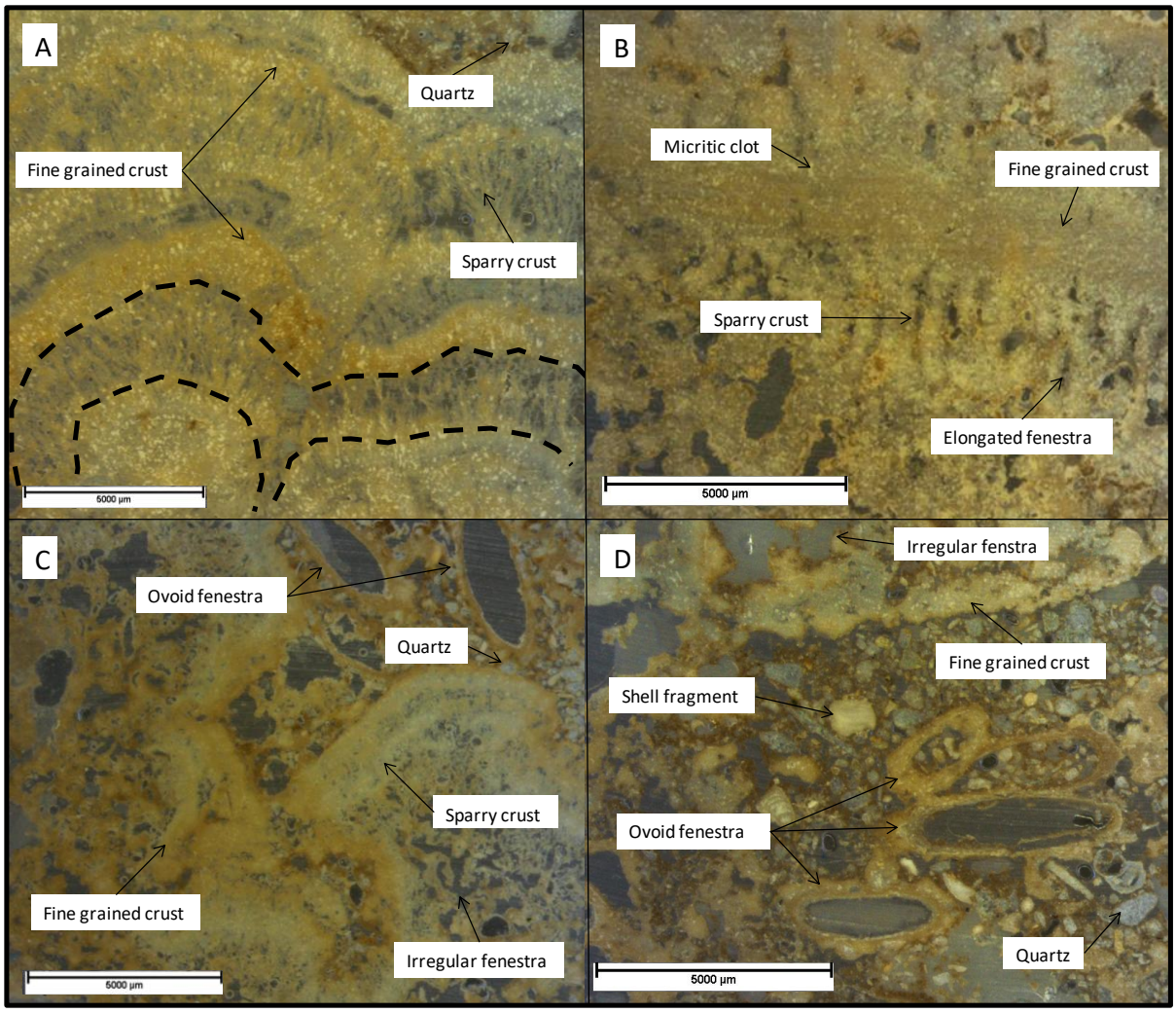

Fig. 1.8 A) Thin section image (CF2) of colloform/pustular growth showing alternations of fine grained and sparry laminae. The dashed black lines represent the upper limits of two layers. B) Thin section image (LF5) showing interlayered sparry and fine grained crust. C) Thin section image (RS1) of rimstone growth showing a layered structure, fenestrated fine grained tufa, and tufa cemented quartz grains and shell fragments. D) Thin section image (RS2) of rimstone growth from site C showing fine grained crust, sections of tufa cemented sediments, and tunnel-like features.

RS1 contains an irregularly shaped layered structure between a highly fenestrated fine grained tufa and tufa cemented sediment (Fig. 1.8C). The layered structure exhibits both sparry and fine grained layers. The void space or fenestra in the fine grained material may be formed by macro-algae and/or burrowing metazoans (e.g. Rishworth et al., 2016b) growing within/on the rimstone. The trapped clastic sediment is made up of sub-rounded quartz grains and shell fragments (< 0.5 mm) that are loosely cemented by minor calcite cement. Ovoid fenestra, lined with microcrystalline calcite, also appear within the trapped sediment (Fig. 1.8C).

RS2 is made up of fine grained crust above cemented quartz grains and shell fragments (Fig. 1.8D). Ovoid fenestra coated with microcrystalline calcite are also observed within the cemented grains and shell fragments of RS2. The sub-rounded quartz grains (< 0.5 mm) and the shell fragments (< 1 mm) are partially cemented by fine grained tufa (Fig. 1.8D).

3.3 Scanning Electron Microscopy

Scanning electron microscopy (SEM) was used to image tufa samples at the micro- and nano-scale. Samples of each macro- and meso- type were selected for SEM analysis. These include wrinkled laminar and rhizoliths on waterfall deposits, laminar flat on beachrock, laminar flat and columnar on discharge aprons, pustular/colloform and laminar flat on back pool, and rimstone on a front pool.

The micro- to nano-scale SEM investigation initially revealed similar textures to those found in thin section (Fig. 1.9). The wrinkled laminar of waterfall deposits, laminar flat beachrock, laminar flat discharge aprons, and columnar growth all contain both sparry crust and fine grained crust (Fig. 1.9A, 1.9C, 1.9E, and 1.9G). Laminar flat discharge aprons and columnar growth show alternations of fine grained and sparry crust, unlike wrinkled laminar and beachrock tufa which show patches of sparry crust and a cap of sparry crust respectively. Rhizolith waterfall deposits and rimstone tufa do not include sparry crust (Fig. 1.9B and 1.9H), however, some filamentous bacterial casts can be found in rimstone (Fig. 1.9H). Colloform growth and laminar flat barrage pool growth samples did not display fine grained layers under SEM, despite the layering being present in thin section (Fig. 1.9D and 1.9F). The samples of colloform growth analysed by SEM display minimal amounts of calcification and bacterial filament surfaces are still clearly visible (Fig. 1.9D).

A closer investigation of the tufa internal fabrics exposes diverse micro-textures from nano-scale micritic grains (~ 200 nm) to micro-scale (1-4 μm long) sparitic needles (Fig. 1.10), identified as needle fibre calcite (NFC). Nanocrystalline calcite coats the bacterial casts found in waterfall deposits with NFC occurring between the coatings (Fig. 1.10A). Rhizolith and beachrock samples are dominated by micrite and do not display any calcite needles, however, some micro-scale plate-like and cubic crystals are also observed in Fig. 1.10 B and Fig. 1.10C respectively. The poorly calcified colloform growth also contains micrite, with no needle-fibres, and calcified diatoms (Fig. 1.10D). Similar to the wrinkled laminar waterfall deposits, laminar flat discharge aprons, laminar flat barrage pools, and columnar growth display both micritic and NFC textures (Fig. 1.10E, 1.10F, and 1.10G). Rimstone tufa, however, is made up of a micritic and meso-crystalline textures, with no needle-fibres observed (Fig. 1.10H)

Table 1.3) SEM micrograph analysis of tufa samples of each type found in the study area : a summary. For macro- and meso- type descriptions, refer to Edwards et al. (2017). Needle fibre calcite is abbreviated here to NFC

Sample	Macro type	Site	Meso type	Textures	Analysis
SEM1	Waterfall	B1	Wrinkled Laminar	Micrite and NFC	Nanocrystalline calcite forming around bacterial filament casts. Needle-like texture formed between casts. Micritic texture associated with none-filamentous areas.
SEM2	Waterfall	B1	Wrinkled Laminar	Micrite and NFC	Nanocrystalline calcite forming around bacterial filament casts. Needle-like texture formed between casts. Micritic texture associated with non-filamentous areas.
SEM3	Waterfall	B1	Rhizolith	Micrite	Micrite formed around roots and vegetation. Variation in crystal grain size and other trapped sediment
SEM4	Beach rock	B1	Laminar flat	Micrite	Nanocrystalline globular and micritic textures with areas of cubic micro-crystals.
SEM5	Discharge Apron	D	Laminar flat	Micrite and NFC	Nanocrystalline calcite forming around bacterial filament casts. Needle-like texture associated with filamentous layers. Micritic texture associated with non-filamentous layers
SEM6	Discharge Apron	D	Columnar	Micrite and NFC	Micritic and NFC “cross-hatch” textures associated with bacterial filament casts. Micritic texture associated with non-filamentous areas. Rare NFC “bridges”.
SEM7	Discharge Apron	D	Columnar	Micrite and NFC	Micritic and NFC “mesh” textures associated with bacterial filament casts. Micritic texture associated with non-filamentous areas. Rare NFC “bridges”.
SEM8	Barrage pool	C2	Colloform	Micrite	Poorly calcified bacterial filaments. Abundant pennate and circular diatoms. Well-formed calcite rhombs appear in mounds.
SEM9	Barrage pool	C2	Colloform	Micrite	Poorly calcified bacterial filaments. Abundant pennate and circular diatoms. Well-formed calcite rhombs appear in mounds. Rare patches of globular texture.
SEM10	Barrage pool	D	Laminar flat	Micrite and NFC	Micritic and NFC textures associated with bacterial filament casts. Micritic texture associated with non-filamentous areas. Rare Inclusions of square plate-like crystals.
SEM11	Barrage pool	C2	Rimstone	Micrite	Micritic and meso-crystalline textures. Rare globular nano- scale grains appear in association with bladed crystal grains.

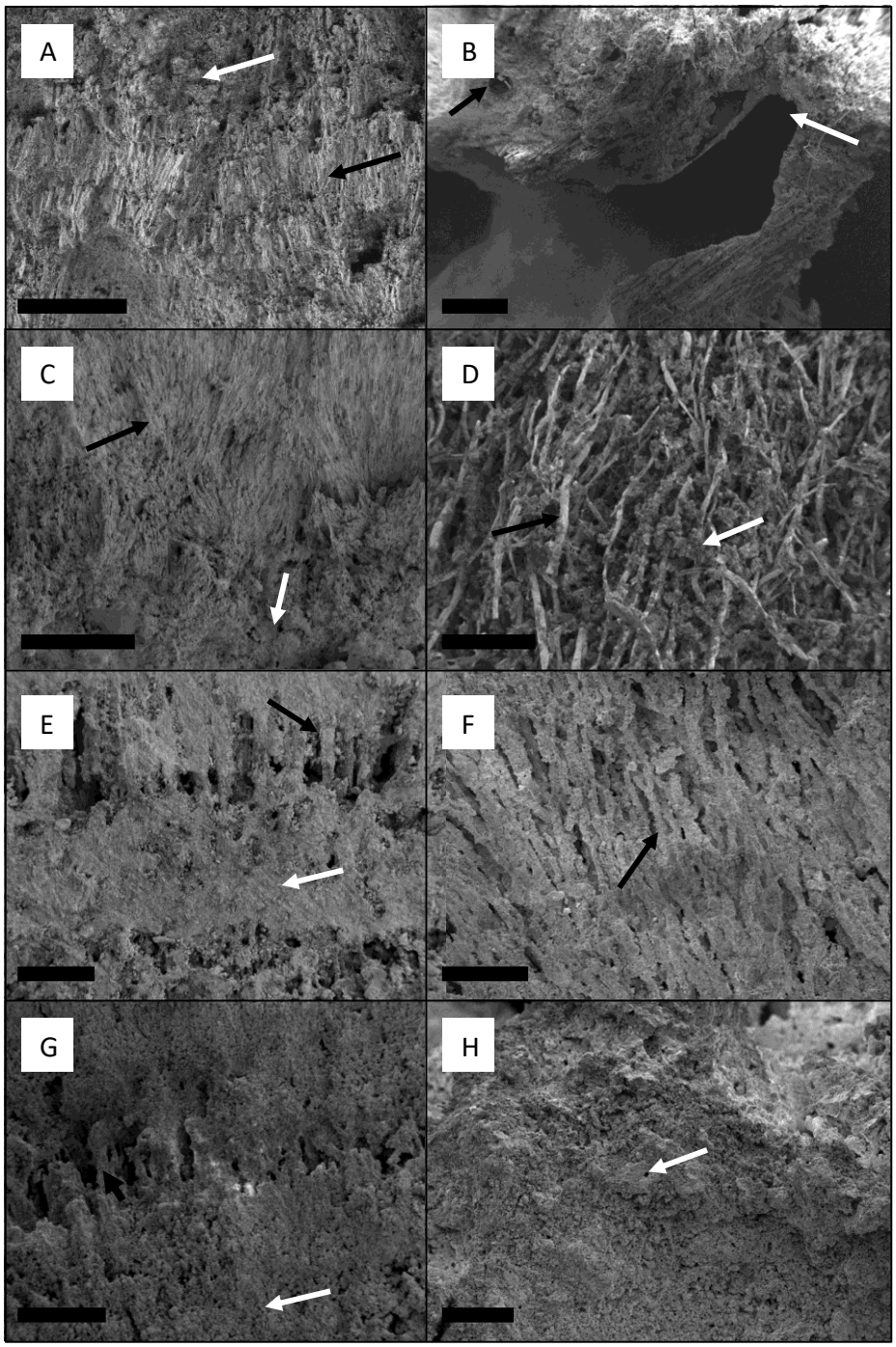

Fig. 1.9 SEM micrographs of the various meso-fabrics at the micro scale. A) Wrinkled laminar from a waterfall deposit showing sparry crust (black arrow) beneath fine grained crust (white arrow); scale bar = 200 µm. B) Rhizolith sample containing tunnel like fenestra (black arrow) and fine phytoclast material (white arrow), within fine grained crust; scale bar = 500 µm. C) Beach rock tufa showing layer of sparry crust overlying a layer of fine grained micrite; scale bar = 500 µm. D) Colloform material made up of bacterial filaments (black arrow) and collections of fine grained calcite (white arrow); scale bar = 500 µm. E) Laminar flat discharge apron sample showing alternations of calcite coated bacterial filaments (black arrow) and fine grained calcite layers (white arrow); scale bar = 500 µm. F) A laminar flat sample taken from a barrage pool wall showing a build-up of calcified bacterial filaments (black arrow) - note there are no fine grained layers; scale bar = 300 µm. G) Columnar growth exhibiting layers of calcite encrusted bacterial filaments (black arrow) and fine grained calcite (white arrow); scale bar = 500 µm. H) Rimstone sample showing no layering and some bacterial filament casts (white arrow); scale bar = 100 µm

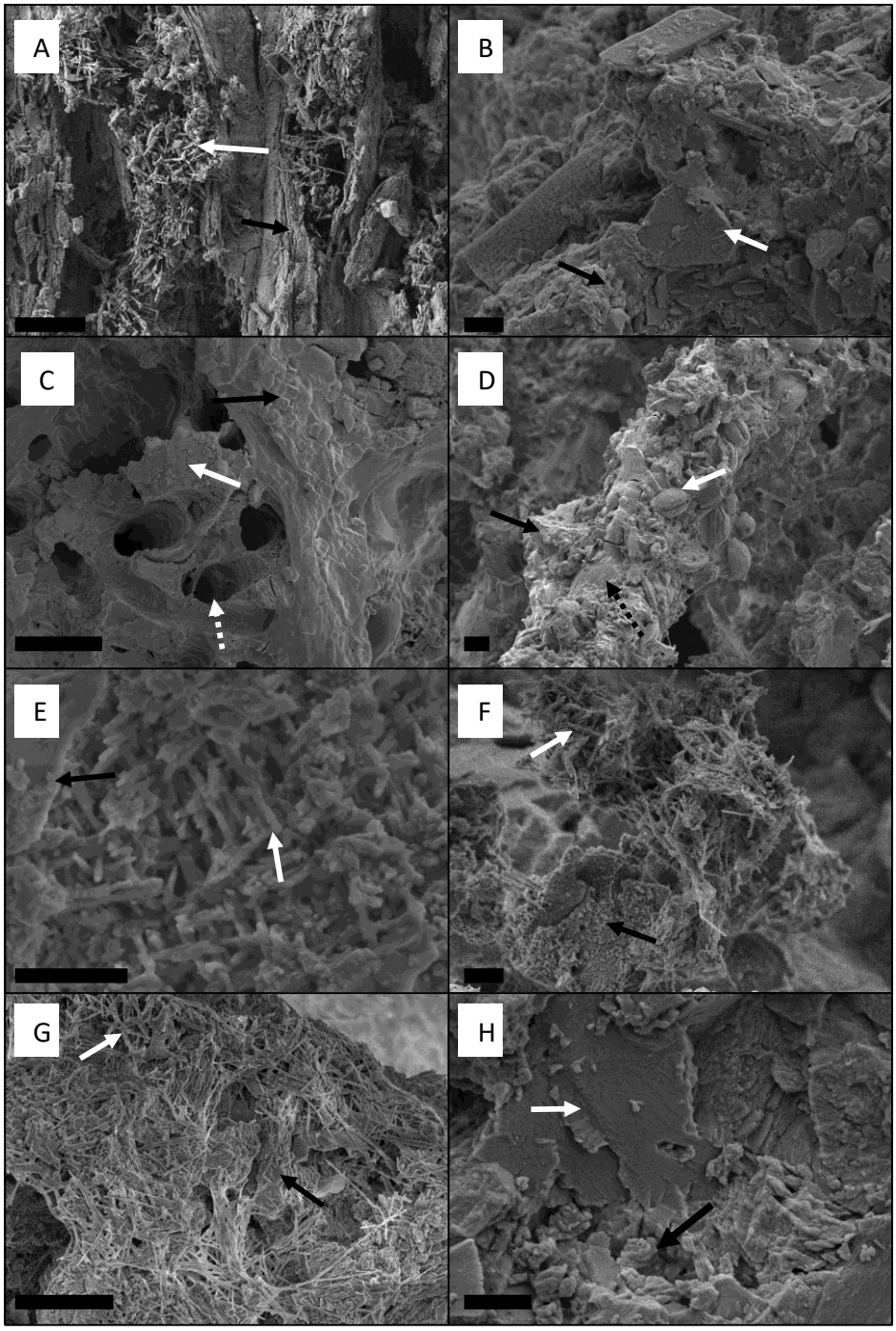

Fig. 1. 10 SEM micrographs of the micro textures observed in each sample. A) Nanocrystalline calcite coating bacterial filament casts (black arrow) and needle fibre calcite (white arrow) occurring between and within the filament casts of wrinkled laminar deposit; scale bar = 10 µm B) Rhizolith sample showing nano-crystalline calcite (black arrow) and larger plate-like minerals (white arrow); scale bar = 1 µm C) Micrite (White arrow) and cubic micro-crystals (Black arrow) from a beachrock tufa sample. Bacterial filament casts (white dashed arrow) are also observed here; scale bar = 10 µm D) Bacterial filaments (black dashed arrow), observed in a colloform growth type, encrusted with nano-crystalline calcite (black arrow) and diatoms (white arrow); scale bar = 10 µm. E) Laminar flat discharge apron sample showing NFC (white arrow) and minor micrite grains (black arrow); scale bar = 1 µm. F) A needle fibre calcite bundle (white arrow) above a micrite encrusted bacterial filament in a laminar flat sample from a barrage pool wall; scale bar = 1 µm. G) Columnar growth showing a NFC mesh (white arrow) and minor micrite (black arrow); scale bar = 5 µm H) Rimstone sample showing micrite grains (black arrow) and meso-crystalline calcite (white arrow); scale bar = 1 µm.

The crystal morphology, and other features, of the various tufa samples were examined at the micro- to nano-scale(Fig. 1.11 – 1.14). Overall three categories make up the tufa micro-fabrics, viz. meso-crystalline, micritic, and sparitic. Morphologies of halite and gypsum crystals are also observed in a portion of the tufa samples. The SEM images obtained in this study only comprehensively show the calcite needles' three-dimensional morphologies for some crystals.

The crystal morphology of wrinkled laminar waterfall deposits shows the differences in response to the filamentous bacteria presence. In areas that include filamentous bacterial casts, needle-fibre calcite occurs in clusters between nano-crystalline calcite coatings of the cast walls (Fig. 1.11A). The nano-crystalline calcite appears grainy while the needle-fibre calcite displays a variety of morphologies. Smooth types, in the form of single straight rods (black arrow in Fig. 1.11A), are observed but serrated-edged types are most common (black and white dashed arrows in Fig. 1.11A. In areas lacking filament casts the carbonate is dominated by meso-crystalline calcite (black arrow in Fig. 1.11B) and micrite grains (white arrow in Fig. 1.11B). Rhizoliths (waterfall deposits) are made up almost entirely of meso-crystalline calcite and micrite, although rare plate-like minerals and rods are also observed (Fig. 1.11C). Beachrock tufa also lacks NFC and is made up of a nano-scale globular texture, with some areas of larger (~ 1 μm^3) halite crystals (Fig. 1.11D and 1.11E). The nano-scale globules align and form short elongated/straight build-ups, similar to the smooth rod morphology (black arrow in Fig. 1.11E).

The colloform growth sample had less carbonate build-up compared to the other samples (Fig. 1.9). The crystal morphologies were consequently poorly developed, but other features were observed (Fig. 1.12). The poorly calcified bacterial filaments are covered in diatoms, varying in size (2-30 µm) and shape (pennate to circular), all held together by nanocrystalline calcite cement (Fig. 1.12A). In some areas the calcite has entirely covered the bacterial filaments and diatoms but their shape remains evident (Fig. 1.12B). In other areas, the calcified bacterial filaments and diatoms are scarce or absent (Fig. 1.12C). The concentration of calcite growth shows meso-crystalline texture development, encrusting of diatoms, and nano-crystalline calcite mounds (Fig. 1.12D). The mounds are made up of nano-scale calcite rhombs (Fig. 1.12E) and the diatoms are covered in nano-scale clusters of calcite (Fig. 1.12F).

Discharge aprons have similar crystal morphologies to wrinkled laminar waterfall deposits (Fig. 1.13). In laminar flat discharge aprons, serrated-edged NFC dominates the layers with bacterial filaments, although here the needles appear to have a preferred cross-hatch orientation and display epitaxial growth (Fig. 1.13A). Meso-crystalline calcite and micrite grains (< 200 nm in length) make up the layers lacking bacterial filaments (Fig. 1.13B). Halite is also present in the laminar flat sample but is uncommon (Fig. 1.13A). The NFC layers in columnar growth form a mesh-like needle texture with some small areas of nano-scale granular calcite (Fig. 1.13C). In some cases the needles align and form a 'bridge' between the gaps in crystal growth (Fig. 1.13D). Laminar flat growth at barrage pool walls also contains NFC in areas including bacterial filament casts, however, the needles form clusters rather than a mesh (Fig. 1.14A). The meso-crystalline calcite and the nano-scale calcite grains are more abundant here than in other samples displaying NFC development. The needles are once again dominated by serrated-edged types (Fig. 1.14B) and the fine grained calcite appears more developed (Fig. 1.14C). Minor square plate-like minerals are also observed in some areas (Fig. 1.14D). Barrage pool rimstone is made up of micritic and meso-crystalline textures (Fig. 1.14E), although infrequent nano-scale globular crystals and bladed calcite crystals are also observed (Fig. 1.14F).

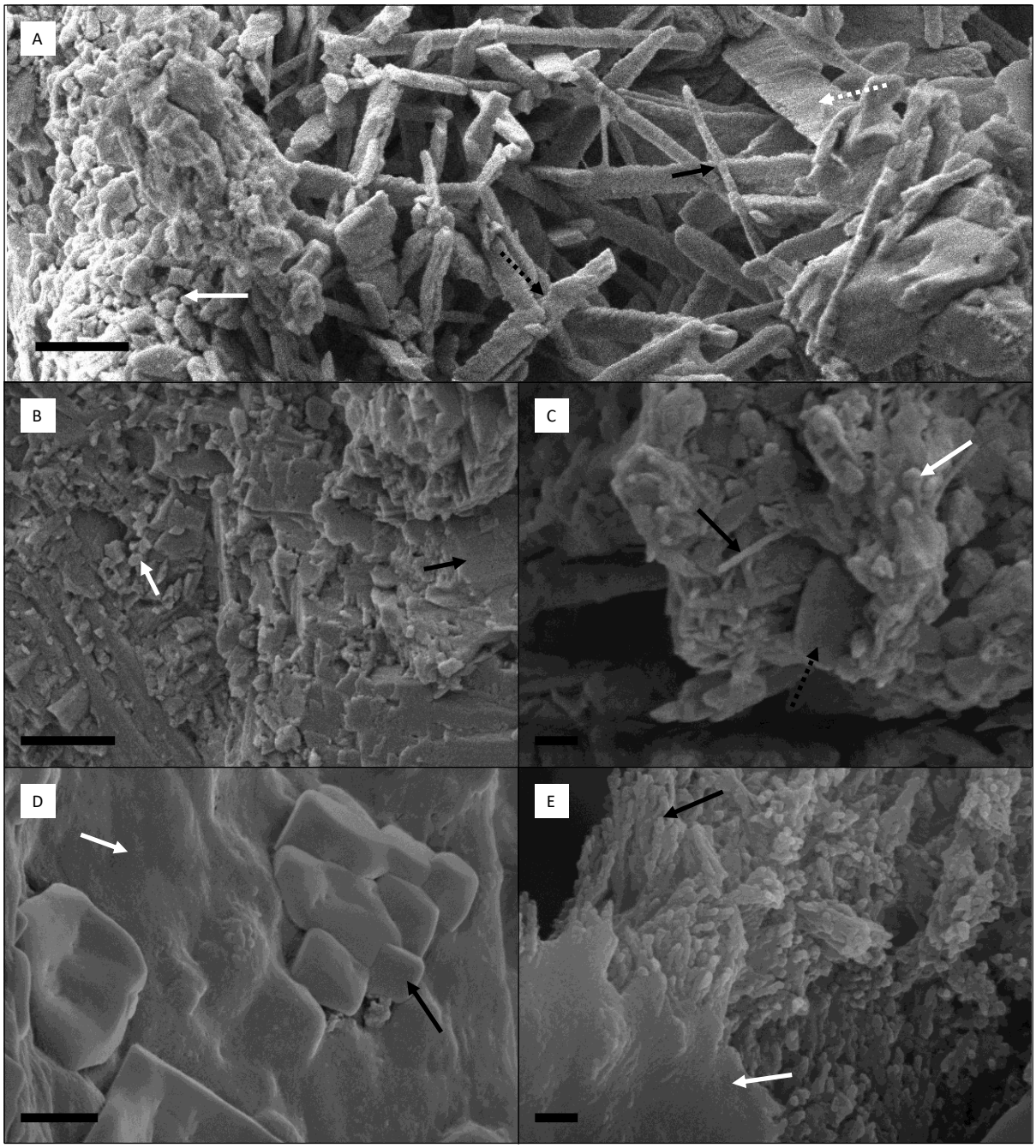

Fig. 1.11 Micrographs showing a range of crystal forms within waterfall and beachrock tufa samples. A) Nano crystalline calcite (white arrow) between a cyanobacterial filament cast and NFC showing smooth rods (black arrow), flat serrated-edged needles (white dashed arrow), and serrated-edged needles (black dashed arrow); scale bar = 1 µm. B) Waterfall deposit showing granular nano-crystalline calcite (white arrow) and meso-crystalline calcite (black arrow) in areas clear of bacterial filaments; scale bar = 1 µm. C) Rhizolith sample showing variation in crystal morphology, from single rods (black arrow), to flat plate-like minerals (black dashed arrow) and granular calcite (white arrow); scale bar = 200 nm. D) SEM micrograph of cubed crystals (black arrow) occurring above a nano-crystalline texture (white arrow); scale bar = 1 µm. E) Nano-scale globular calcite (black arrow) covered in some areas by a nano-crystalline coating, within a beachrock tufa sample; scale bar = 200 nm.

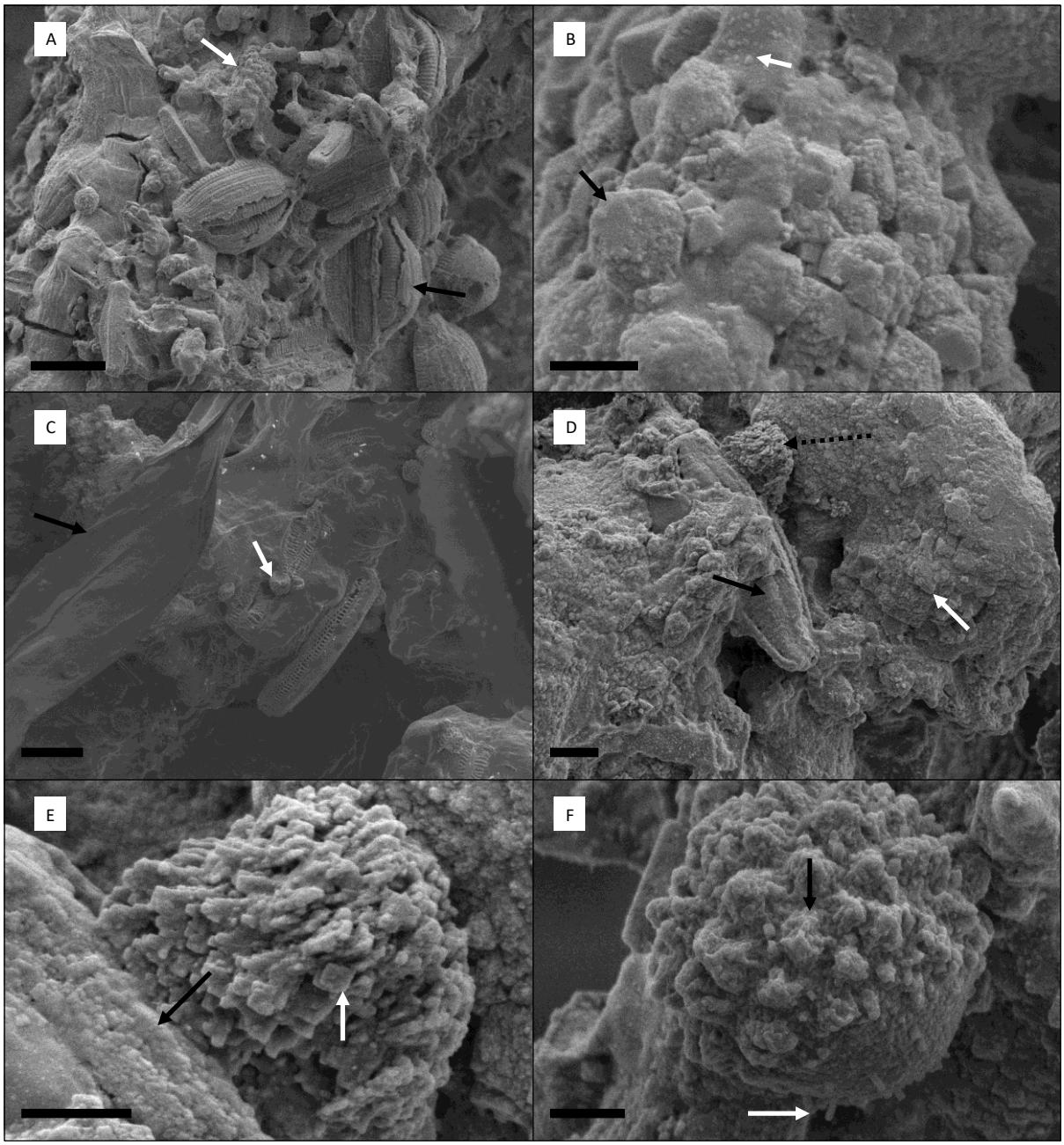

Fig. 1.12 Tufa sample micrographs showing various micro-structures and bacterial bodies within a colloform tufa sample. A) Diatom frustules (black arrow) and fine grained calcite (white arrow) encrusting bacterial filaments; scale bar = 10 µm. B) Nano-grained calcite (white arrow) occurring on (~1 µm) blocky calcite mounds (black arrow); scale bar = 1 µm. C) Small (~ 2 µm) diatom frustules (white arrow) near filamentous micro-algae (black arrow); scale bar = 10 µm. D) Pennate diatom (black arrow) cemented by meso-crystalline calcite (white arrow) and mounds of nano-scale calcite (black dashed arrow); scale bar = 1 µm. E) Close up view of calcite mound in D showing nano-scale calcite rhombs (white arrow) occurring on the surface of a pennate diatom (black arrow); scale bar = 1 µm. F) Close up of small diatom frustule encrusted by clusters of nano-scale calcite (black arrow) and short fine rods (white arrow); scale bar = 1 µm.

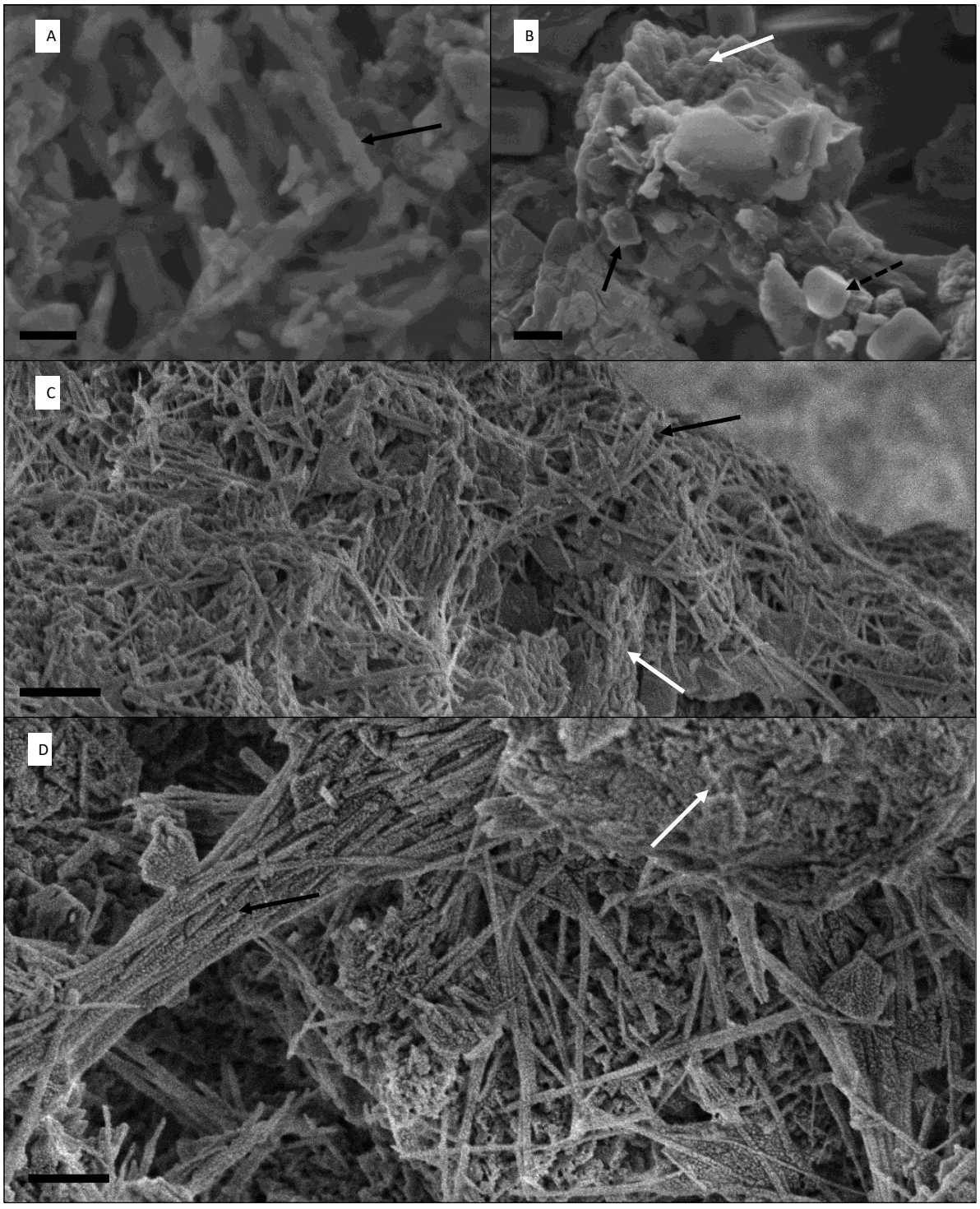

Fig. 1.13 SEM images showing the different micro-fabrics found in the tufa. A) Serrated calcite rods, showing epitaxial growth (black arrow), with a cross-hatch orientation; scale bar = 200 nm. B) Meso-crystalline calcite (white arrow) and nano-scale calcite grains (black arrow). Halite crystals are rare but also present (black dashed arrow); scale bar = 200 nm. C) Needle-fibre calcite mesh (black arrow), with no preferred crystal orientation, and underlying micrite (white arrow); scale bar = 2 µm. D) Needle-fibre calcite aligning to form a "bridge" (black arrow) above nano-crystalline calcite (white arrow); scale bar = 1 µm.

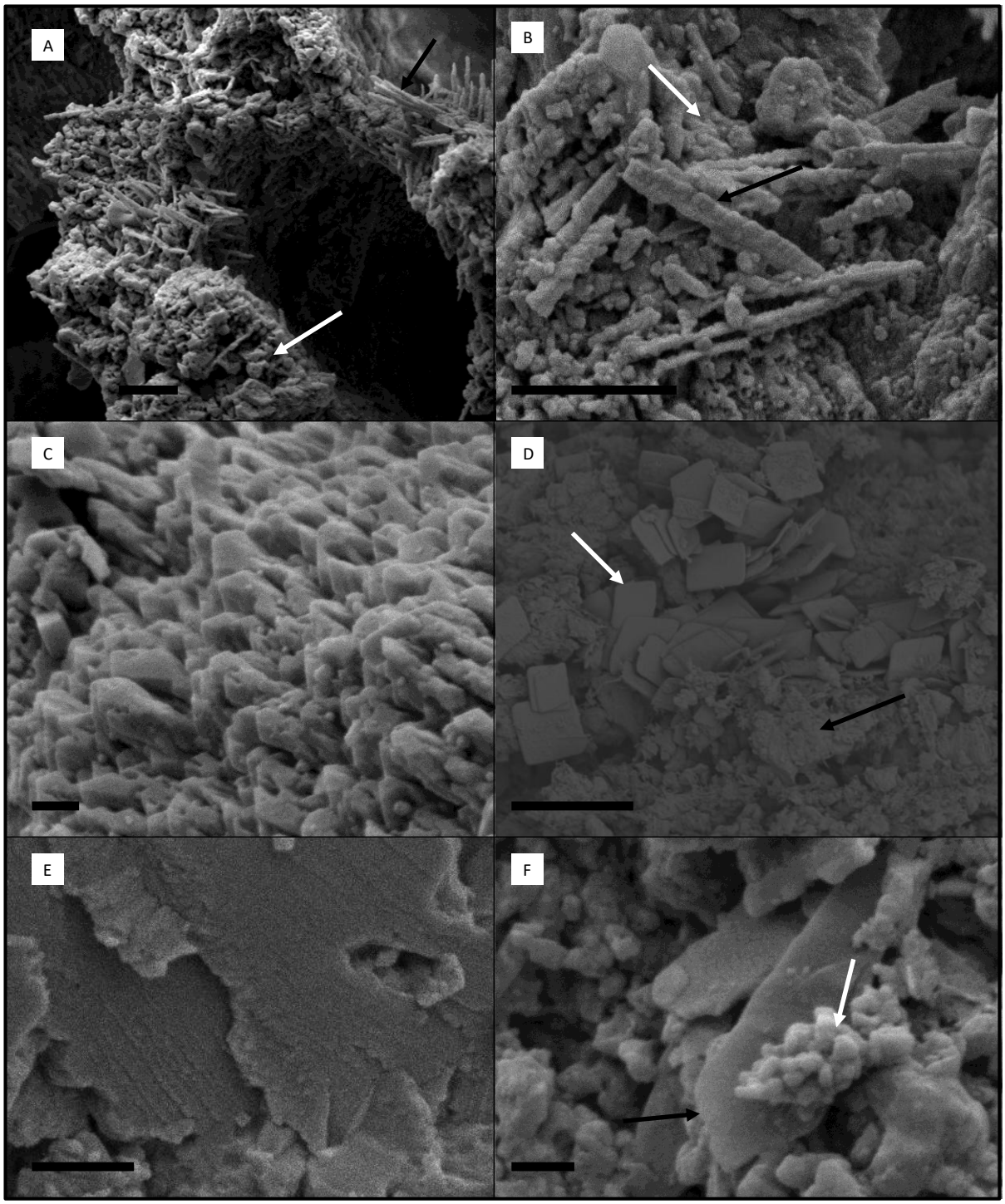

Fig. 1.14 SEM micrographs showing examples of the various crystal morphologies of barrage pools. A) NFC clusters (black arrow) and nano-scale calcite grains (white arrow) occurring near a bacterial filament cast; scale bar = 1 µm. B) Close up image showing the scale of the granular calcite (white arrow) and the serrated-edged type of NFC (black arrow); scale bar = 1 µm. C) SEM image showing the well-developed nano-scale calcite grains; scale bar = 200 nm. D) Rare plate-like gypsum crystals (white arrow) occurring in areas of fine grained calcite (black arrow); scale bar = 1 µm. E) Rimstone tufa sample showing meso-crystalline calcite and nano-scale calcite grains; scale bar = 500 nm. F) Uncommon nano-scale globular calcite (white arrow) and bladed calcite crystals (black arrow); scale bar = 200 nm.

4. Discussion

4.1 Thin section analysis

Thin sections were analysed for the purpose of classification and contextualization using the classification scheme proposed by Pedley (1990) and later revised by Jones and Renault (2010). The tufa meso-types in this study were shown to contain multiple textures/micro-fabrics, each characteristic of a different tufa facies. The different tufa fabrics occurring in each sample are labelled herein as micro-facies. The micro-fabric of each meso-type is discussed in terms of their depositional models: perched spring line and barrage pool (Pedley, 1990), both of which occur in the study area. The perched spring line model includes a fan shaped, sheet like deposit occurring on a slope below a fresh water spring. The barrage pool model consists of barrier-like phytoherm growth structures which act to accumulate flowing fresh water.

The perched spring line model occurring at Site B1 contains two main components: waterfall deposits and beachrock/conglomerate (Edwards et al., 2017). In thin section these two components encompass four distinct micro-fabrics, each representative of a different tufa facies. The waterfall deposits exhibit micro-fabrics associated with phytoherm boundstone facies (Fig. 1.2B & 1.C), phytoherm framestone facies (Fig. 1.2A & 1.3), and intraclast tufa facies (Fig. 1.2D). Smith et al. (2005) defined sparry crust (typical of boundstone facies) as pioneer laminae, which seem to be the case for these waterfall deposits. The sparry crust layers are nearest the bottom and encrust the original waterfall surface. Framestone facies and intraclast facies only appear above the sparry crust (Fig. 1.2A & 1.2C) and most likely form due to deposition and calcification of plant material and sedimentary grains respectively.

Beachrock/conglomerate also has multiple facies, containing lithoclast and boundstone facies. The bulk of the rock is made up of coated grain tufa (lithoclast facies) with a thin (~1 cm) layer of boundstone (layered) occurring at the uppermost section of the rock (Fig. 1.6A & 1.6B). Here the sparry crust occurs above the fine grained crust, which coats the rock and shell fragments, suggesting that the sparry crust in this instance does not play the role of pioneer laminae. Calcification of the rock and shell fragments may provide a suitable surface on which the filamentous bacteria can grow, leading to the formation of the

boundstone facies layering. Some beachrock samples also contained ovoid fenestra (Fig. 1.5) within the lithoclastic lower section. These features are likely the result of tunnelling or burrowing invertebrates (Rishworth et al. 2016b). The ovoid fenstra are only observed in areas dominated by sediment/shell fragments and are coated by micritic carbonate. This observation suggests that the invertebrates are moving through the lose sediment/shell fragments, including soft friable tufa material, before and during the calcification process. A number of benthic macro-invertebrates have been documented to be active within the microbialite systems near Port Elizabeth (Rishworth et al., 2016b). The ovoid fenestra are likely to be tunnels or burrows formed by the activity of similar metazoans.

The barrage pool model also contains two main components; back pools and front pools (Edwards et al., 2017). The back pools exhibit pustular formations, colloform growth and to a lesser extent laminar flat lateral growth. In thin section all three meso-types display alternating layers of type 1 and type 2 laminae, suggesting a phytoherm boundstone facies. Colloform growth has been suggested to form by the coalescence of pustular formations (Edwards et al., 2017). A closer examination of Fig. 1.8A provides evidence for this. Near the bottom of the image, small irregular shaped nodules (pustular formations) occur and show a clear separation between each growth structure (shown by the dashed black lines in Fig. 1.8A). Above these separated nodules, the layers become continuous (between growth structures) creating a more colloform growth appearance, thus confirming the suggested link between pustular and colloform growth. The sparry crust within the colloform growth appears to be calcified algal tufts (Fig. 1.8A) as opposed to calcified horizontal algal mats observed in laminar flat lateral growth. This suggests that the algae play a significant role in the formation of the various meso-structure morphologies.

The front pools exhibit rimstone growth that includes four distinct micro-fabric structures: layered (phytoherm boundstone), macrophyte encrustation (phytoherm framestone), tufa coated sedimentary grains (lithoclast tufa), and tufa coated ovoid fenestra. The bulk of the active rimstone is often encrusted in macroalgae (Edwards et al., 2017; Rishworth et al. 2018), indicative of phytoherm framestone facies. When freshwater is diverted away from the rimstone it becomes inactive and the macroalgae is removed via natural decay. The calcification and subsequent removal of these macroalgae are likely to be the cause of the

reef like framework formation, common in rimstone, and is also evidence of early diagenesis (Janssen et al., 1999). The layered structure observed in the rimstone (Fig. 1.8C) may have formed due to a hiatus period of macroalgae growth at the pool rim, since it contains no evidence of encrusted macro vegetation. These periods of low macroalgae cover may occur seasonally or as a result of the metazoans known to consume macroalgae at these sites, particularly during winter (Rishworth et al., 2017, 2018). These or similar burrowing metazoans are likely responsible for the formation of the ovoid fenestra seen in beachrock and rimstone tufa. The ovoid fenestra or burrows are also coated with fine grained tufa, suggesting that calcification of the sediments occurred after or during the tunnels formation. The metazoans most likely burrowed through the loose sediment which was then calcified at a later stage. The lithoclast facies observed in the two rimstone samples (Fig. 1.8C & 1.8D) occur due to the calcification of washed-in beach sediments.

A combination of the two depositional models (barrage pool model and perched springline model) is found at Site D. This is also the only site at which columnar growth, found at the bottom of an inactive discharge apron, was sampled. Discharge aprons commonly exhibit pustular formations, colloform growth and laminar flat growth. Alternating layers of type 1 and type 2 are observed in each meso-type of the discharge apron, suggesting a phytoherm boundstone facies. The columnar growth sample was found at the bottom of a discharge apron and shows obvious and continuous layer boundaries. The colloform growth occurring on the discharge apron (Fig. 1.7A) is made up of both types of layers; however, the boundaries are not as clear as the back pool colloform growth (Fig. 1.7A & 1.8A). Laminar flat growth occurring on the discharge aprons is also made up of alternating layers (Fig. 1.7B) of both types but appears more distinct than the laminar flat lateral growth of the back pools (Fig. 1.8B). The type 2 (fine grained) layers of the discharge apron are significantly thinner than the type 2 layers of the laminar flat back pool growth and lack the characteristic trapped sediment. This indicates that laminar flat discharge aprons are not exposed to as much detrital sediment or that the sediment is quickly washed away.

The thin section analysis revealed a variety of micro-fabrics and micro-structures (Table 2) in the various tufa facies at each site. Previously the tufa deposits near Port Elizabeth have been referred to as tufa “stromatolites” (e.g. Perissinotto et al., 2014; Edwards et al., 2017) given the formation of bacterially mediated, macroscopically layered carbonates. The

definition of stromatolites has been argued in terms of the layering and presence of biogenic and abiogenic carbonate (e.g. Riding, 1999), although there is now a consensus that in order for a deposit to be termed a stromatolite it must be macroscopically layered (e.g. Jones and Renault, 2010). The presence of non-layered meso-types in the tufa deposits near Port Elizabeth, indicate that the deposits are not entirely stromatolitic. Thus collectively the deposits should be referred to as tufa microbialites, as they contain stromatolitic and other micro-facies.

4.2 Mineralogy and crystal morphology

Results of the XRD analysis show a dominance of low-Mg calcite. This can be expected in most temperate water tufa deposits (Jones and Renault, 2010) and is extremely likely to be mediated through bacterial activity (Dodd et al., 2018). The minor inclusions of halite, and to a lesser extent gypsum, may have formed when the samples were dried for analysis., however, the close proximity to marine water suggests it is likely a result of sea water evaporation after intrusion by overtopping or wave splash. Despite the lack of quartz in the XRD results, the thin section analysis does show minor quartz inclusions in waterfall deposits, beachrock, discharge aprons, and barrage pools (Table 1.2). The quartz and other minor minerals (Table 1.1) identified in the active rimstone are likely to be washed-in beach sediments trapped within the rimstone tufa. Mineral grains seen in thin section of some waterfall deposits are likely trapped soil and/or dune material washed in by rainfall events or fresh water seeps. Vaterite, which is identified in the inactive rimstone tufa, has been associated with bacterially mediated mineralization (Rodriguez-Navarro et al., 2007; Azulay et al., 2018). However, its occurrence in only the inactive rimstone suggests it may have precipitated abiogenically or under conditions of different (non-accretionary) bacterial metabolic activity.

In spite of the mineral similarity of all samples, the morphology of the calcite can differ greatly. The images obtained via SEM show calcite morphological variation within and between tufa meso-types (Table 3). The main crystal morphological variation in the tufa deposits appears to be associated with the type of layer. Type 1 layering, associated with vertical cyanobacteria filaments, commonly displays a sparitic needle-fibre calcite (NFC)

morphology, while type 2 layering, with a fine-grained texture, displays a micritic and meso-crystalline morphology. This could suggest that the cyanobacteria filaments play a role in NFC precipitation. In the active colloform sample the bacterial filaments were intact and no NFC was observed (Fig. 1.12). This observation, combined with NFC growth extended into a bacterial cast (Fig. 1.14A), suggests that NFC micro-fabric formation occurs after or during filament decay. Acicular crystal morphology has been associated with post-mortem degradation of cyanobacteria (Kazmierczak et al., 2015). Cailleau et al. (2009) showed that NFC is initially released as straight rods (Fig. 1.11A), formed within organic filaments that control the rod morphology. The complex morphology that follows is a result of aggregation and welding occurring after subsequent decay of the organic matter. The rods are believed to evolve into whisker crystals, via coalescence of euhedral crystals on a rod, or rhomb chains, through successive epitaxial growth steps on a needle during variations in growth conditions (Cailleau et al., 2009). The evolution of rods, whisker crystals and rhomb chains can result in a number of complex morphologies, each represented by a type number from 1 to 33 (Fig. 1.15). The dominant needle morphology observed in this study appears to be type 13, although minor smooth types (type 3) and other serrated-edged types (possibly type 11 or 20) are also observed (Fig. 1.11A). Type 13 is a serrated-edged rhomb chain type constructed by superimposed sub-planes (Fig. 1.14B). Sub-planes are refer to the crystal facets of each calcite rhomb that are now aligned due to the accumulation of more grains along the y-axis of the chain. The presence of this type of rod suggests epitaxial and syntaxial crystal growth that in turn indicates diagenesis (e.g. Canveras et al., 2006; Cailleau et al., 2009). Stromatolites have not yet been documented to contain NFC, however, other bacterial carbonates and filamentous bacterial mats have been associated with its development (e.g. Gruszczynski et al., 2004; Bindschedler et al., 2014). The occurrence of needle-fibre calcite can be used as evidence for the biogenic origin of the tufa deposits near Port Elizabeth.

The meso-crystalline and micritic textures are similar throughout all the samples, occurring predominantly in areas lacking bacterial filaments and filament casts, but are also observed in some areas beneath the NFC micro-fabrics (Fig. 1.13). The NFC is observed to form a randomly orientated mesh (Fig. 1.13C), but can also form clusters (Fig. 1.10F), bridges (Fig. 1.13D) and cross-hatched mesh (Fig. 1.13A). All four types include epitaxial forms of

NFC (serrated-edge types), suggesting that straight rods have been released from their constraints and secondary crystal growth has occurred (e.g. Bindschedler, et al., 2014; Cailleau et al., 2009). In order to interpret the formation of these various NFC textures one would need to analyse the origin of the straight rods. This study suggests that the straight rods are a product of filamentous bacterial decay but the exact processes are unknown.

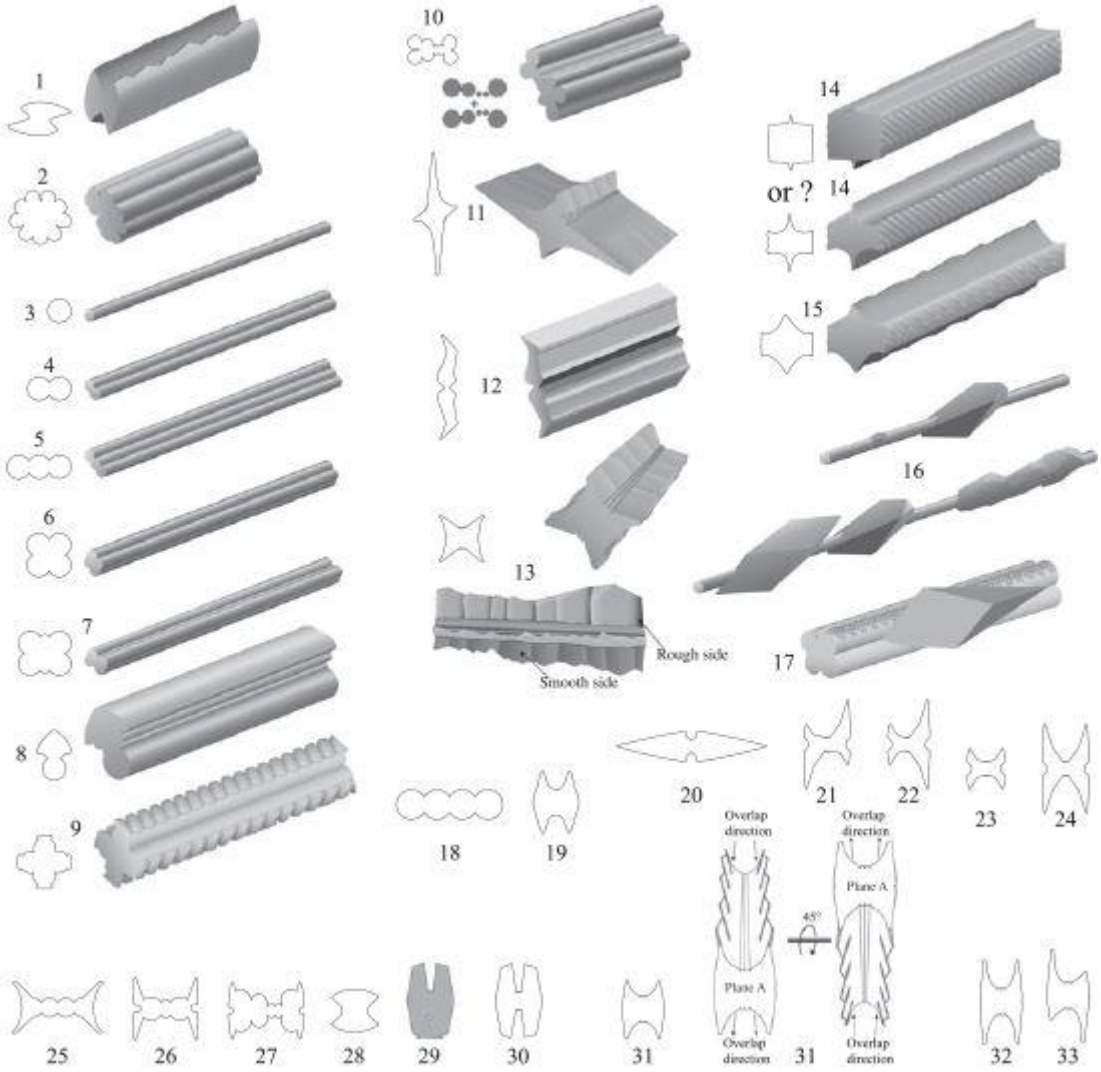

Fig. 1.15 A diagram showing a non-exhaustive synthesis of needle morphology. Each type is assigned a number and is represented by cross-section or three-dimensional shape. The various morphologies are separated into three groups (i) Serrated-edge types: Types 1, 11 – 13, and 19 – 33. (ii) Smooth types: Types 2 – 8, 10, and 18. (iii) Complex types: Types 9, and 14 – 17. (Taken from Cailleau et al. (2009))

4.3 Comparison to similar deposits

Edwards et al. (2017) showed that the macro-structures, meso-structures and depositional environments, of these deposits are similar to the supratidal deposits found in south-west Australia (Forbes et al., 2010), Giant's Causeway of Northern Ireland (Cooper et al., 2013), and Morgan's Bay in South Africa (Smith and Uken 2003). All these deposits may be of a similar coastal facies, however, a comprehensive micro-structure and mineralogical analysis is needed to confirm a genetic link (Edwards et al., 2017).

In this study, X-ray diffraction, thin section analysis, and SEM imaging reveal variations in the mineralogy of the Eastern Cape tufa deposits, comparable to those observed in the deposits of South Western Australia (e.g. Forbes et al., 2010). The XRD bulk rock analysis results show a clear dominance by low-Mg-calcite and minor inclusions of halite in all samples. In contrast the supratidal tufa deposits from South Western Australia are dominated by calcite and contain minor Mg-calcite and halite (Forbes et al., 2010). The formation of low Mg-calcite at the Eastern Cape coast instead of calcite could be a result of higher Mg/Ca ratios in the associated waters (e.g. Jones and Renault, 2010; Forbes et al., 2010; Dodd et al., 2018). The XRD analysis of the tufa deposits in Australia also show a minor quartz (< 3%) and aragonite (typically < 10 %) content, while the XRD results here do not. Minor quartz grains are, however, observed in the thin sections of waterfall deposits, beachrock, discharge aprons, and barrage pools (Table 2.2). There is no evidence to suggest any aragonite precipitation in the Eastern Cape tufa deposits. Therefore, the mineralogy of the South-West Australian deposits is slightly different to those of the Eastern Cape. This subtle dissimilarity may be a function of differing physicochemical, hydrochemical, thermodynamic, and/or nutritional conditions at the two sites (e.g. Jones and Renault, 2010; Dodd et al., 2018). The mineral composition of the Morgan's Bay and Giant's Causeway tufa deposits have not been investigated in depth, making a comparison to this study unfeasible for now.

Two types of layers have been documented in the microbial deposits found at Cape Morgan: thicker, lighter layers comprising tightly packed vertical filaments (type 1); and thinner, darker layers often containing sedimentary grains and diatoms (type 2) (Smith et al. 2005). There is also a gradation shown from stromatolitic tufa (layered) to un-layered tufa (Smith et al., 2018). The tufa deposits in this study show similar layering and micro-fabrics: lighter,

thicker layers made up of tightly packed vertical filaments and thinner, darker layers often containing sedimentary grains. The layering here is shown to be dependent on the samples' meso-type. The laminar flat discharge apron, colloform, and columnar types display clear alternating type 1 and type 2 layers (Fig. 1.7 & 1.8). Wrinkled laminar, laminar flat beachrock, and rimstone types only showed type 1 layering in sections of the sample (Fig. 1.2, 1.6, and 1.8), while rhizolith samples showed no type 1 layering. Type 2 is observed in all samples in this study and often shows trapped sedimentary grains and shell fragments, although no diatoms were observed. Similar textures are also observed in the supratidal tufa deposits from Contos Springs and Quarry Bay, South-West Australia (Forbes et al., 2010). These deposits, like the ones observed in this study, include laminated structures, sedimentary grains, marine bioclastic material, void space (fenestra), and calcified organic filaments. This similarity in the micro-fabrics of all three sites strongly suggests a similar genetic link in terms of their formation.

5. Conclusion

The micro-structure and mineralogical analyses conducted in this study allow us to draw the following conclusions on the tufa deposits near Port Elizabeth. Firstly, the deposits are dominantly calcareous (low-Mg calcite) and are better referred to as tufa microbialites and not tufa stromatolites, given the array of microbialite facies other than the well-laminated fabric. Secondly, these microbialites are shown to have a similar mineralogy to the supratidal tufa deposits observed in Contos Springs and Quarry Bay, Australia (Forbes et al., 2010). Thin section micro-structure analysis shows similarity to the Australian supratidal deposits and the tufa deposits of Cape Morgan, South Africa (Smith et al., 2011). This suggests that similar physical and chemical processes may be underpinning the microbialite formation at these sites, which is further confirmed by mineralogical and micro-structure similarity.

This study also demonstrates, for the first time to our knowledge, the presence of epitaxial forms of NFC in a stromatolite/microbialite deposit. Importantly, this confirms the biogenic origin, digenesis and re-crystallization of the Eastern Cape microbialites, as previously suggested by Perissinotto et al. (2014)and Rishworth et al. (2016a).

Further insights into the exact processes involved in the needle-fibre calcite formation may be produced by examination via transmission electron microscopy (TEM). The use of TEM will allow examination of the tufa deposits at a positive pressure, meaning there will be no need to dry samples. With little to no sample preparation, the organic sleeves that control rod morphology may be preserved. Imaging a range of tufa specimens, in this way, may provide a visual representation of the effects of digenesis and re-crystallization.

Chapter 2

Geochemical characterisation of the peritidal tufa microbialites near Port Elizabeth, South Africa

1. Introduction

Active tufa microbialite systems, found along the Port Elizabeth coast of South Africa, have been analysed in terms of their biological drivers, morphology, ecosystem dynamics, and associated water chemistry (e.g. Edwards et al., 2017; Rishworth et al., 2016a, Dodd et al., 2018). The tufa deposits contain a number of facies, including phytoherm framestone (fine-grained), phytoherm boundstone (layered), and lithoclast facies. The layered types (phytoherm boundstone) are identified as shore platform stromatolites (SPS), given their layered texture and occurrence on a wave cut rocky platform (e.g. Smith et al., 2018). Stromatolites made up of minerals precipitated in-situ, such as SPS, have been shown to be similar to their ancient marine equivalents (Riding, 2008). Ancient stromatolites are often charcterized by their depositional environment, which can be inferred using their major and trace element cocentrations (e.g. Frimmel, 2009). Rare earth elements (REE) and yttrium shed light on water conditions based on elemental range and pattern (e.g Chagas et al., 2016). The major and trace elemental concentrations of active, modern microbialites may, therefore, be compared to existing active stromatolites and possibly used as an analogue for ancient marine deposits.

The chemical constituents of tufa deposits were examined using X-ray fluorescence (XRF), Laser Ablation Inductively Coupled Plasma Mass Spectrometry (LA-ICP-MS), and Scanning Electron Microscopy / Energy Dispersive X-Ray Spectroscopy (SEM/EDS). XRF and LA-ICP-MS were used to analyse bulk major and trace element levels respectively, while major elements in specific areas within the tufa were identified using SEM/EDS.. XRF is sufficient in determining the major elemental abundance, but does not have a low enough detection limit to measure the trace element abundance. Trace elements are better measured by LA-ICP-MS as this technique has a significantly lower detection limit. Problems do arise, due to contamination with washed-in sediment, as XRF and LA-ICP-MS analyse the bulk rock chemistry and not only the carbonate matrix. SEM/EDS is useful as is allows for analyses of the carbonate with little or no interference from the detrital component.

Information on the elemental makeup of tufa microbialites can and has been used in geomorphological and palaeontological reconstructions (Janssen et al., 1999; Frimmel, 2009; Garnett et al., 2004; Andrews and Brasier, 2005). Trace element geochemistry is

shown to be a good tool for determining depositional environments and the effects of detrital material on ancient carbonate rocks (Bolhar and Van Kranendonk, 2007; Frimmel, 2009). The chemical composition, of modern in-situ deposits may be used in a similar way and has not yet been examined in the tufa systems near Port Elizabeth. This study will provide the first geochemical study of these microbialites and is based on observations conducted within the previously studied sites B1, C2, and D (following Perissinotto et al., 2014 and Edwards et al., 2017). An elemental evaluation of these deposits may also provide key information on the physical and biological controls of tufa formation (Forbes et al., 2010). Identifying and describing the elemental composition of the Eastern Cape tufa microbialites is, therefore, the primary aim of this study.

2. Materials and methods

2.1 Study area

The study was conducted on the same area described by Edwards et al. (2017). Sites B1, C2, and D were selected and sampled between November 2017 and May 2018. These three sites include all the various macro- and meso-structures noted in the broader study area and are representatives of the three depositional models identified by Edwards et al. (2017). The perched springline model and the barrage pool model occur at site B1 and C2 respectively, while site D is a combination of the two (Fig. 2.1).

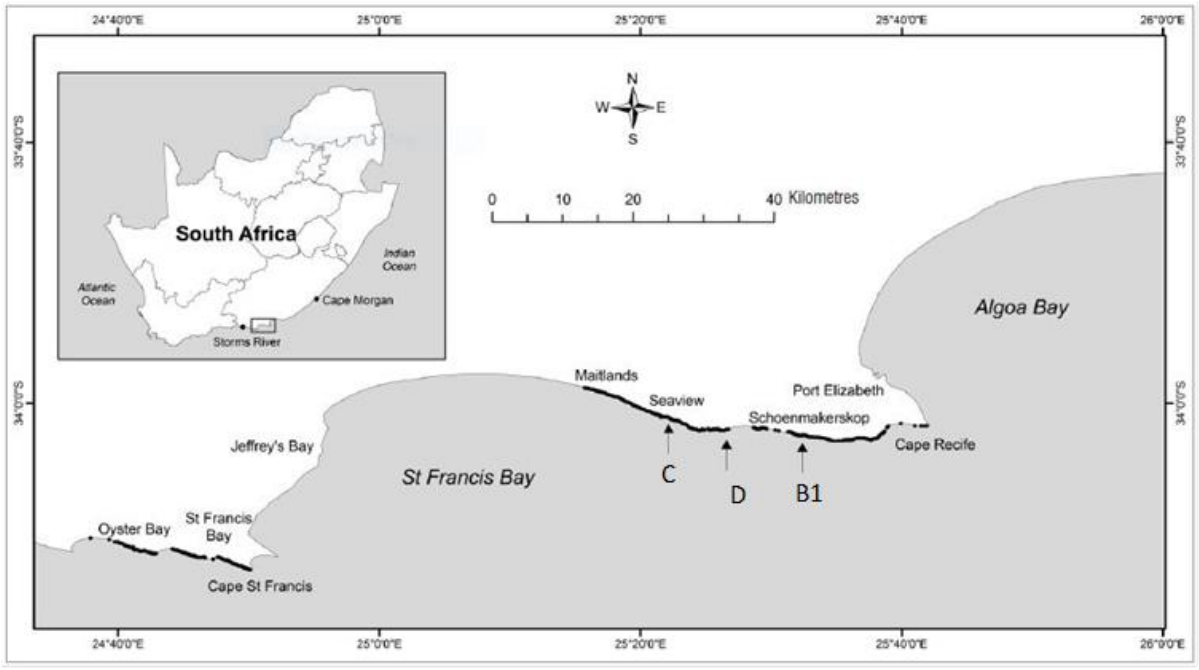

Fig. 2.1 Map indicating the three study sites along the Eastern Cape coast. Black points along the coast represent known tufa stromatolite colonies. (after Perissinotto et al., 2014)

2.2 Sample collection

In total, 15 tufa samples were collected for chemical analysis; 8 were used for bulk rock analysis (Table 2.1) and 7 for specific small area analysis (Table 2.2). At all three sites, samples with microbial activity (active) and dried out samples (inactive) were collected at varying elevation along the tufa profiles, to note any chemical variance. Edwards et al. (2017) noted morphological variations with elevation, suggesting the possibility of chemical variation with the same factor. Although specific elevations were not noted when sampling, the tufa systems were separated into three categories (as in Chapter 1) based on level of fresh- and marine-water mixing as a factor of elevation (fresh, mixed, and marine).

Table 2.1. A summary of the samples collected and used for bulk rock major and trace elemental analyses. At least one sample of each macro- and meso-type was used for bulk rock analysis.

Sample	Macro-structure	Meso-type	Active/inactive	Site	category
X1	Waterfall	Wrinkled laminar	Active	B1	Fresh
X2	Waterfall	Wrinkled laminar	Inactive	B1	Fresh
X3	Waterfall	Rhizolith	Inactive	B1	Fresh
X4	Barrage pool	Laminar flat	Active	D	Mixed
X5	Barrage pool	Laminar flat	Inactive	D	Mixed
X6	Discharge Apron	Colloform	Active	D	Mixed
X7	Barrage pool	Rimstone	Active	C2	Marine
X8	Barrage pool	Rimstone	Inactive	C2	Marine

Table 2.2. An overview of the tufa samples collected and used for elemental analysis via SEM/EDS. At least one sample of each macro- and meso-type was used for SEM/EDS analysis.

Sample No.	Macro-structure	Meso-type	Active/inactive	Site	category
S1	Waterfall	Wrinkled laminar	Inactive	B1	Fresh
S2	Beachrock	Laminar flat	Active	B1	Fresh
S3	Barrage pool	Laminar flat	Active	D	Mixed
S4	Discharge Apron	Colloform	Active	D	Mixed
S5	Discharge Apron	Laminar flat	Inactive	D	Mixed
S6	Barrage pool	Rimstone	Active	C2	Marine
S7	Barrage pool	Rimstone	Inactive	C2	Marine

2.3 Sample preparation and analysis

For bulk rock analyses the samples were dried at 50 °C overnight before being crushed into a fine powder using a rock mill. Approximately ten grams of each sample were sent to the Central Analytical Facilities (CAF) in Stellenbosch for further sample preparation and analysis. A PAN analytical XRF, Rh Tube, 3kWatt spectrometer was used to analyse the major elements as an oxide weight percentage composition (wt%). The trace elements on the fused disc were determined using a Resonetics 193nm Excimer laser ablation instrument. Trace element composition was measured as elemental weight percent. The samples, produced by cutting small (~1cm^3) blocks from hand samples were first semi polished with water paper and then sent to CHRTEM (Centre for High Resolution Transmission Electron Microscopy) for mounting, polishing and carbon coating. Overall, seven samples were prepared and analysed by a JSM-7001F field emission scanning electron microscope.

3. Results

3.1 Bulk rock major and trace elements

Bulk rock analysis of the major elements shows that the tufa deposits are dominated by CaO (44-54%).(Table 2.3). Loss on Ignition (LOI), which represents the organic matter, CO_2 loss from carbonates, and possible hydrous mineral phases also constituted a large portion of the tufa (39-49%). A few samples also had higher levels of SiO_2. For the remaining elements, concentrations were higher in samples X7 and X8 (rimstone), and marginally higher in X3 (rhizolith). Trace element data are presented in Table 2.4. The marine samples as well as the rhizolith sample show a slight increase in most trace elemental measurements when compared to the other samples.

Table 2.3. Analysis of the major elements in each tufa type taken from the three study sites. Values are given as a percentage oxide (wt%).

Sample	Site	Type	Category	CaO	L.O.I.	SiO_2	MgO	Al_2O_3	Fe_2O_3	Na_2O	P_2O_5	TiO_2	K_2O	Cr_2O_3	MnO
X1	B1	Inactive Waterfall deposit	Fresh	54,19	43,88	0,86	1,30	0,03	0,02	0,06	0,03	0,02	0,01	bdl	bdl
X2	B1	Active Waterfall deposit	Fresh	52,52	44,34	2,02	0,42	0,08	0,05	0,01	0,04	0,02	0,01	bdl	bdl
X3	B1	Rhizolith	Fresh	51,71	43,47	3,14	0,46	0,38	0,16	0,04	0,05	0,06	0,03	bdl	bdl
X4	D	Inactive Wall growth	Mixed	52,15	46,74	0,46	0,85	0,10	0,05	0,08	0,06	0,02	0,01	bdl	bdl
X5	D	Active wall Growth	Mixed	49,34	49,00	0,41	1,20	0,04	0,03	0,06	0,02	0,01	0,01	bdl	bdl
X6	D	Active Colloform	Mixed	50,40	48,13	0,19	1,04	0,03	0,02	0,04	0,03	0,03	0,01	bdl	bdl
X7	C	Inactive Rimstone	Marine	49,47	43,15	4,05	2,67	0,53	0,34	0,14	0,11	0,05	0,03	bdl	0,01
X8	C	Active Rimstone	Marine	44,32	39,52	12,36	2,00	1,08	0,52	0,24	0,12	0,11	0,08	bdl	0,01

*bdl = below detection limit

Table 2.4. Trace element analysis of each tufa type found within the study area. Trace element compositions are given as PPM.

Sample	Sc	V	Cr	Co	Ni	Cu	Zn	Rb	Sr	Y	Zr	Nb	Mo	Cs	Ba	La	Ce
X1	0,099	1,615	4,290	0,227	1,320	4,405	10,790	0,145	463,5	0,248	2,595	0,089	0,102	bdl	15,045	0,194	0,354
X2	0,366	5,345	4,885	0,364	1,825	7,585	10,805	0,415	779,0	0,497	9,085	0,293	0,383	bdl	29,535	0,469	0,936
X3	0,649	5,355	8,065	0,442	3,590	14,350	14,945	1,574	679,0	1,149	8,605	0,571	0,211	bdl	41,400	1,127	2,512
X4	0,109	7,055	6,475	0,252	2,175	3,810	68,350	0,368	350,5	0,186	1,680	0,081	0,108	bdl	24,450	0,232	0,488
X5	0,064	1,980	4,800	0,132	0,805	5,580	15,270	0,216	458,0	0,073	1,635	0,058	0,168	bdl	32,600	0,094	0,193
X6	0,042	1,130	3,685	0,077	0,764	2,765	11,395	0,141	296,5	0,099	1,138	0,040	0,110	bdl	22,695	0,100	0,234
X7	0,775	6,370	10,225	0,709	5,120	21,700	12,300	1,653	1568,5	1,908	12,645	0,542	0,225	bdl	37,700	1,952	4,005
X8	1,976	11,105	14,195	1,326	5,015	29,340	13,210	1,816	1484,0	4,460	96,250	1,522	0,269	bdl	56,850	4,250	8,745

Sample	Pr	Nd	Sm	Eu	Gd	Tb	Dy	Ho	Er	Tm	Yb	Lu	Hf	Ta	Pb	Th	U
X1	0,075	0,192	0,044	0,033	0,054	0,017	0,050	0,016	0,030	0,009	0,035	0,013	0,080	0,029	6,415	0,069	0,287
X2	0,289	0,514	0,281	0,196	0,281	0,138	0,196	0,182	0,162	0,136	0,166	0,124	0,389	0,141	5,980	0,250	0,803
X3	0,304	1,008	0,211	0,116	0,196	0,063	0,207	0,059	0,144	0,030	0,121	0,048	0,322	0,076	6,995	0,329	0,955
X4	0,062	0,211	0,057	0,029	0,052	0,014	0,043	0,016	0,036	0,020	0,022	0,010	0,070	0,020	0,747	0,080	0,313
X5	0,058	0,108	0,039	0,020	0,039	0,016	0,031	0,017	0,022	0,016	0,019	0,018	0,068	0,015	1,459	0,049	0,169
X6	0,029	0,088	0,025	0,011	0,021	0,009	0,026	0,017	0,015	0,007	0,017	0,013	0,057	0,020	0,942	0,034	0,124
X7	0,485	1,753	0,360	0,097	0,318	0,057	0,308	0,064	0,188	0,038	0,166	0,031	0,336	0,065	4,660	0,572	0,294
X8	1,011	4,100	0,839	0,173	0,737	0,114	0,722	0,149	0,457	0,064	0,437	0,069	2,330	0,106	9,740	1,337	0,615

* bdl = below detection limit

3.2 SEM/EDS

Scanning electron microscopy/energy dispersive x-ray spectroscopy allowed for the analysis of individual tufa crust types present in the samples, as well as any other inclusions. The findings are separated into carbonate matrix (Table 2.5) and inclusions (Table 2.6). The carbonate matrix of the tufa, as well as any other inclusions, are separated in terms of the level of marine- and freshwater mixing as well as the crust type. Type 1 and type 2 crusts were identified respectively by the abundance of filamentous bacterial casts or the lack thereof. (Fig. 2.2). Due to the samples being carbon coated, the C in the carbonate could not be determined and do not form part of the results. Various minerals were identified using measured wt% and calculated molar concentrations of elemental constituents.

As with the XRF results both types of crust are dominated by O, Ca. All samples have minor amounts of Mg and most contain traces of Na and S. Mixed and beachrock samples also contain Cl. Sr was only detected in the barrage pool samples and Si was found in one rimstone sample. There are no clear trends between the chemistry and crust types, but Mg does show an increasing trend towards more marine water (Table 2.5).

A number of features such as sub-rounded grains, cubic minerals, and diatom frustules were also observed and analysed (Fig. 2.2). The sub-rounded grain inclusions were found in the two rimstone samples (marine) and the colloform discharge apron sample (mixed). A number of sub-rounded grains were identified as quartz (2:1 ratio for Si to O). White cubic minerals (Fig 2.3C), identified as halite (1:1 ratio for Na to Cl), are observed in the beachrock tufa sample (SEMC2). The grain in SEMC4 (Fig 2.3A) has a similar O wt% to the quartz grains but a significantly lower Si wt%, and also contains a significant amount of Al and minor amounts of Fe and Ti (Table 2.6). The molar ratios of the elements observed in the grain did not match any expected detrital mineral. It is therefore suggested that this is either one mineral with alteration products or the SEM technique has sampled two adjacent minerals.

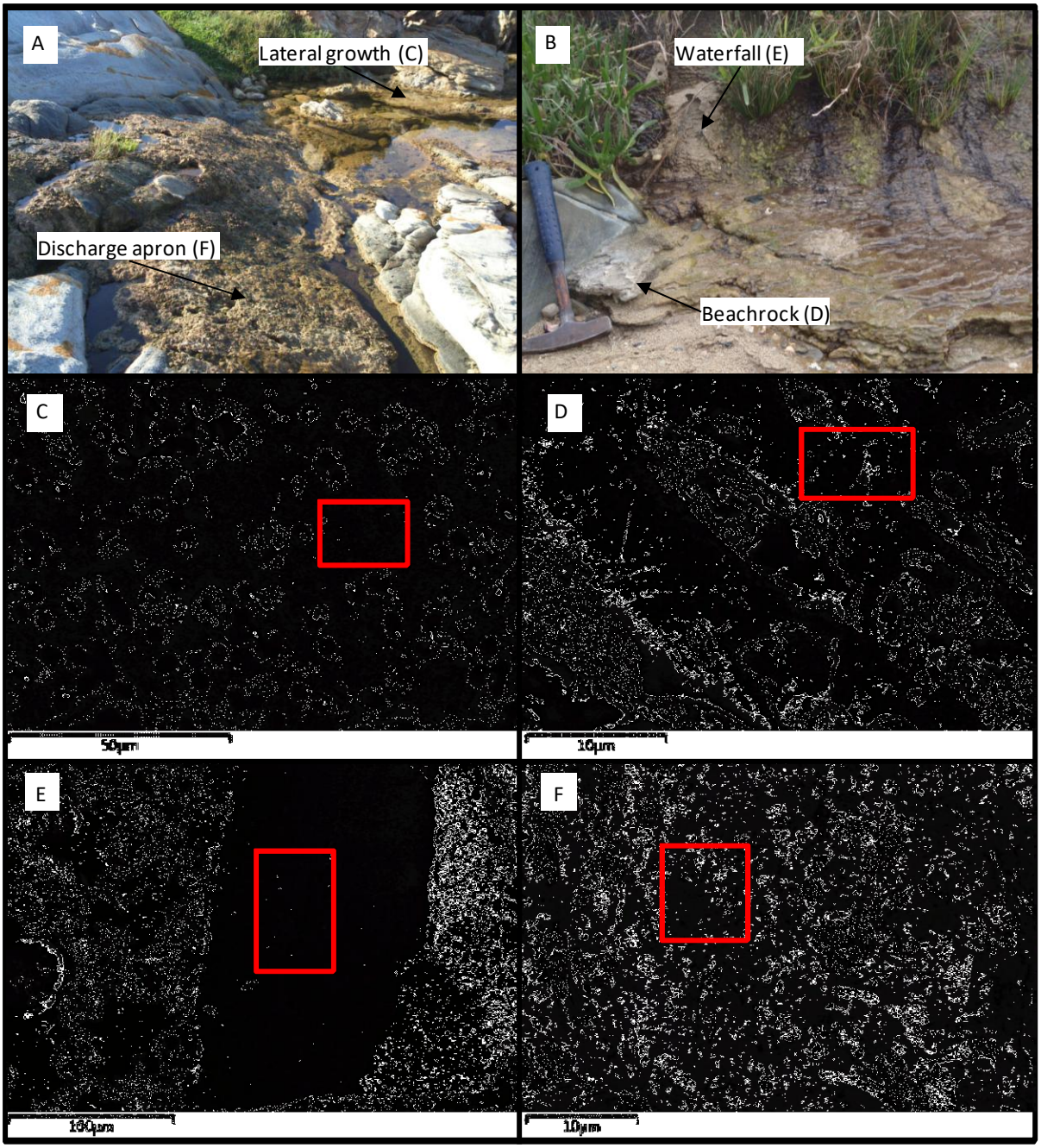

Fig. 2.2 An example of the various tufa samples collected (A and B) and the internal micro-fabrics (C-F) that were analysed. Typical sample areas from the various crust types are demarcated by red rectangles. A) A field image showing lateral growth at a barrage pool (C) and a discharge apron (F). B) A photograph of a waterfall deposit (E) and beachrock (B). C) A laminar flat barrage pool sample showing abundant filament casts. D) A beachrock sample showing presence of filament casts. E) An area lacking filament casts in a wrinkled laminar waterfall deposit. F) A discharge apron sample showing an area deficient of bacterial casts.

Table 2.5. SEM/EDS analysis of the carbonate matrix of each tufa type found within the three study sites. Crust type identified by presence (type 1) or lack (type 2) of filamentous bacterial casts. All values expressed as element wt%. All empty cells are taken as 0 %wt.

Sample	Category	Type	Crust	O	Ca	Mg	Si	Sr	Na	Cl	S
SEMC1	Fresh	Waterfall - Wrinkled laminar	Type 1	55,17	44,20	0,31			0,14		0,19
			Type 2	55,53	43,60	0,45			0,46		
SEMC2	Fresh	Beachrock - laminar flat	Type 1	53,03	45,58	0,51			0,29	0,34	0,25
			Type 2	53,91	45,32	0,49			0,12		0,15
SEMC3	Mixed	Barrage pool - Laminar flat	Type 1	53,68	45,28	0,39			0,24	0,18	0,23
			Type 2	52,03	47,17	0,55					0,25
SEMC4	Mixed	Discharge apron - Colloform	Type 1	56,19	40,88	1,98			0,47	0,27	0,20
			Type 2	55,00	42,48	1,85			0,32	0,14	0,21
SEMC5	Mixed	Discharge apron - Laminar flat	Type 1	52,89	45,85	0,66			0,25		0,35
			Type 2	52,52	46,33	0,79			0,18		0,18
SEMC6	Marine	Barrage pool - rimstone	Type 1	56,05	41,46	1,84		0,15	0,26		0,85
			Type 2	54,77	43,28	0,31		0,91	0,44		0,29
SEMC7	Marine	Barrage pool - rimstone	Type 1	54,53	40,43	2,68	0,98	0,49	0,32		0,26
			Type 2	54,75	41,64	3,02		0,28	0,15		0,16

Table 2.6. SEM/EDS analysis of the inclusions observed in various tufa types. All values are expressed in element wt%.

Sample	Category	Type	Area	O	Ca	Na	Cl	Al	Si	Fe	Mg	Sr	Ti	S
SEMC1	Fresh	Waterfall - Wrinkled laminar	Diatom frustule	54,01	45,22						0,22	0,32		0,23
SEMC2	Fresh	Beachrock - Laminar flat	Cubic mineral	0,80	0,51	39,37	59,32							
SEMC4	Mixed	Discharge apron - Colloform	sub-rounded grain	54,35					45,65					
			sub-rounded grain	53,5	0,43	1,57		18,71	17,12	4,60	3,50		0,57	
SEMC6	Marine	Barrage pool - Rimstone	Shell fragment	57,64	41,25	0,45						0,66		
			sub-rounded grain	53,50					46,50					
SEMC7	Marine	Barrage pool - Rimstone	sub-rounded grain	52,50					47,50					
			sub-rounded grain	52,97					47,03					

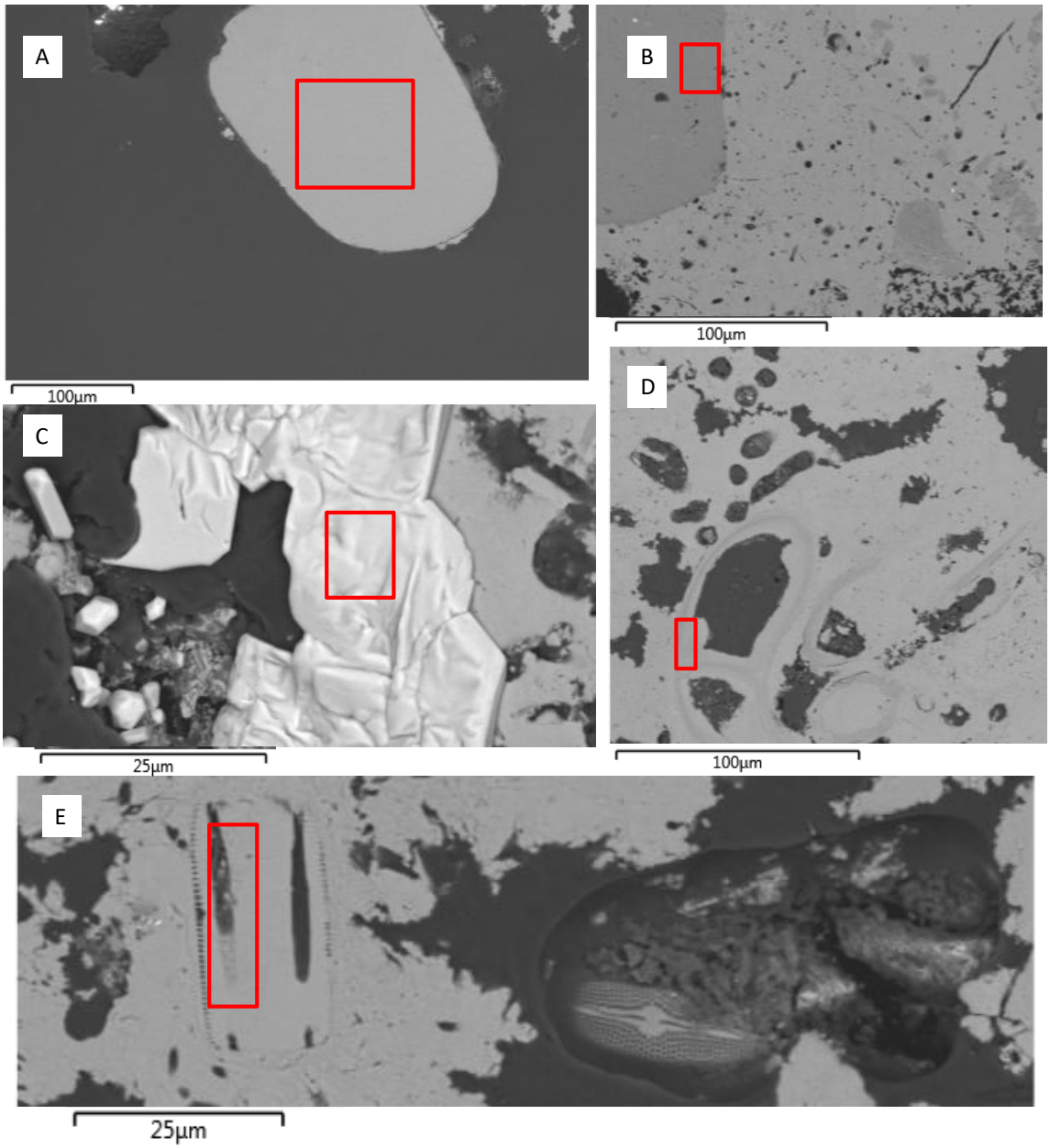

Fig. 2.3 Various inclusion found in the tufa samples analysed by SEM/EDS. Red rectangles demarcate the area sampled. A) A sub-rounded quartz grain partially trapped by tufa and surrounded by resin. B) A rimstone sample showing a quarts grain trapped and surrounded by tufa. C) Cubic halite found in a beachrock sample. D) A shell fragment or possibly a foram test found in a rimstone sample. E)Two diatoms found in a waterfall sample. The diatom on the left is trapped by tufa while the other is trapped in a bubble of resin and could not be analysed.

4. Discussion

4.1 Geochemical variation

The chemical make-up of the Eastern Cape tufa systems all have high CaO (XRF), Ca (SEM/EDS), and LOI values. This is in keeping with those expected from microbialite deposits precipitating from carbonate saturated waters (e.g. Dodd et al., 2018). The LOI values are due to CO_2 loss from the carbonates, organic matter (mostly microalgae Rishworth et al., 2017), and possibly hydrous mineral phases. The loss of water from the detrital component will be minor given that Al and Fe concentrations are generally < 1 %. The proportions of organic and inorganic C was not determined. Lower levels of Sr and Mg are also observed. These divalent ions are known to readily substitute into the crystal structure of calcite (e.g. Saunders et al., 2014; Finch and Allison, 2007). This is observed in both the XRF/LA-ICP-MS and SEM/EDS analyses, which confirms the identification of low-Mg calcite reported in Chapter 1.

The chemical analyses of the tufa material shows that the samples have varying amounts of detrital material. This is seen primarily through elevated levels of SiO_2, Al_2O_3, K_2O, Fe_2O_3, and TiO_2, which occur in minerals such as quartz, feldspar, mica, and possibly rutile/illmenite. A plot of these elements versus Al_2O_3 alllows for the interpretaion of the detrital component as Al_2O_3 forms part of the washed-in sedimentary grains and not part of the carbonate matrix. This plot (Fig. 2.4) shows positive correlations for all elements, while CaO exhibits a negative trend. These patterns relate to relative proportions of detrital material and calcium carbonate (tufa). The plots show that samples X3, X7, and X8 (rhizolith, rimstone, and rimstone respectively) contain relatively higher amounts of detrital sediment . The higher proportion of sediment in X3 is due to this rhizolith sample forming adjacent to soil horizons (Edwards, et al., 2017), while the two rimstone samples (X7 and X8) both had regular interaction with shore sediment. Given the results of the whole rock analyses, it is surprising that X-ray diffraction only identified quartz and feldspar in one active rimstone sample (XRD6; Chapter 1), suggesting low levels of sediment and/or heterogeneous samples. A few shell fragments and quartz grains were, however, observed in the rimstone samples during SEM analysis (Table 2.7). The remaining samples all had much lower concentrations of elements associated with detrital minerals. This is not unexpected as the coarser detrital

grains entering from the seeps will settle to the bottom of the pool, while some finer material may be incorporated into the lateral barrage pool growth. This dynamic also prevents seep sediment reaching the discharge apron. All of these samples may, on occasion, receive some marine sediment through wave over-topping. This may be responsible for the observed quartz and an unknown mineral grain observed in the discharge apron colloform sample using SEM/EDS (Table 2.7).

The remaining elements all show poorer correlations with Al_2O_3 (Fig. 2.4). The MgO variability in the plot is due to its incorporation into the crystal structure of the calcium-carbonate matrix, as confirmed by SEM and XRD analysis (Chapter 1), as well as possibe inclusion in detrital minerals. The scatter in the Na_2O data is a result of halite crystals in the samples, detrital material, and also possibly the inclusion of Na into the carbonate structure. Halite was identified in the beachrock sample (Table 2.7), and in all XRD samples in Chapter 1. As halite is an evaporite mineral, it would be expected in this supratidal environment. The calcite identified together with the halite (Fig. 2.3; Table 2.7) is probably beneath the halite and was not part of the crystal being analysed but rather an artefact of the way in which SEM/EDS determines the sample's chemistry. An electron beam penetrates the sample and interacts with the elements below the sample surfacebefore being ejected toward a sensor. This means that sample measurements may include elements from minerals adjacent to the intended target. The poor correlation of the P_2O_5 presumably relates to the heterogenous distribution of organic phosphorous in the sediment and/or detrital grains of monazite or apatite.

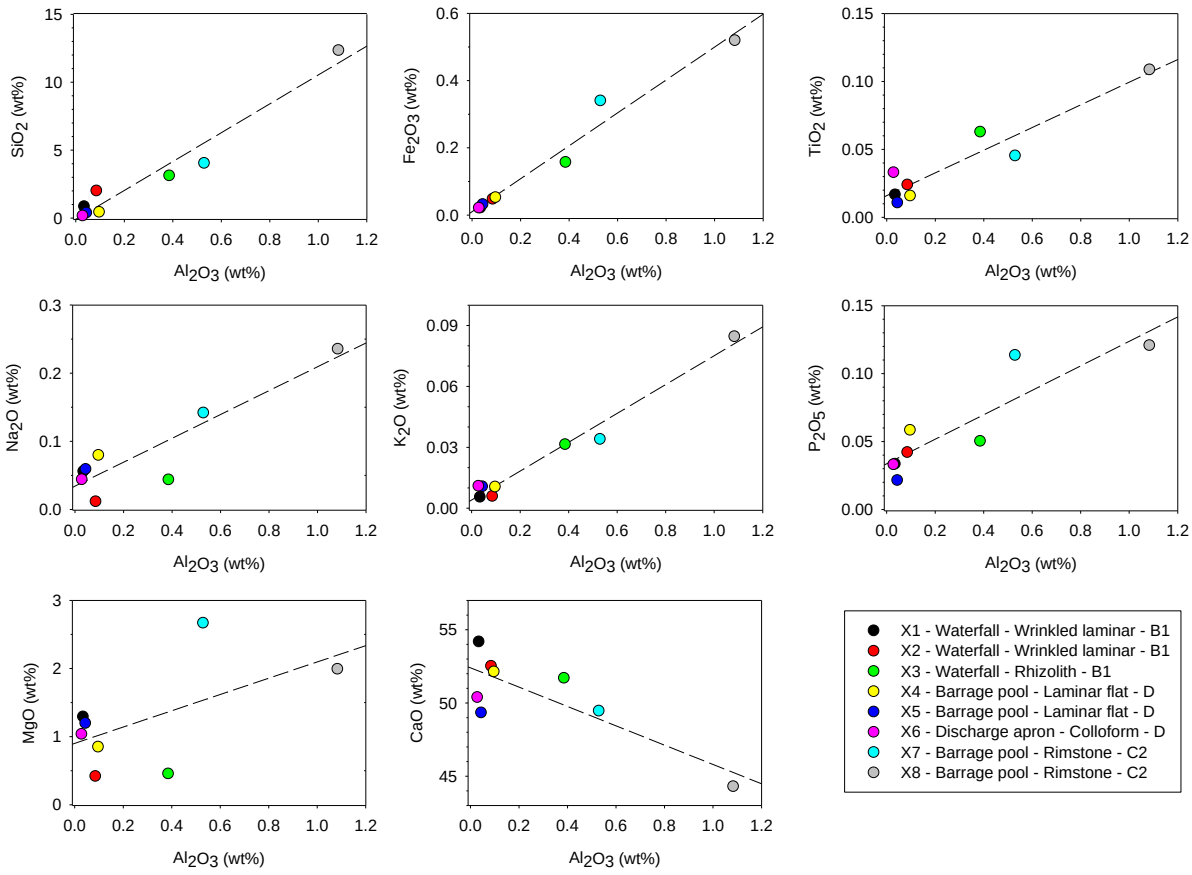

Fig. 2.4 Oxides detected by XRF plotted against Al_2O_3 showing effect of detrital material (sediment). Trend lines increase with all oxides other than CaO.

Table 2.7 Molar ratios of identified mineral inclusions in various tufa types from SEM/EDS data.

Sample	Category	Type	Area	O/Si	Na/Cl	O/C	Mineral ID -based on molar ratios
SEMC1	Fresh	Waterfall - wrinkled laminar	Diatom frustule			3.0	Calcite
SEMC2	Fresh	Beachrock - laminar flat	Cubic mineral		1.0	3.9	Halite/calcite
SEMC4	Mixed	Discharge apron - colloform	Sub-rounded grain	2.1			Quartz
			Sub-rounded grain	5.5		311.7	Unknown
SEMC6	Marine	Barrage pool - rimstone	Shell fragment			3.5	Calcite
			Sub-rounded grain	2.0			Quartz
SEMC7	Marine	Barrage pool - rimstone	Sub-rounded grain	1.9			Quartz
			Sub-rounded grain	2.0			Quartz

Selected major and trace elements are plotted to characterize the mineralogy controlling the elemental composition (Fig. 2.5). Similarly to Fig. 2.4, samples X3, X7, and X8 (rhizolith, rimstone, and rimstone respectively) all show increases in element abundance compared to the other samples. The reasonably good correlation between Zr and Hf is likely as the latter occurs in zircon, $(Zr_{0:99}Hf_{0:01})SiO_4$, (Bindeaux and Nichols, 2003). The REE elements (Ce, La, Nd, Y) and Th all show excellent correlations (r2 = 0.99 - 1.00), presumably as they all occur in the same mineral. This may be the heavy mineral monazite, $(Ce,La,Nd,Th)(PO_4,SiO_4)$, but given the good correlation of Ce to Al it is more likely a silicate (e.g. a mica or feldspar). The Zr-Al plot illustrates the relationship between the mineral zircon and the Al-silicates. This has a poor correlation, which is expected due to the effect of sorting and weathering of zircon in sediments, which differs to the Al-silicates, such as micas and/or feldspar.

A positive, but poor correlation is seen between Zr and Ce, as well as Zr and Ti. This is unexpected as usually a good correlation between the heavy minerals zircon, monazite, and the Ti bearing rutile and/or ilmenite would be observed. Given the better correlation between Al and Ti (Fig. 2.4), it is likely the Ti is present in silicates such as biotite or muscovite (e.g. Chambers and Kohn, 2012), while Ce (and other REEs) occurs in mica or feldspar. The contribution of the carbonates to the REE concentrations in the samples is unclear from the scatter plots.

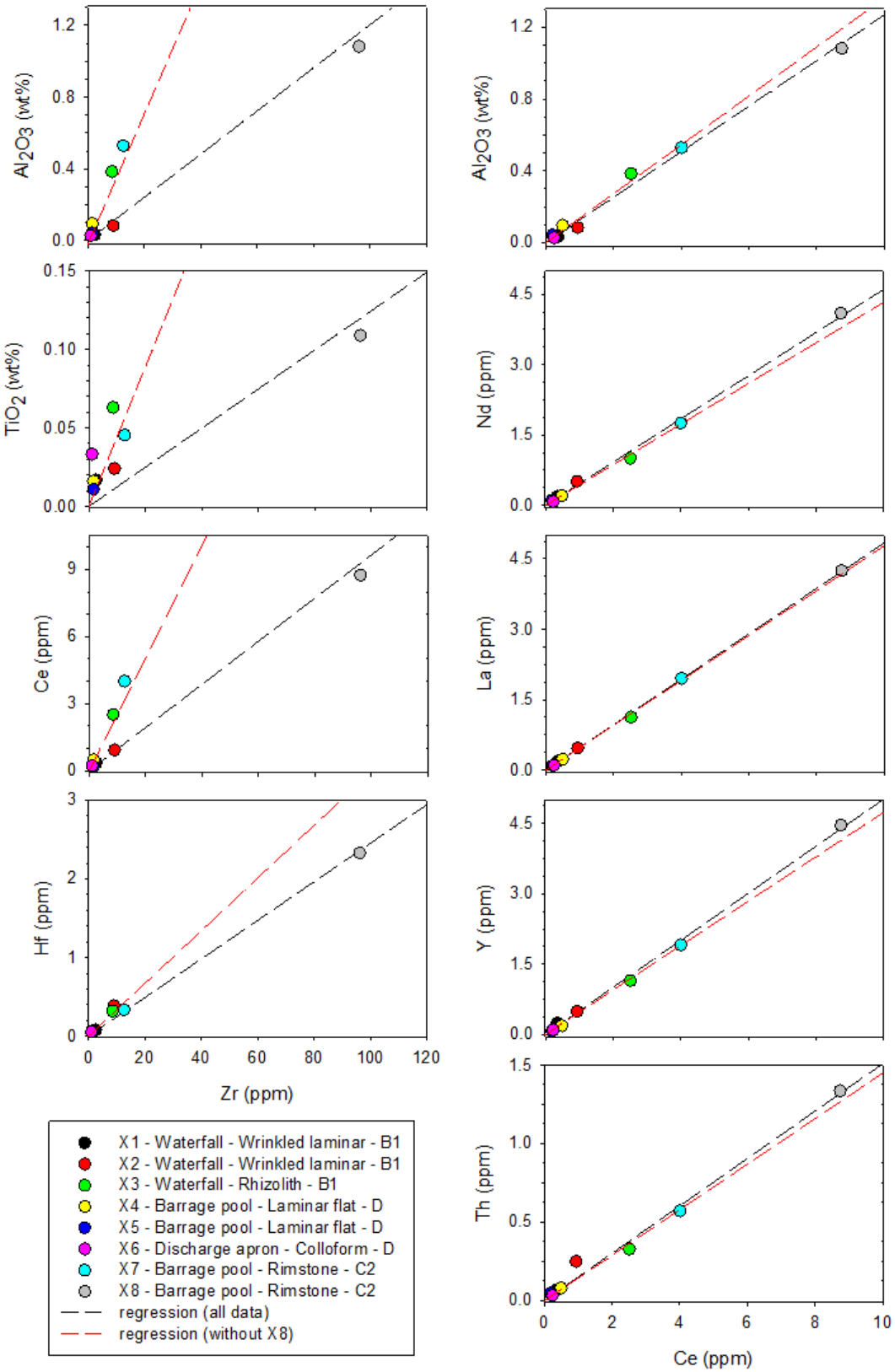

Fig. 2.5 Scatter plots of the trace element data showing the trace element distribution of the detrital minerals. Two regression lines are shown because sample X8 is very much higher than the others and can significantly influence correlations (black line = all data and red line = data excluding X8)

Major and trace element, as well as REE, spider plots (Fig. 2.5,Fig 2.6 and Fig. 2.7), normalised to PAAS (Post-Archaen Australian Shale), show the elemental distribution of the samples with respect to the elevation profiles. All major and trace elements show similar patterns that related to the underlying mineralogy. The Ca levels are elevated, as is expected in limestone, while major elements associated with detrital material, such as SiO_2, TiO_2, Al_2O_3, Fe_2O_3, Na_2O, and K_2O are depleted (Fig. 2.6). The slight MgO depletetion as well as the Sr enrichment is expected, as both are readily incorporated into the calcite structure (e.g. Saunders et al., 2014). The range seen in the trace element depletion relates to the variability in concentration of the detrital minerals (Fig. 2.6). A few of the trace metals in some samples deviated from the general pattern. With the exception of X4 (inactive wall growth), the levels of Zn showed little variation, while Pb levels for X4, X5, and X6 (inactive wall growth, active wall growth, and colloform respectively) are lower than expected. These anomalies may relate to organic matter, as both are readily complexed by organic ligands (Stumm and Morgan, 1996).

The Rare Earth Element patterns in this study are shown in Fig. 2.7. All REE show similar depletion to those reported for Cuatro Ciénegas Basin (Johannesson et al., 2014). A number of authors have suggested that uptake of REE can be used to infer depositional conditions of ancient deposits (e.g Chagas et al., 2016; Frimmel, 2009). In this study the three samples with the highest detrital content (X3, X7, and X8) show less depleted and flat REE patterns, presumabely due to the higher detrital component of these samples. The remaining samples are more depleted and all show a simlar saw tooth pattern, possibly related to lower levels of detrital minerals and relatively more REE contribution from the carbonates.

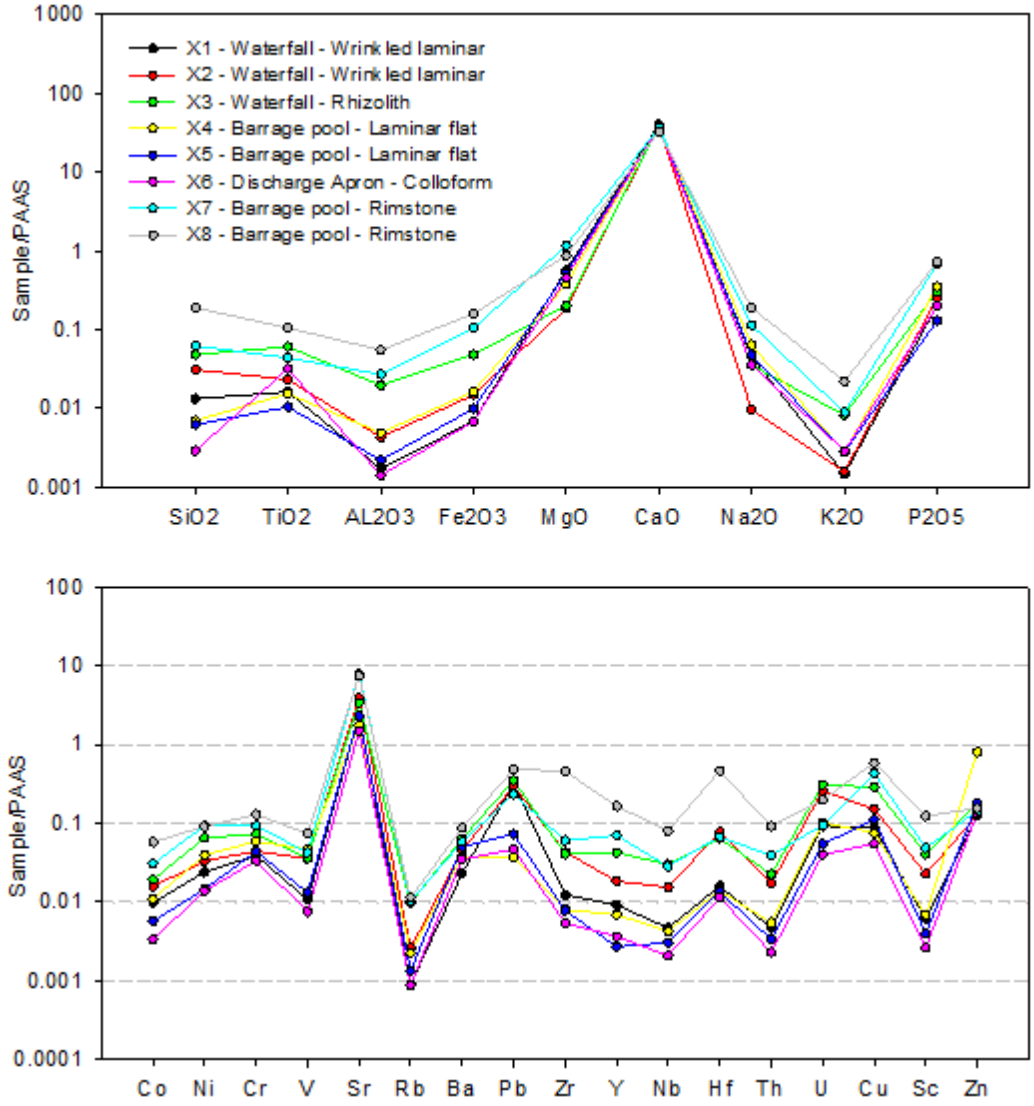

Fig. 2.6 Spider diagrams of the major and trace elements showing the distribution and effects of detrital sediment within the tufa systems. Results are normalised to Post-Archean Australian Shale (PAAS values after Nance and Taylor, 1976, as cited by Piper and Bau, 2013)

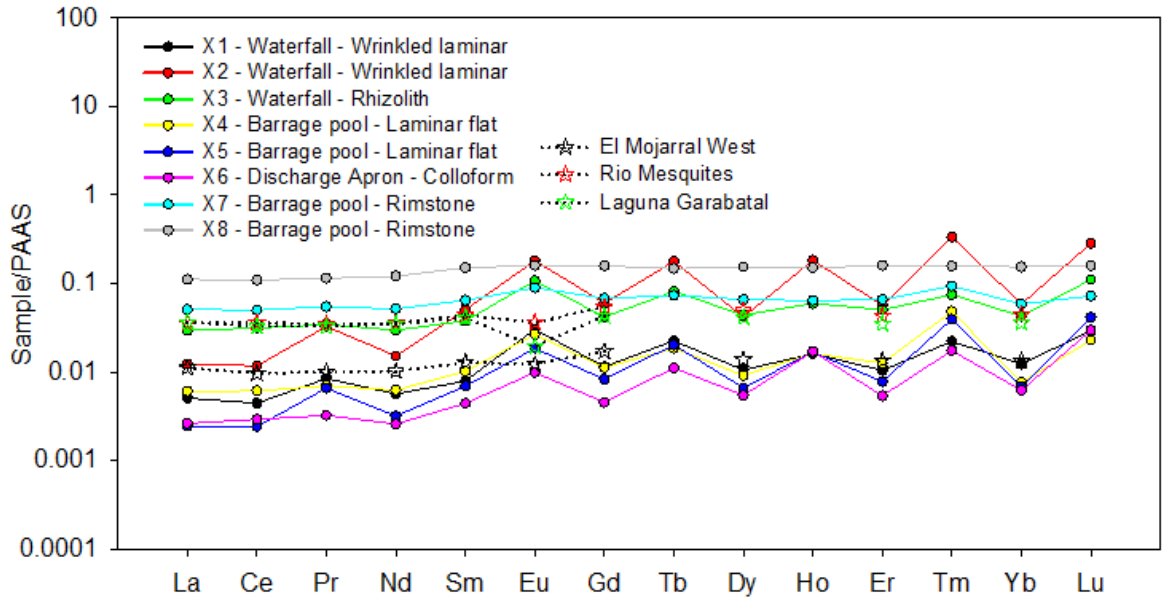

Fig. 2.7 REE patterns of the tufa systems near Port Elizabeth compared to those of Cuatro Ciénegas Basin (Data from Table 14.2 of Johannesson et al., 2014). Results have been normalised to Post-Archean Australian Shale (PAAS from Piper & Bau, 2013)

4.2 Rock and water chemistry

The Ca^{2+} content of the tufa water system near Port Elizabeth is shown to have an increasing trend towards more saline water (Dodd et al., 2018). Interestingly, the Ca^{2+} values have an inverse trend compared to Ca and CaO values measured in this study (Tables 2.3 and 2.5). Ca (SEM/EDS) and CaO (XRF) values both show an overall decrease from the fresh and mixed tufa towards the marine samples. This general increase in the Mg levels of the tufa samples is better seen using molar ratios (Table 2.8 and 2.9) and is readily explained in terms of the chemistry of the water flowing through the microbialite system

The Mg^{2+} content of water shows a rapid increase in concentration as fresh and marine water mix (Dodd et al., 2018). The higher levels of Mg^{2+} in the mixed and marine waters are responsible for increased uptake of Mg into the carbonates. The Ca^{2+} values for the marine and mixed water are lower than the corresponding Mg^{2+} values, which results in the tufa system being oversaturated with respect to Mg-bearing minerals, such as dolomite ($CaMg(CO_3)_2$) and huntite ($Mg_3Ca(CO_3)_4$) (Dodd et al., 2018). The XRF and SEM/EDS results do not confirm these model calculations, with only minor concentrations of MgO and no dolomite precipitation, respectively. This anomaly may be explained by the influence of exopolymeric substances (EPS) on the precipitation processes of carbonate minerals (e.g.

Braissant et al., 2007). EPS is shown to have a strong influence on precipitation and a tendancy to favour ions with a low charge (Ca^{2+}) over ions with a higher charge (Mg^{2+}) (Rogerson et al., 2008). This therefore explains why despite the water having a high Mg content and the capacity to precipitate Mg minerals, the tufa system predominantly forms low-Mg calcite.

Table 2.8 Molar ratios of the carbonate matrix of each tufa type found in the study area, as identified by SEM/EDS.

Sample	Category	Type	Crust	Mg/Ca (mmol/mol)	Sr/Ca (mmol/mol)	Na/Ca (mmol/mol)	Na/S (mol/mol)
SEMC1	Fresh	Waterfall - wrinkled laminar	Type 1	11,6		5,5	1,0
			Type 2	17,0		18,4	
SEMC2	Fresh	Beachrock - laminar flat	Type 1	18,5		2,7	0,4
			Type 2	17,8		4,6	1,1
SEMC3	Mixed	Barrage pool - laminar flat	Type 1	14,2		4,7	0,7
			Type 2	19,2			
SEMC4	Mixed	Discharge apron - colloform	Type 1	79,9		12,6	2,1
			Type 2	71,8		9,4	1,5
SEMC5	Mixed	Discharge apron - laminar flat	Type 1	23,7		9,5	1,0
			Type 2	28,1		6,8	1,4
SEMC6	Marine	Barrage pool - rimstone	Type 1	73,2	1,7	10,9	0,4
			Type 2	11,8	9,6	17,7	2,1
SEMC7	Marine	Barrage pool - rimstone	Type 1	109,3	5,5	13,8	1,7
			Type 2	119,6	3,1	6,3	1,3

Table 2.9 Molar ratios of elements identified by bulk rock XRF, in each tufa type, showing increased values for the rimstone samples

Sample	Site	Type	Category	Mg/Ca (mmol/mol)	Sr/Ca (mmol/mol)	Na/Ca (mmol/mol)
X1	B1	Inactive waterfall deposit	Fresh	33,3	0,55	1,9
X2	B1	Active waterfall deposit	Fresh	11,2	0,95	0,4
X3	B1	Rhizolith	Fresh	12,4	0,84	1,5
X4	D	Inactive wall growth	Mixed	22,7	0,43	2,8
X5	D	Active wall growth	Mixed	33,8	0,59	2,2
X6	D	Active colloform	Mixed	28,7	0,38	1,6
X7	C	Inactive rimstone	Marine	75,1	2,03	5,2
X8	C	Active rimstone	Marine	62,7	2,14	9,6

The precipitation of low-Mg calcite in microbialites has been suggested to indicate low salinity and Mg/Ca ratios < 0.8 for the source water (Chagas et al., 2016). The peritidal microbialite systems near Port Elizabeth were shown to have a range of Mg/Ca ratios from 0.15 – 0.21 in the fresh water inlets to 3.12 in the marine water (Dodd et al., 2018). These microbialites are predominantly composed of low-Mg calcite (Chapter 1) and precipitate largely from the freshwater portion of the system (Edwards et al., 2017), thus aligning well with the suggestion by Chagas et al. (2016). This provides further evidence that hydrochemical conditions can be inferred by the mineralogy of tufa microbialites. The tufa samples analysed in this study are thought to be fairly recent deposits and therefore may undergo mineralogical changes over time due to further diagenesis. Ancient microbialites precipitating from similar source waters may therefore show a variable mineralogy to that of these deposits.

Sr, and Na to Ca, as well as Na/S molar ratios as detected by SEM/EDS and XRF are provided in Table 2.8 and Table 2.9 respectively. Sr was only detected by SEM/EDS in the marine samples, which have a high Mg content. This is not unusual as Sr uptake in magnesium calcite increases with Mg content (Mucci and Morse, 1983). Interestingly, the highest Sr/Ca ratio corresponds to one of the lowest Mg/Ca ratios and the discharge apron samples have a high Mg content but no Sr/Ca ratio. This may be an effect of insufficient detection limits of SEM/EDS, or sample heterogeneity. Sr detection in the carbonate matrix show that it is likely incorporated into the calcite structure, although the ratios are questionable. High Sr/Ca ratios in the high detrital samples (rimstone samples X7 and X8 in Table 2.9) show that Sr is in both the carbonate and detrital minerals. Two sources are likely also for sodium. Molar concentrations of Na exceed those of chlorine, thus any excess after subtracting that in halite presumabely forms part of the carbonate matrix. Yoshimura et al. (2017) reported a variety of altervalent substitutions for Na into biogenic calcite; substitution of a trivalent cation/anion lattice vacancies, substitution with bicarbonate, vacancies and interstitial substitutions, or $2Na^{+}$ substitution for Ca^{2+} with structural substitution of SO_4^{2+} or SO_3^{2+} for CO_3^{2+}. The positive Na/S ratios in Table 2.8 suggest that $2Na^{+}$ is being substituted for Ca^{2+} together with a substitution of SO_4^{2+} or SO_3^{2+} for CO_3^{2+}. The chemical setting, and the incorporation of Na into biogenic calcite is, however, still being debated.

4.3 Similar deposits

The tufa deposits in this study have been shown to be similar with regards to environmental setting, mineralogy and morphology (e.g. Edwards et al., 2017 and Chapter 1) to supratidal tufa deposits in South West Australia (Forbes et al., 2010).. This suggests that a similar elemental composition to the tufa deposits in this study may also occur at the Australian sites, although the water chemistries differ (Dodd et al., 2018).

XRF results in this study reveal similar CaO, LOI, MgO, and Na values to the supratidal Australian tufa deposits (e.g. Forbes et al., 2010). The SiO_2 values are shown to be slightly more erratic here, and this is likely the result of varying interactions with siliceous sediments (from a marine origin) at the two sites. Similar variability may also explain the levels of Al_2O_3, Fe_2O_3, and TiO_2 in the XRF results of this study, while they are not reported by Forbes et al. (2010). Alternatively, the lack of these elements may be explained by a higher detection limit of the XRF instrument used by Forbes et al. (2010).

The trace elemental analysis of the South West Australian tufa sites only reported Sr and As, with all others below 20 ppm (Forbes et al., 2010). LA-ICP-MS results of this study show a similar Sr range (300–1500 ppm) but no values are given for As. Other elements (Ba, Cu, Zn, and Zr) also occur here in values above 20 ppm. Ba is consistently above 20 ppm while Cu, Zn, and Zr are commonly below this threshold. The remaining trace elements recorded in this study fall well below the 20 ppm mark.

Elemental ratios of Mg, Sr, and Na to Ca in this study (XRF and SEM/EDS) are compared to XRF results from South West Australia (Forbes et al., 2010) (Fig. 2.8). These elements are used for comparison purposes as they make up the bulk of the major elements identified in the two studies. Elemental ratios are used as they negate the effects of the detrital component. The values in this study all fall within similar ranges to those of Forbes et al. (2010), although the rimstone SEM/EDS samples are consistently higher in this study. This shows further comparability between these deposits. The Mg/Ca and Na/Ca values are only slightly higher and could still be considered to be in the same range. The Sr/Ca ratios, however, are much higher and could be a result of varying detection limits of the two analytical methods (XRF vs SEM/EDS). Sr is detected in all samples by LA-ICP-MS (Table 2.4), however, the samples analysed via SEM/EDS only show Sr in the marine samples (Table 2.5).

The Sr levels of the fresh and mixed samples shown in Table 2.4 are significantly lower than the marine samples, and there are no Sr values for the same sample types in Table 2.5. This inconsistency may be due to the relatively restricted detection limit of SEM/EDS compared to LA-ICP-MS, demonstrating the usefulness of using complementary techniques in such analyses.

Despite all these elemental similarities, the deposits in South West Australia are reported to be made up largely of calcite with only minor amounts of Mg-calcite (Forbes et al., 2010), in contrast to this study that found mostly low Mg-calcite. This difference may be due to the variable sample preparation or XRD interpretation of the two studies, and can be tested by examining samples from both sites using identical XRD methods.

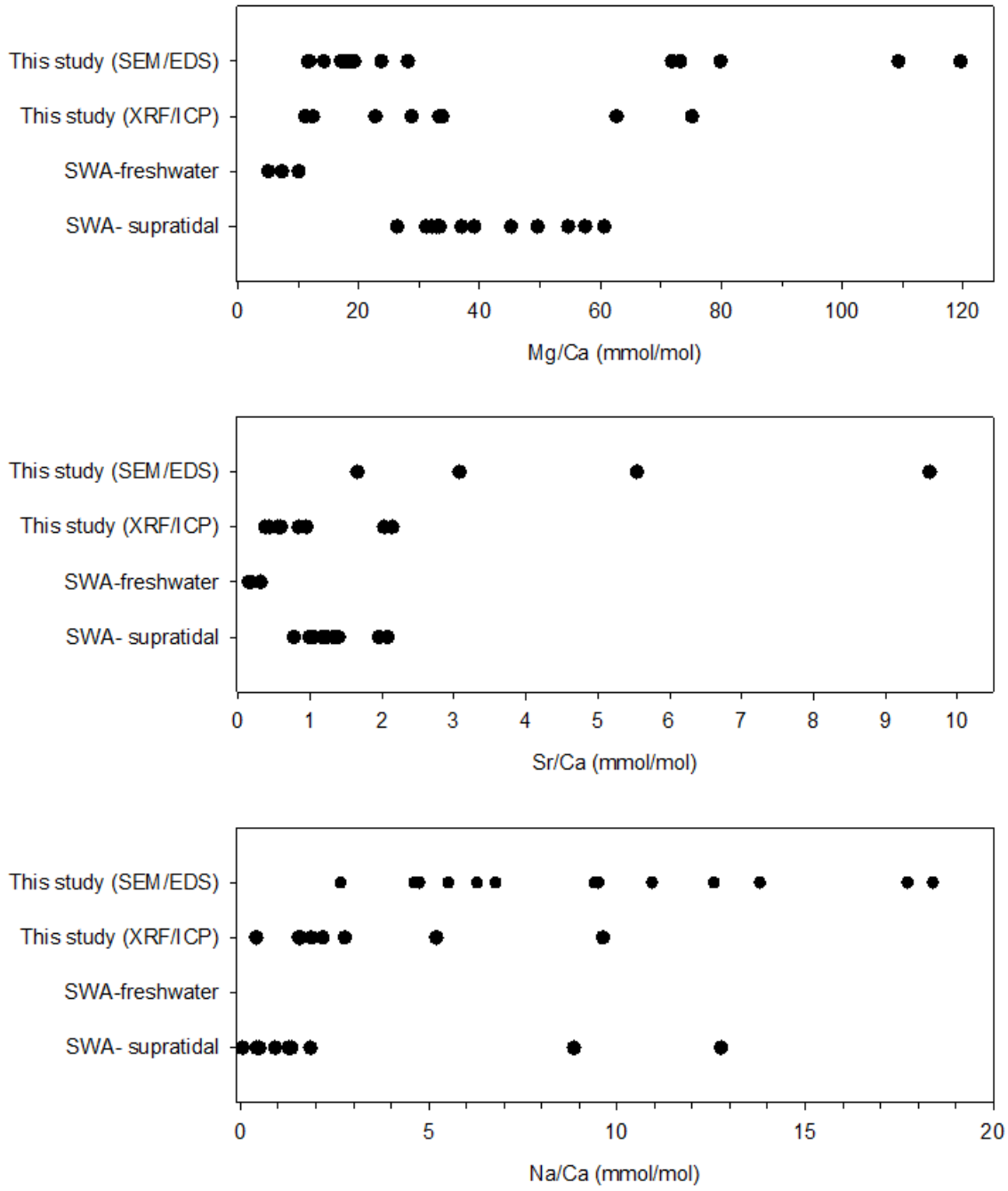

Fig. 2.8 Molar ratios of Mg, Sr, and Na to Ca of the tufa as identified by SEM/EDS and XRF compared to XRF data from similar deposits in South West Australia (SWA). Data taken from Forbes et al., (2010). SWA-supratidal are the Contos springs, Quarry Bay, and Canal Rocks sites, and SWA-freshwater is the Meekadarribee Falls site.

5. Conclusion

Chemical investigations of the tufa microbialites near Port Elizabeth have revealed an elemental dominance by Ca, CO_3 and Mg, in the form of low Mg-calcite as well as Sr. A comparison of bulk rock chemistry to specific area analysis has also shown that while other elements, such as Si, Al, Fe, Ti, Na, and Cl, are often entrapped in the tufa, they do not form part of the tufa matrix. Instead these elements occur in trapped sedimentary grains or minor evaporite minerals (Table 2.6).

Elemental molar ratios show increasing trends toward more marine tufa for many elements (especially Mg). These trends are explained by the interaction with increased amounts of sedimentary products and/or interaction with more saline water that contains a higher TDS (e.g. Dodd et al, 2018). Such patterns in tufa chemistry may be used for paleontological reconstructions. Sr, Na, and Mg to Ca ratios are also important as they may indicate elemental patterns as well as mineralogy and salinity conditions (Mg/Ca). Conducting similar chemical investigations along tufa profiles using larger sample sets may provide more insight into the exact mechanisms of these elemental variations.

The two types of crust present in the tufa, interestingly showed very little overall elemental variation (Table 2.5). This may be due to the constant change in water chemistry conditions experienced by the microbialite system (e.g. wave or tide action, rainfall events and/or seasonal change). An argument could be made that in order to accurately measure any chemical variation in the crust type they should be separated before the analysis. If one were to separate enough of each crust type then LA-ICP-MS analyses could be conducted separately and possibly reveal further trace element variation between the crust types. This would provide key information on effects of the organic matter in type 1 crust on the elemental contribution of the carbonate matrix.

The tufa deposits near Port Elizabeth are comparable to those in South West Australia, Northern Ireland, and Morgan's Bay (Edwards et al., 2017). Here the tufa is shown to be similar, in terms of the dominant elements (Ca and, to a lesser extent, Mg and Sr), to the Australian deposits in spite of subtle dissimilarities in water chemistry (e.g. Dodd et al., 2018). Elemental ratios (Mg, Sr, and Na to Ca) in this study are in a similar range to the Australian deposits. This and the slight disparities in the minor elemental make-up of the

tufa systems may be explained by the difference in hydrochemistry and sediment chemistry of the two tufa systems. This may also be the reason for the dominant mineral discrepancy (low-magnesium calcite in this study and calcite in the Australian tufa). The tufa deposits occurring at Giant's Causeway, Northern Ireland and Morgan's Bay, South Africa have not yet been investigated in this regard, therefore making a future comparison highly recommended.

General conclusions and future work

This micro-fabric, mineralogical and geochemical study has provided important information on the microbialite systems near Port Elizabeth. Essentially, the main findings are that these deposits are made-up of various micro-facies consisting primarily of low-Mg calcite matrix, organic matter, various trapped sediments.. This suggests that the deposits be classified as 'tufa microbialites' rather than the previously suggested 'tufa stromatolites'. The calcitic matrix of the tufa is shown to incorporate Mg, Sr, and some Na into the carbonate structure, while other elements are mostly present in detrital grains. The exact concentrations of the detrital material and the carbonate need to be properly quantified. The elemental ditributions, of the detrital phases, increased down the tufa profiles and were shown to depend on increasing interaction with shoreline sediments. Many of the above findings were only demonstrated because two or more analytical techniques were utilised, showing the importance of combining data from various analyses.

Using both the mineralogical (XRD) and elemental (XRF, LA-ICP-MS, SEM/EDS) analyses has allowed the scrutinisation of the major and trace element distributions along the tufa profiles. Some of these techniques have also complemented each other and confirmed findings, such as the precipitation of low-Mg calcite. SEM/EDS results strengthened the elemental analysis by XRF, as they were able to identify elemental concentrations of the carbonate matrix and the mineral inclusions separately. This showed the presence of Mg, Sr, and Na in the carbonate matrix as well as the detrital material, as well as confirmed the increasing trends of Mg, Na and, Sr toward more marine water. These complementary analytical techniques have deciphered not only the mineralogical and elemental contributions of the carbonate matrix but also the effects of detrital sediments. Analysing these effects will improve the results of any future studies conducted on the micro-fabrics, mineralogy, and chemistry of these and other tufa deposits.

The geochemical analysis of the microbialite systems in this study shows that detrital material has a significant influence on the geochemistry of the tufa microbialites. This study also speculates on the mineral make-up of this detrital material based on trace element correlations, but does not sufficiently determine the source of these trace elements. These minerals may be observed by dissolving the carbonate matrix and examining the residue.

Dissolving the tufa samples should leave behind all grain inclusions, which could then be filtered out. The residue could then be inspected using SEM analyses in order to identify minerals and trace element sources in the tufa deposits. This may also help to differentiate between trace elemental portions of the tufa and the trapped detrital sediment.

Previous studies of modern and ancient microbialites have suggested using mineralogical and elemental data to infer water conditions. For example, the precipitation of low-Mg calcite indicates low salinity and Mg/Ca ratios < 0,8 for the source water (Chagas et al., 2016). This study shows the potential to apply these techniques to peritidal microbialites because their salinity,Mg/Ca ratios and mineralogy, all correspond to these suggestions. Given that this study is conducted on modern microbialites only, mineralogical changes may occur over time (e.g. Yoshimura et al., 2017) and further research is required to analyse the possibility of using these methods on ancient peritidal microbialites.

Further analyses could be used in conjunction with the results of this study in order to more accurately detail the microbialite fabrics. Analysing the LOI, for example, may improve the trace element and REE data. LOI is known to consist of carbonate, organic matter and hydrous mineral phases (Craft et al., 1991) but the proportions of each, here, have not been identified. Reporting on the concentrations of each of these constituents may improve the data normalisation and lead to higher concentrations of some elements. More accurate elemental data will provide greater opportunity for comparison to other studies and similar deposits.

This study also shows that well-calcified tufa samples display a larger range of crystal forms, partially controlled by filamentous bacteria, compared to the poorly calcified samples. The crystal forming process and evolution are, however, not well understood. Calcite needles (NFC) are thought to precipitate within bacterial sheaths and then released upon decay, but no such sheaths were observed here. Examining fresh, non-dried, samples using a TEM (Transmission Electron Microscope) or a CTEM (Conventional Transmission Electron Microscope) may provide an opportunity to view these sheaths. Using a range of poorly calcified to well calcified samples may also add insight into the inolvment of bacterial decay on the rod release process and the crystal evolution of the microbialite deposits.

Ultimately, this dissertation demonstrates some important advances in the interpretation of modern microbialites. It also provides the potential for a comparisonto their ancient counterparts, using detailed mineralogical analyses. Further work is however clearly needed to elucidate the patterns of mineralogical decay or transformation to accurately interpret the fossil record, or even to search for signs of extraterrestrial microbialite evidence.

References

Aitken, J. D. 1967. Classification and environmental significance of cryptalgal limestones and dolomites with illustrations from the Cambrian and Ordovician of southwestern Alberta. *Sedimentary Petrology, 37(4)*, 1163-1178. doi.org/10.1306/74D7185C-2B21-11D7-8648000102C1865D

Andrews, J. E., & Brasier, A. T. 2005. Seasonal records of climate change in annually laminated Tufas: short review and future prospects. *Journal of Quaternary Science, 20(5)*, 411-421. doi.org/10.1002/jqs.942

Azulay, D. N., Abbasi, R., Ktorza, I. B., Remennik, S., Reddy, A., & Chai, L. 2018. Biopolymers from a bacterial extracellular matrix affect the morphology and structure of calcium carbonate crystals. *Crystal growth & design, 18(9)*, 5582-5591. doi/10.1021/acs.cgd.8b00888

Baumgartner, L. K., Spear, J. R., Buckley, D. H., Pace, N. R., Reid, P., Dupraz, C., & Visscher, P. T. 2009. Microbial diversity in modern marine stromatolites, Highborne Cay, Bahamas. *Environmental Microbiology, 11(10)*, 2710-2719. doi: 10.1111/j.1462-2920.2009.01998.x

Benzerara, K., Meibom, A., Guatier, Q., Kameirczak, J., Stolarski, J., Menguy, N., & Brown, G. 2010. Nanotextures of aragonite in stromatolites from the quasi-marine. *The Geological Society of London*, 336(10), 211-224. doi: 10.1144/SP336.10

Bernhard, J. M., Edgcomb, V. P., Visscher, P. T., McIntyre-Wressnig, A., Summons, R. E., Bouxsein, M. L., Louis, L., Jeglinski, M. 2013. Insights into foraminiferal influences on microfabrics of microbialites at Highborne Cay, Bahamas. *Proceedings of the National Academy of Sciences of the United States of America*, 110(24), 9830-9834. doi: 10.1073/pnas.1221721110

Bindeaux, A., Nichols, B. 2003. Handbook of Mineralogy, vol. 2, Mineral Data Publishing, *Mineralogical society of America*.

Bindschedler, S., Gailleau, G., Braissant, O., Milliere, L., Job, D., & Verrecchia, E. P. 2014. Unravelling the enigmatic origin of calcitic nanofibres in soils and caves: purely physicochemical or biogenic processes? *Biogeosciences*, 2809-2825.

Bolhar, R., & Van Kranendonk, M. J. 2007. A non-marine depositional setting for the northern Fortescue Group, Pilbara Craton, inferred from trace element geochemistry of stromatolitic carbonates. *Precambrian Research*, 229-250.

Braissant, O., Decho, A. W., Dupraz, C., Glunk, C., Przekop, K. M., & Visscher, P. T. 2007. Exopolymeric substances of sulfate-reducing bacteria: Inter- actions with calcium at alkaline pH and implication for formation of carbonate minerals. *Geobiology*, 5(4), 401-411. doi: 10.1111/j.1472-4669.2007.00117.x

Burne, R. V., & Moore, L. S. 1987. Microbialites; organosedimentary deposits of benthic microbial communities. *Palaios*, 2(3), 241-254. doi: 10.2307/3514674

Cailleau, G., Verrecchia, E. P., Braissant, O., & Emmanuel, L. 2009. The biogenic origin of needle fibre calcite. *Sedimentology*, 56(6), 1858-1875. doi: 10.1111/j.1365-3091.2009.01060.x

Canveras, C. J., Cuezva, S., Sanchez-Moral, S., Lario, J., Laiz, L., Gonzalez, J., & Saiz-Jimenez, C. 2006. On the origin of fiber calcite crystals in moonmilk deposits. *Naturwissenschaften*, 93(1), 27-32. doi: 10.1007/s00114-005-0052-3

Chambers, J.A., Kohn, M.J. 2012. Titanium in muscovite, biotite, and hornblende: Modeling, thermometry, and rutile activities of metapelites and amphibolites. *American Mineralogist*, 97(4), 543-555. doi: 10.2138/am.2012.3890

Chagas, A. A., Webb, G. E., Burne, R. V., & Southam, G. 2016. Modern lacustrine microbialites: Towards a synthesis of aqueous and carbonate geochemistry and mineralogy. *Earth-Science Reviews*, 162, 338-363. doi: 10.1016/j.earscirev.2016.09.012

Cooper, J., Smith, A., & Arnscheidt, J. 2013. Contemporary stromatolite formation in high intertidal rock pools,Giants's Causeway, Northern Ireland: preliminary observations. *Journal of Coastal Research 65*, 65(2), 1675-1680. doi: 10.2112/SI65-283.1

Council for Geoscience., 2000a. [Map] 3325CD Uitenhage, 1:50 000 Geological series. Pretoria: Council for Geoscience.

Council for Geoscience., 2000b. [Map] 3425AB Uitenhage, 1:50 000 Geological Series.Pretoria: Council for Geoscience.

Craft, C.B., Seneca, E.D., Broome, S.W., 1991. Loss on ignition and Kjeldahl digestion for estimating organic carbon and total N in estuarine marsh soils: calibration and dry combustion, *Estuaries*, 14(2), 175–179. doi: 10.2307/1351691

Dodd, C., Anderson, C. R., Perissinotto, R., du Plooy, S. J., & Rishowrth, G. M. 2018. Hydrochemistry of peritidal stromatolite pools and associated freshwater inlets along the Eastern Cape coast, South Africa. *Sedimentary Geology*, 373, 163-179. doi: 10.1016/j.sedgeo.2018.06.002

Edwards, M.J.K., Anderson, CR., Perissinotto, R., Rishworth, G.M., 2017. Macro- and meso-fabric structures of peritidal tufa stromatolites along the Eastern Cape coast of South Africa. *Sedimentary Geology*, 359, 62–75. doi:10.1016/j.sedgeo.2017.08.006

Finch, A. A., & Allison, N. 2007. Coordination of Sr and Mg in calcite and aragonite. *Journal of Mineral Science*, 71(5), 539-552. doi: 10.1180/minmag.2007.071.5.539

Forbes, M., Vogwill, R., & Onton, K. 2010. A characterisation of the coastal tufa deposits of south-west Western Australia. *Sedimentary Geology*, 232(1-2), 52-65. doi: 10.1016/j.sedgeo.2010.09.009

Ford, T.D., Pedley, H.M., 1996. A review of tufa and travertine deposits of the world. *Earth Science Reviews*, 41(3-4), 117-175. doi: 10.1016/S0012-825(96)00030-X

Frimmel, H. E. 2009. Trace element distribution in Neoproterozoic carbonates as a palaeoenvironmental indicator. *Chemical Geology*, 258(2-4), 338-353. doi: 10.1016/j.chemgeo.2008.10.033

Garnett, E. R., Andrews, J. E., Preece, R. C., & Dennis, P. F. 2004. Climatic change recorded by stable isotopes and trace elements in a British Holocene tufa. *Journal of Quaternary Science*, 19(3), 251-262. doi:10.1002/jqs.842

Grotzinger, J. P. 1990. Geochemical model for Proterozoic stromatolite decline. *American Journal of Science*, 290-A, 80-103.

Gruszczynski, M., Kowalski, B. J., Soltysik, R., & Hercman, H. 2004. Tectonic origin of the unique Holocene travertine from the Holy Cross Mts.: microbially and abiologically mediated calcium carbonate, and manganese oxide precipitation. *Acta Geologica Polonica*, 54(1), 61-76.

Hofmann, H. J., Grey, K., Hickman, A. H., & Thorpe, R. I. 1999. Origin of 3.45 Ga coniform stromatolites in Warrawoona Group, Western Australia. *GSA Bulliten*, 111(8), 1256-1262.

Janssen, A., Swennen, R., Podoor, R., & Keppens, E. 1999. Biological and diagenetic influence in recent and fossil tufa deposits from Belgium. *Sedimentary Geology*, 126(1-4), 75-95. doi: 10.1016/S0037-0738(99)00033-0

Johannesson, K.H., Telfeyan, K., Chevis, D.A., Rosenheim, B.E., Leybourne, M.I., 2014. Rare earth elements in stromatolites—1. Evidence that modern terrestrial stro- matolites fractionate rare earth elements during incorporation from ambient waters.In: Dilek, Y.,Furnes, H. (Eds.),Evolution of ArcheanCrust andEarly Life. Modern Approaches in Solid Earth Sciences. *Springer*, Netherlands, pp. 385–411. doi: 10.1007/978-94-007-7615-9_14

Jones, B., & Renaut, R. 2010. Calcareous Spring Deposits in Continental Settings. *Developments in Sedimentology*, 61, 177-224. doi: 10.1016/S0070-4571(09)06104-4

Kano, A., Matsuoka, J., Kojo, T., & Fujii, H., 2003. Origin of annual laminations in tufa deposits, southwest Japan. *Palaeogeography, Palaeoclimatology, Palaeoecology,* 191(2), 243–262. doi: 10.1016/0031-0182(02)00717-4

Kawai, T., Kano, A., & Hori, M. 2009. Geochemical and hydrological controls on biannual lamination of tufa deposits. *Sedimentary Geology*, 213(1-2), 41-50. doi: 10.1016/j.sedgeo.2008.11.003

Kazmierczak, J., Fenchel, T., Kuhl, M., Kempe, S., Kremer, B., Lacka, B., & Malkowski, K. 2015. $CaCO_3$ precipitation in multilayered cyanobacterial mats: clues to explain the alternation of micrite and sparite layers in calcareous stromatolites. *Life*, 5(1), 744-769. doi: 10.3390/life5010744

Le Roux, F.G., 1989. The lithostratigraphy of Cenozoic deposits Along the South-East Cape Coast as related to sea- level changes. Unpublished MSc dissertation, University of Stellenbosch.

Leybourne, M. I., Betcher, R. N., McRitchie, W. D., Kaszycki, C. A., & Boyle, D. R. 2009. Geochemistry and stable isotopic composition of tufa waters and precipitates from the Interlake Region,

Manitoba, Canada: Constraints on groundwater origin, calcitization, and tufa formation. *Chemical Geology*, 260(3-4), 221-233. doi: 10.1016/j.chemgeo.2008.12.024

Mata, S. A., & Bottjer, D. J. 2012. Microbes and mass extinctions: paleoenvironmental distribution of microbialites during times of biotic crisis. *Geobiology*, 10(1), 3-24. doi: 10.1111/j.1472-4669.2011.00305.x

Mucci, A., & Morse, J. W. 1983. The incorporation of Mg^{2+} and Sr^{2+} into calcite overgrowths: influences of growth-rate and solution composition. *Geochemica at Cosmochimica Acta*, 47(2), 217-233. doi: 10.1016/0016-7037(83)90135-7

Pedley, H. 1990. Classification and environmental models of cool freshwater tufas. *Sedimentary Geology*, 68(1-2), 143-154. doi: 10.1016/0037-0738(90)90124-C

Pedley, M. 1992. Freshwater (phytoherm) reefs: the role of biofilms and their bearing on marine reef cementation. *Sedimentary Geology*, 79(1-4), 255-274. doi: 10.1016/0037-0738(92)90014-I

Pedley, M., Andrews, J., Ordonez, S., del Cura, M. A., Martin, J. G., & Taylor, D. 1996. Does climate control the morphological fabric of freshwater carbonates? A comparative study of Holocene barrage tufas from Spain and Britain. *Palaeogeography, Palaeoclimatology, Palaeoecology*, 121(3-4), 239-257. doi: 10.1016/0031-0182(95)00080-1

Perissinotto, R., Bornman, T. G., Steyn, P.-P., Miranda, N. A. F., Dorrington, R. A., Matcher, G. F., Strydom, N., Peer, N. 2014. Tufa stromatolite ecosystems on the South African south coast. *South African Journal of Science*, 110(9–10), 1–8. doi: 10.1590/sajs.2014/20140011

Perri, E., Tucker, M. E., & Spadafora, A. 2012. Carbonate organo-mineral micro- and ultrastructures in sub-fossil stromatolites: Marion lake, South Australia. *Geobiology*, 10(2) 105-117. doi: 10.1111/j.1472-4669.2011.00304.x

Piper, D. Z., & Bau, M. 2013. Normalized rare Earth elements in water, wediments, and wine: Identifying sources and environmental redox conditions . *American Journal of Analytical Chemistry*, 4(10A), 69-83. doi: 10.4236/ajac.2013.410A1009

Plummer, L. N., Wigley, T. M., & Parkhurst, D. I. 1978. The kinetics of calcite dissolution in CO_2-water system at 5° to 60°C and 0.0 to 1.0 atm CO2. *American Journal of Science*, 93, 179-216. doi: 10.1021/bk-1979-0093.ch025

Reid, R. P. P., Visscher, P. T. T., Deche, A. W., Stoltz, J. F., Bebout, B. M. M., Dupraz, C., … DesMarais, D. J. J., 2000. The role of microbes in accretion, lamination and early lithification of modern marine stromatolites. *Nature*, 406(6799), 989–92. doi: 10.1038/35023158

Riding, R. 1999. The term stromatolite: Towards an essential definition. *Lethaia*, 32(4), 321-330. doi: 10.1111/j.1502-3931.1999.tb00550.x

Riding, R. 2000. Microbial carbonates: the geological record of calcified bacterial-algal mats biofilms. *Sedimentology*, 47(1), 179-214.

Riding, R 2006. Microbial carbonate abundance compared with fluctuations in metazoan diversity over geological time. *Sedimentary Geology*, 185(3-4), 229–238. doi: 10.1016/j.sedgeo.2005.12.015

Riding, R. 2008. Abiogenic, microbial and hybrid authigenic crusts: components of Precambrian stromatolites. *Geologia Croatica*, 61(2-3), 73-103.

Riding R. (2011) The Nature of Stromatolites: 3,500 Million Years of History and a Century of Research. In: Advances in Stromatolite Geobiology. *Lecture Notes in Earth Sciences*, 131, 29-74, Springer, Berlin, Heidelberg. doi: 10.1007/978-3-642-10415-2_3

Rishworth, G. M., Perissinotto, R., & Bird, M. S. 2018. Grazer responses to variable macroalgal resource conditions facilitate habitat structuring. *Royal Society Open science, 5(1)*, 171428. doi: 10.1098/rsos.171428

Rishworth, G. M., Perissinotto, R., Bird, M. S., Strydom, N. A., Peer, N., Miranda, N. A., & Raw, J. L. 2017. Non-reliance of metazoans on stromatolite-forming microbial mats as a food resource. *Scientific Reports*, 42614. doi: 10.1038/srep42614

Rishworth, G. M., van Elden, S., Perissinotto, R., Miranda, N., Steyn, P.-P., & Bornman, T. G. 2016a. Environmental influences on living marine stromatolites: insights from benthic microalgal communities. *Environmental Microbiology*, 18(2), 503-513. doi: 10.1111/1462-2920.13116

Rishworth, G., Perissinotto, R., & Bird, M. 2016b. Coexisting living stromatolites and infaunal metazoans. *Oecologia*, 182(2), 539-545. doi: 10.1007/s00442-016-3683-5

Rodriguez-Navarro, C., Jimenez-Lopez, C., Rodriguez-Navarro, A., Gonzalez-Munoz, M. T., & Rodriguez-Gellego, M. 2007. Bacterially mediated mineralization of vaterite. *Geochimica et Cosmochimica Acta*, 71(5), 1197-1213. doi: 10.1016/j.gca.2006.11.031

Rogerson, M., Pedley, H. M., Wadhawan, J. D., & Middleton, R. 2008. New insights into biological influence on the geochemistry of freshwater carbonate deposits. *Geochimica et Cosmochimica Acta*, 72(20), 4976-4987. doi: 10.1016/j.gca.2008.06.030

Saunders, P., Rogerson, M., Wadhawan, J. D., Greenway, G., & Pedley, H. M. 2014. Mg/Ca ratios in freshwater microbial carbonates: Thermodynamic, kinetic and vital effects. *Geochemica et Cosmochimica Acta*, 147, 107-118. doi: 10.1016/j.gca.2014.10.014

Schumann, E.H., 2013. Sea level variability in South African estuaries. *South African Journal of Science*, 109, 1–7.

Schumann, E.H., Perrins, L.-A., 1982. Tidal and inertial currents around South Africa, in: Proceedings of 18th Conference on Coastal Engineering, Cape Town, South Africa. American Society of Civil Engineers, New York, pp. 2562–2580. doi: 10.1061/9780872623736.156

Smith, A. M., & Uken, R. 2003. Living marine stromatolites at Kei River mouth. *South African Journal of Science*, 99(5-6), 200.

Smith, A. M., Andrews, J. E., Uken, R., Thackeray, Z., Perissinotto, R., Leuci, R., & Marca-Bell, A. 2011. Rock pool tufa stromatolites on a modern South African wave-cut platform: partial analogues for Archaean stromatolites. *Terra Nova*, 23(6), 375-381. doi: 10.1111/j.1365-3121.2011.01022.x

Smith, A. M., Uken, R., & Thackeray, Z. 2005. Cape Morgan peritidal stromatolites: The origin of lamination . *South African Journal of Science*, 101(3-4), 107-108.doi: 10.10520/EJC96384

Smith, A., Cooper, A., Misra, S., Bharuth, V., Guastella, L., & Botes, R. 2018. The extant shore platform stromatolite (SPS) facies association: a glimpse into the Archean? *Biogeosciences*, 15, 2189-2203. doi: 10.5194/bg-15-2189-2018

Spadafora, A., Perri, E., Mckenzie, J., & Vasconcelos, C. 2010. Microbial biomineralization processes forming modern Ca:Mg carbonate stromatolites. *Sedimentology*, 57(1), 27-40. doi: 10.1111/j.1365-3091.2009.01083.x

Stumm, W., Morgan, J.J. 1996. Aquatic Chemistry: Chemical Equilibria and Rates in Natural Waters, 3rd ed., Wiley, Pasadena.

Yoshimura, T., Tamenori, Y., Suzuki, A. et al., 2017. Altervalent substitution of sodium for calcium in biogenic calcite and aragonite. *Geochemica et Cosmochimica*, 202, 21-38. doi: 10.1016/j.gca.2016.12.003

Appendices

Appendix 1: Macro- and meso-fabric structures of peritidal tufa stromatolites along the Eastern Cape coast of South Africa (see separate file "Appendix 1").

Appendix 2: Modern active microbialite-metazoan relationships in peritidal systems on the Eastern Cape coast of South Africa: Ecological significance and implication for the palaeontologist record (see separate file "Appendix 2").

Sedimentary Geology 359 (2017) 62–75

Contents lists available at ScienceDirect

Sedimentary Geology

journal homepage: www.elsevier.com/locate/sedgeo

Macro- and meso-fabric structures of peritidal tufa stromatolites along the Eastern Cape coast of South Africa

Mark Joseph Kalahari Edwards [a,*], Callum Robert Anderson [a], Renzo Perissinotto [b], Gavin Midgley Rishworth [b]

[a] Department of Geosciences, Nelson Mandela University, P.O. Box 77000, Port Elizabeth, South Africa
[b] DST/NRF SARChI Chair: Shallow Water Ecosystems, Nelson Mandela University, P.O. Box 77000, Port Elizabeth, South Africa

ARTICLE INFO

Article history:
Received 25 May 2017
Received in revised form 23 August 2017
Accepted 24 August 2017
Available online 01 September 2017

Editor: Dr. J. Knight

Keywords:
Stromatolite
Tufa
Peritidal
Carbonate
Bacteria
Calcite

ABSTRACT

Stromatolites are rare in modern ecosystems due to factors associated with seawater chemistry or biological competition that restrict their formation. Actively calcifying stromatolites, near the Kei Mouth in the Eastern Cape, South Africa, were discovered in the early 2000s. Similar deposits were later described along a 200 km stretch on the south coast of Port Elizabeth. This study aims to describe the environmental setting, the macro- and meso-structures, as well as the evolution of the deposits near Port Elizabeth compared to other similar formations. Results show that the general environmental setting is consistent amongst peritidal stromatolites, including those described in this study. In all instances stromatolite growth occurs on a wave-cut rocky platform in and around rock pools. Growth is maximal within the intertidal to supratidal zone, as a result of freshwater inflow via emerging mineral springs at the base of landward slopes, and the periodic intrusion of seawater via storm surges or wave splash. In comparison with other systems, the South African stromatolite formations exhibit an additional macro-structure (beachrock/conglomerate) and four previously undescribed meso-structures: wrinkled laminar, laminar flat, rhizoliths, and blistered types. The South African stromatolites are also larger and more concentrated than other peritidal stromatolites, which could be due to this area having more suitable growth conditions.

1. Introduction

Stromatolites are layered organo-sedimentary structures that form from sediment trapping, binding and/or carbonate precipitation as a result of the growth and metabolic action of cyanobacteria (Awramik et al. 1976). These deposits develop in areas where $CaCO_3$ supersaturation is reached (Smith et al. 2011), such as at the sediment water interface in freshwater, marine, and evaporitic environments (Riding 2011). When stromatolites grow, they often form domical or columnar structures (Riding 2011) and have a mineralogy mainly dominated by calcite and occasionally aragonite or Mg-calcite (Forbes et al. 2010). Extant marine stromatolites are a rare occurrence because of depleted ocean calcium carbonate levels as well as competition introduced by eukaryotic organisms (Logan 1961; Eckman et al. 2008).

Actively calcifying stromatolites, near the Kei River Mouth in the Eastern Cape of South Africa, were discovered and described by Smith and Uken (2003). These layered limestone deposits are restricted to locally distributed supratidal rock pools, with high evaporation rates. Light, thicker layers (type 1) contain tightly packed vertical filaments arranged in radiating fans, while dark, thin layers (type 2) consist of horizontal filaments and diatoms which often trap sand and other grains (Smith et al. 2005). According to Reid et al. (2000) climax communities, that include endolithic coccoid cyanobacteria, develop during extended hiatial periods of type 1 growth. These microbial communities form thicker lithified laminae (type 3), by biologically altering the sediment. Type 1 layering is referred to as pioneer growth, while types 2 and 3 are referred to as climax laminae.

Similar deposits were later described on the south coast of South Africa near Port Elizabeth (Perissinotto et al. 2014; Fig. 1). These deposits have been regarded as unique in their nature, due to their occurrence within the intertidal/supratidal zone at the interface between freshwater seeps and marine penetration (Perissinotto et al. 2014).

Tufa is a carbonate-based deposit that typically forms under open-air conditions (exposure to ambient conditions, such as wind and sunlight) in cool freshwater that is permanently or periodically supersaturated with calcium carbonate (Kano et al. 2003). Pedley (1990) described a wide variety of tufa types that included phytoherm framestone and phytoherm boundstone (stromatolitic tufa). The external description of these deposits is similar to the "tufa stromatolites" described by Perissinotto et al. (2014). Here, however, the tufas are located in supratidal to upper intertidal zones that regularly receive seawater

* Corresponding author.
E-mail address: kalahariedwards@gmail.com (M.J.K. Edwards).

http://dx.doi.org/10.1016/j.sedgeo.2017.08.006
0037-0738/

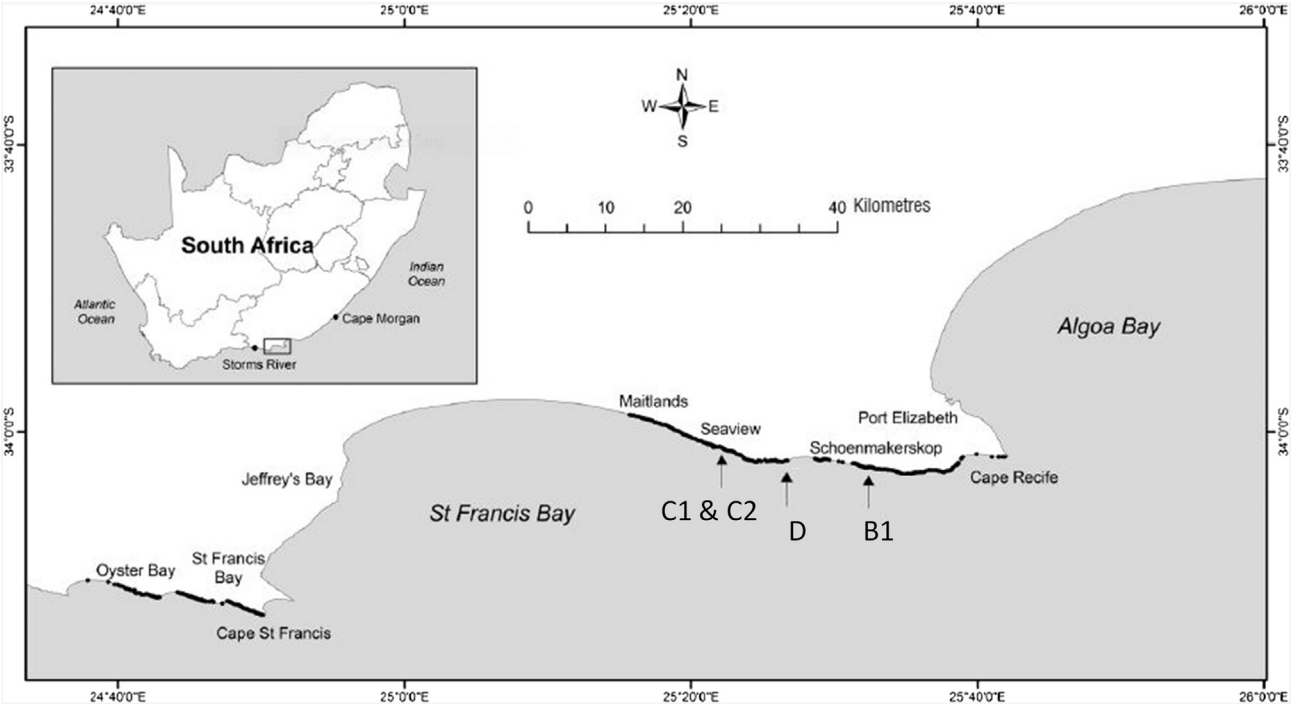

Fig. 1. Study area map showing the location of sites used for sampling and analyses (B1, C1, C2, D). Black points along the coast represent known stromatolite colonies (adapted after Perissinotto et al. 2014).

inflow through wave overtopping at spring high tide or wave splash during storm events (Perissinotto et al. 2014). As these deposits and those at the Kei River Mouth form through the extracellular microbial precipitation of calcium carbonate, introduced by flowing freshwater, they have been classified as "tufa stromatolites" (Riding 2000; Smith et al. 2011; Perissinotto et al. 2014; Rishworth et al. 2016). These tufa stromatolites form waterfall deposits and build barrage pools to trap carbonate-rich freshwater flowing from the base of landward slopes.

Despite their evolutionary importance, stromatolite formation is relatively poorly understood, in terms of the role of microbial activity and the environmental factors that are involved in stromatolite accretion (Reid et al. 2000). An understanding of modern microbial behaviour during stromatolite formation is therefore required (Perissinotto et al. 2014). The microbial activity occuring during stromatolite formation is likely reflected in the fabrics and structures of the resulting deposit. Therefore, studying the growth of these in modern structures may provide key information on the role of microbes in stromatolite formation (Dupraz et al. 2009).

Stromatolites often grow as columns, domes, or mats (Riding 2011), but may coalesce to form larger structures referred to herein as macro-structures. The smaller features (columns, domes, and mats), which make up the macro-structures, are called meso-structures. Meso-structures reflect the growth pattern of stromatolites and typify their surface morphology. Coastal tufa stromatolites have been documented as showing vertical and lateral variations in morphology at the macro-, meso-, and micro- (sub-millimetre) scale (Smith et al. 2011). This study aims to describe the stromatolitic macro- and meso-structures found near Port Elizabeth along the Eastern Cape coast of South Africa. Results are compared to similar deposits found at Western Australia (Forbes et al. 2010), Kei Mouth, South Africa (Smith et al. 2011) and Giant's Causeway, Northern Ireland (Cooper et al. 2013). This study also aims to model and interpret lateral and vertical variations in tufa stromatolite morphology.

2. Materials and methods

2.1. Study site

The study areas occur along the southern stretch of coastline near Port Elizabeth in the Eastern Cape, South Africa (Fig. 1). The coastline is host to at least 540 different stromatolite colonies, of which four were chosen for this study. One of the sites (C1) has been previously studied (Perissinotto et al. 2014) while sites B1, C2, and D represent new study sites. Site B1 (34°2′28.50″S 25°32′17.50″E) is situated at Schoenmakerskop, on the western boundary of the previously studied site B (now referred to as B2). Sites C1 (34°1′3.32″S 25°21′56.48″E) and C2 (34°1′4.72″S 25°22′14.05″E) lie on the coast of Seaview, and site D (34°1′56.54″S 25°24′9.71″E) is found on the Bushy Park farm coastline, near Kini Bay (Fig. 1). The coastline is typified by wave-cut rocky platforms.

2.2. Geological and hydrological setting

The underlying geology at site B and D consists of the deformed metasediments of the Sardinia Bay Formation (Council for Geoscience 2000b, 2000a), the lowermost unit of the Palaeozoic Cape Supergroup. At site B, beach sand and semi-consolidated vegetated calcareous soil covers most of the underlying bedrock. Differential weathering at site D has resulted in two resistant quartzite units forming ridges, while erosion of the argillaceous material (phyllite or meta-wacke) forms the lower-lying gullies.

At site C, the underlying geology consists of deformed meta-greywackes, quartzitic grits, and phyllites of the pre-Cape Gamtoos Group (Council for Geoscience 2000b). The thin (5–20 cm) beds and pervasive axial-planar cleavage dip to the south (Miller et al. 2016). Differential weathering of the bedrock combined with the cleavage results in a series of discontinuous ridges and gullies running obliquely to the coastline. The ridges vary in height from a few centimetres up to

~1.5 m in height, while gullies range in width from a few centimetres to several metres.

The underlying Cape and pre-Cape geology at the three study sites is restricted to the coastal platform, primarily the intra and supra-tidal zones. Formations of the calcareous Algoa Group (Cenozoic) unconformably overly the bedrock. Aeolianites of the middle to late Pleistocene Nahoon Formation fringe the coastline at sites B and D, as well as to the west of site C (Council for Geoscience 2000b, 2000a). Inland of this are the unconsolidated aeolian sands of the Holocene Schelm Hoek Formation (Council for Geoscience 2000b, 2000a). These dunes occur up to 6 km inland and attain a thickness of 140 m (le Roux, 1989). Further inland and presumably beneath parts of the Schelm Hoek Formation, lie the semi- to well-consolidated aeolian deposits of the late Pliocene to early Pleistocene Nanaga Formation (le Roux, 1989).

The groundwater seeps that occur at the three sites all appear to originate on, or just above the contact between the underlying bedrock and the aeolian or beach deposits. The aquifer types feeding these seeps are presumably the fractured aquifers of the Gamtoos and Table Mountain Groups, and the intergranular aquifer of the Algoa Group (Department of Water Affairs n.d.). The Algoa group includes units of calcareous sandstone, limestone, and coquinite (Le Roux 1989). Groundwater influenced by these lime rich coastal sands is reported as having an elevated Ca/Mg HCO_3 component (Lomberg et al. 1996). The groundwater is therefore expected to be enriched in carbonate given it has percolated through these aeolian formations with a high calcite content. The stromatolites form on the southern coastline where the groundwater emerges from the base of the aeolian deposits. The high energy coastline has semi-diurnal tidal phase shifts, with a mean range of 0.5 m at neap tide and 1.8 m at spring tide (Schumann and Perrins 1982), but can reach up to 2 m at times (Schumann 2013).

2.3. Mapping

A combination of photogrammetry and ground-truthing (see below) was used to map the macroscale features of the three sites. Site C1 was mapped using the 2009, 2011, and 2013 high-resolution georeferenced aerial photographs (10 cm pixel resolution) obtained from the Nelson Mandela Bay Municipality. At sites B and D, low-level vertical aerial photographs were taken using a Phantom drone. These were stitched together, using Microsoft's Image Composite Editor, to produce a high-resolution aerial image.

Coloured plastic plates were laid out throughout the site as GPS control points in order to georeference the stitched image. GPS readings were taken with a Magellan Mobile Mapper CX differential GPS instrument.

Each image was taken to the relevant site in order to outline, by hand, each feature to be mapped. All mapped features were thereby ground-truthed using direct field observations. These outlines were used as a reference to build digital maps using Surfer software.

Elevation profiles (15 to 40 m in length) at the sites were surveyed using an Abney level, mounted on a Jacob's staff, to sight elevations on a levelling rod placed at recorded distances along each profile. The elevations recorded are in respect to low tide sea level estimated by observed high and low tide levels.

2.4. Sample collection and preparation

Twenty three samples of varying size (5–35 cm long and 5–15 cm wide) were collected of the various types of growth structures observed. At site B, nine beachrock/conglomerate, three waterfall deposit, and two rhizolith samples were collected. Three rimstone samples were collected from site C. Four discharge apron samples were collected from site D as well as two samples from barrage pool rims. None of the actively growing areas could be sampled as the calcifying deposits were too soft and friable to cut into blocks for examination. The beachrock/conglomerate was sufficiently lithified to sample an area of active growth, but some of the deeper sandy material was not well consolidated and often disintegrated.

All samples were placed in an oven at 150 °C for a minimum of 24 h. They were then cut vertically into two or more pieces depending on the size, in order to expose a cross-section of the stromatolitic structures. Samples that were larger than 15 cm in length were cut more than once. The samples were again dried, impregnated with resin (7:1 Epoxy: Hardener) and then polished for examination. Samples were examined using a hand lens and a Zeiss Stemi DV4 hand sample microscope at up to 32 times magnification. A micro-structure analysis, by thin section, was not performed because the focus of this study was on macro- and meso-structures.

3. Results

3.1. Study sites

Site B1, hereafter referred to as Schoenmakerskop, consists of spring water seeps that flow south over the vertical surface of a 0.5 m high storm cut terrace and onto southward sloping beach sand (Fig. 2).

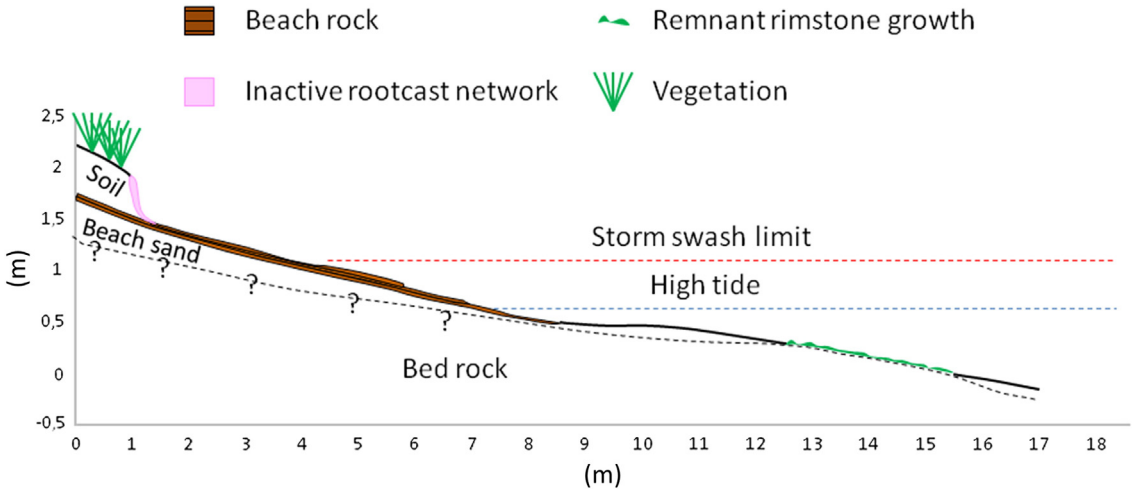

Fig. 2. Cross-section profile of tufa and beachrock deposits at Schoenmakerskop (site B1). Spring water flows (left to right) out and over the vertical storm cut surface to form waterfall deposits and rhizoliths of freshwater tufa (grey). The water then flows onto and through a sandy beach to form beachrock covered by a layer of tufa material (brown). The beachrock extends to below the high tide level but does not progress as far as the low tide level or 0 m elevation. Inactive layered beachrock, possibly formed during a higher sea level, outcrops at the storm cut terrace. Units are in metres. (For interpretation of the references to colour in this figure legend, the reader is referred to the web version of this article.)

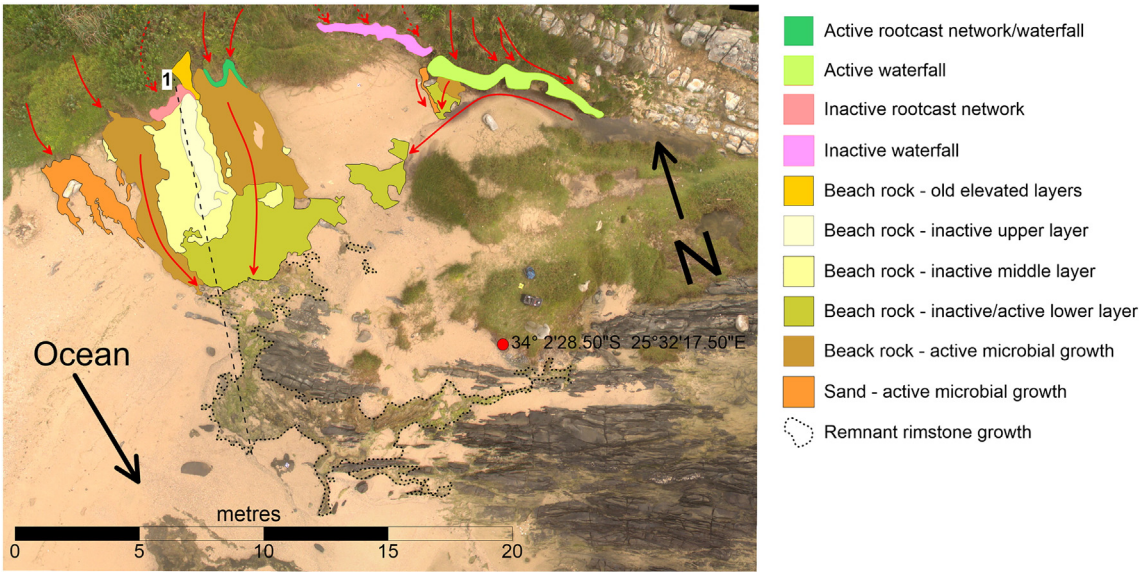

Fig. 3. High resolution aerial photograph map of site B1 showing various types of tufa formation. Red arrows show flow direction, dashed arrows represent inactive flow paths. Dashed black lines indicate location of elevation profile (Fig. 2). (For interpretation of the references to colour in this figure legend, the reader is referred to the web version of this article.)

Laminar type tufa occurs in the waterfall and downstream on the gently sloping beach. An active waterfall deposit occurs on the eastern side of the site where spring water flows over the vertical surface of the storm terrace with no vegetation outcrop (Fig. 3). A small (<1 m^2) section of beachrock occurs below this waterfall where water meets near horizontal ground. On the western edge of the beachrock, sand is covered by a microbial layer. A 15–20 cm deep freshwater pool, which contains no stromatolitic growth, fringes the eastern side of the beachrock here. On the western side of the site, freshwater flows over the vertical surface of the storm cut terrace supporting a prominent vegetation outcrop. The outcropping roots are bound together by a tufa-covering forming a root cast network, known as a rhizolith. Layered beachrock occurs directly below this waterfall and covers an area of >10 m^2 (Fig. 3). Active beachrock occurs on either side of the layered deposit, while the centre is inactive. A microbial layer covers a patch of sand 1 m west of the layered beachrock, where freshwater seeps directly onto gently sloping beach sand.

Sites C1 and C2 are located in front of Seaview, with site C1 (Seaview west) 400 m west of C2 (Seaview East). Seaview west is an exceptionally large section (>100 m in length) of barrage pools and rimstone ponds, which receive freshwater inflow via south flowing groundwater seeps. Back pools form nearest the seepage point, approximately 1.2 m above low tide, and rarely exceed 2 m in diameter and 25 cm in depth. Tufa growth is dominant at back pool margins but does also occur at the pool bottom. Front pools can be up to 1 m in depth and 5 m in diameter. These pools do not exhibit bottom growth, but lateral growth at the margins can be up to 50 cm thick. Shallow (5–20 cm deep) rimstone ponds occur downstream of the front pools and exhibit no bottom growth. Inactive rimstone material is scattered throughout a large central section of the rimstone dams. Remnants of an inactive system are also found in the easternmost part of this site.

Seaview East is a smaller site on the eastern side of a small sandy bay. Freshwater seeps flow south east from a landward slope and into rock pools formed on a wave-cut rocky platform (Fig. 4). Tufa occurs as barrage pool and rimstone deposits. Back pools occur nearest the seepage point, 1.2 m above low tide, and are approximately 20–25 cm deep. Tufa growth is dominant at pool margins, however some growth (<2 cm) occurs at the bottom of the pools. Further seaward the pools

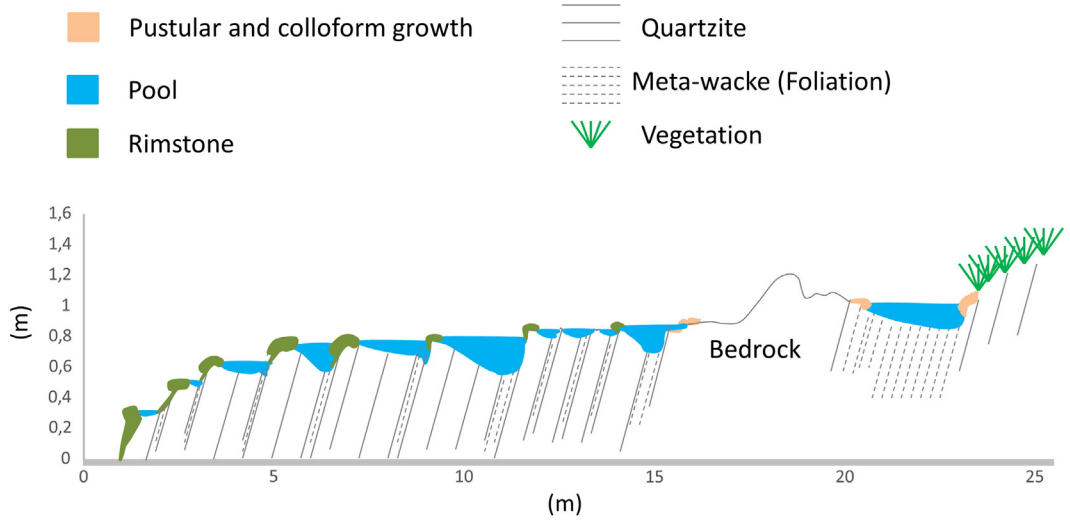

Fig. 4. Cross-section profile of barrage pool and downstream rimstone pools at Seaview (site C2). Spring water flows from right to left over a wave cut rocky platform. Back pools develop nearest the spring water seepage point and exhibit pustular and colloform growth at the pool margins. No bottom growth occurs at these pools. Some thin pustular and blister type mats develop on flat areas covered by a thin layer of freshwater. Downstream pools develop stromatolitic growth at pool rims forming cascading rimstone ponds. Units are in metres.

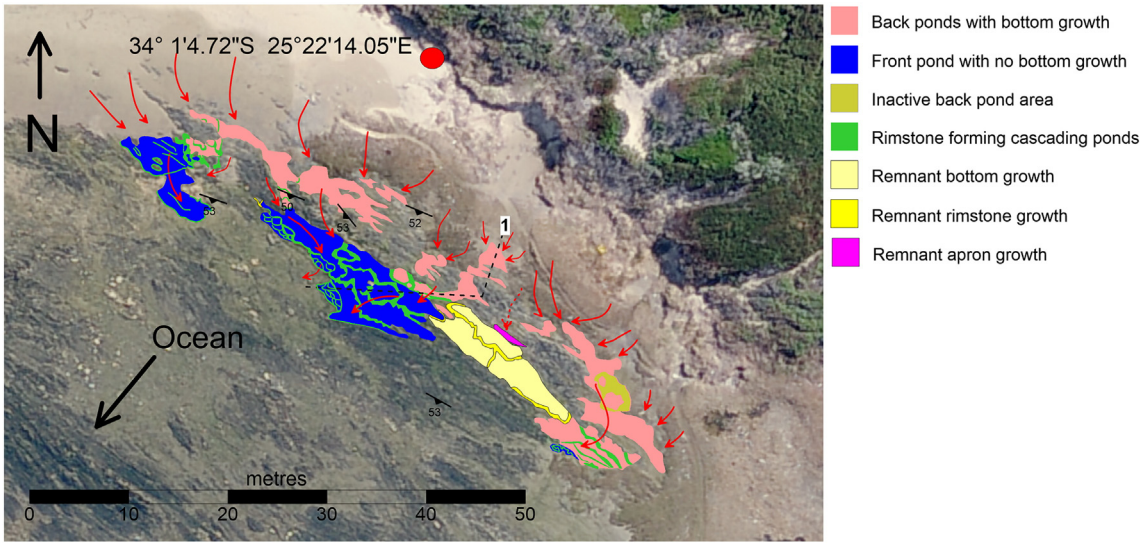

Fig. 5. Google Earth image (2009) map of site C2 showing various stromatolite formations. Red arrows indicate flow direction of freshwater seeps. Dashed red arrows indicate abandoned flow paths. Black dashed line represents location of elevation profile (Fig. 4). (For interpretation of the references to colour in this figure legend, the reader is referred to the web version of this article.)

are shallower (5–20 cm) and form cascading rimstone ponds. The rimstone is active on the east and west sides of the site where freshwater is flowing into the pools (Fig. 5). The 17 m long section in the centre of the site no longer receives freshwater inflow and is inactive (Fig. 5). The active rimstone pools have no bottom growth, but remnant bottom growth is present in the inactive rimstone area.

Site D is located west of Port Elizabeth between Seaview and Schoenmakerskop. It includes a back pool that feeds a large flat apron area, approximately 10 m in diameter, that contains small ponds with bottom growth and deep pools with no bottom growth (Fig. 6). The back pool is approximately 7 m in diameter and contains extensive lateral growth at the margins (Fig. 7). Lateral growth here can be up to 1 m thick and bridges gaps between boulders and pool walls. Smaller (<2 m diameter) back pools and a discharge apron also feed the flat growth area (Fig. 8). Water from the main back pond and the flat area flows via discharge aprons on the steeply dipping quartzite surfaces and into

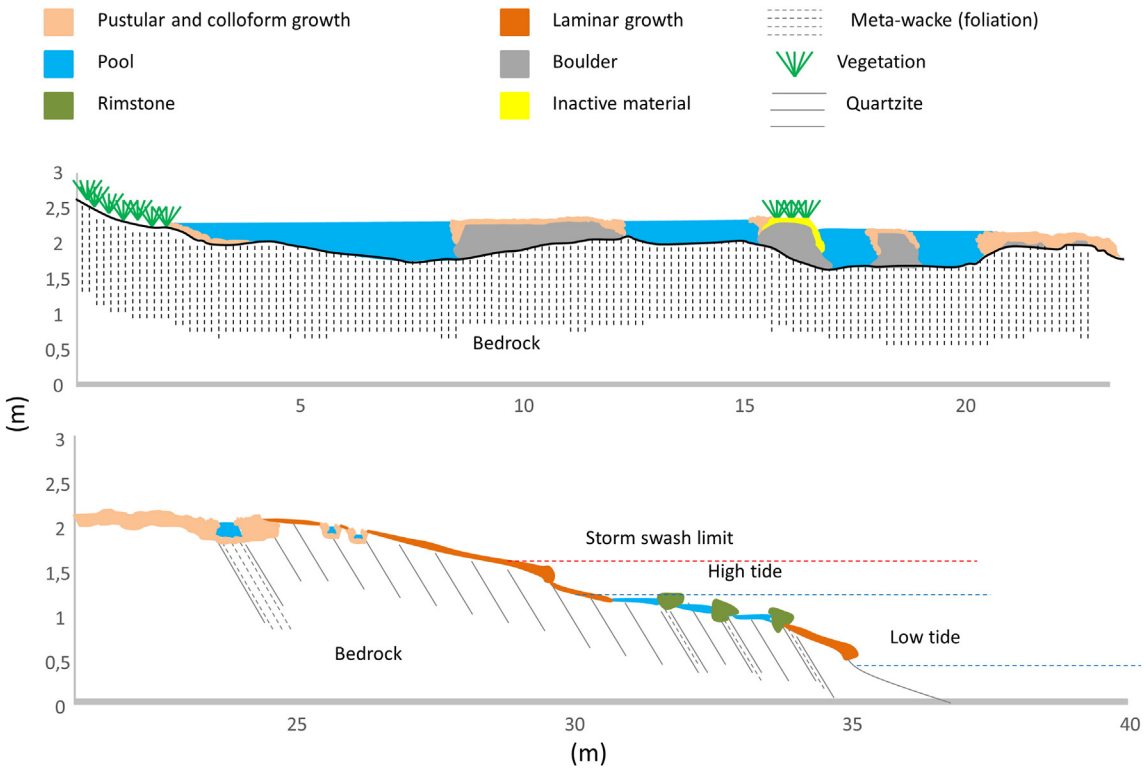

Fig. 6. Cross-section profile 1 of barrage pools and discharge apron at Kini Bay (site D). The first part of the profile is along strike of the underlying bedrock, thus beds appear vertical. Spring water flows (left to right) from a landward bog into relatively large pools which develop pustular and colloform growth (light orange) at pool margins, on pool walls, and on boulders within the pool. Laminar growth (orange) also occurs on flat areas such as boulder tops near the surface of the water and on top of lateral growth from pool walls and boulders. The second part of the profile runs against the strike of the underlying bedrock. Mature pools have developed on a relatively flat area between 19 and 24 m along this profile. Units are in metres.

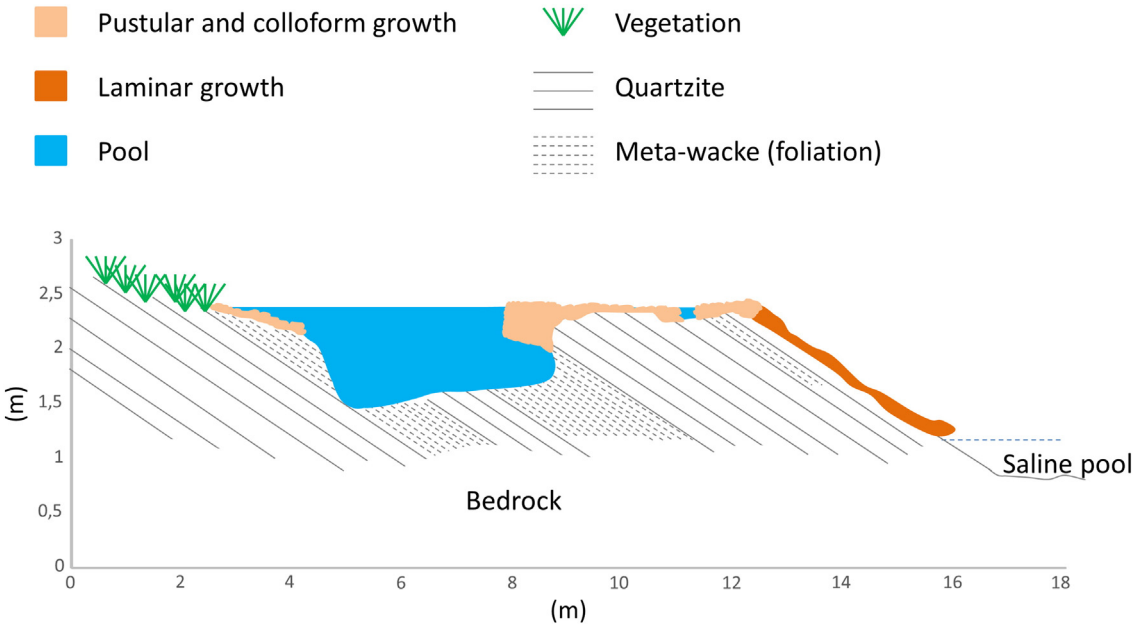

Fig. 7. Cross-section profile 2 of barrage pools and discharge apron at Kini Bay (site D). Pustular to colloform growth occurs in back pools which receive freshwater via spring water seepage from a landward bog.

a marine pool as well as onto a near horizontal quartzite surface. Where freshwater flows into the marine pool (Fig. 7) no growth occurs. However, on the eastern side of the site, water flows onto gently dipping bedrock and forms cascading rimstone ponds (Fig. 6). A remnant discharge apron occurs on the eastern part of the site downstream of an abandoned flow path. West of the site, water seeps through small erosion gullies and joints that form a series of small back ponds and enters the marine ponds via discharge aprons (Fig. 8). Inland of the active back pools is a muddy wetland containing carbonate soil and in places unvegetated areas in which some microbial growth occurs (Fig. 8).

3.2. Macro-structures

The macro-structures observed in this study can be grouped into four categories: barrage pools, discharge aprons, beachrock/conglomerate, and waterfall deposits. Each structure can be distinguished based on a variety of characteristics such as shape, layering, and meso-structures.

The "barrage pool" type consists of back pools and front pools. The back pools occur within the supratidal zone 1.2–2.5 m above low tide and therefore receive seawater via wave overtopping during spring high tide or wave splash during storm events (Figs. 4, 6, 7). In the small shallow back pools bottom and rim growth occurs. In the deeper back pools growth occurs mostly at the pool margins and develops inward (Fig. 9A), ultimately closing the pool (Fig. 10A). Overhangs can also develop on the outer edge of the pool rims (Fig. 10B). The shallow front pools develop as rimstone pools within the upper-intertidal zone (Fig. 4), and as a result receive more seawater and less freshwater than back pools. Growth in these pools is limited to the rims, and develops shallow cascading ponds (Fig. 9B). Rims can mature to develop thicker and higher rims with pronounced lateral growth (Fig. 4). Mature rims will develop inward overhangs and begin to close in a similar fashion to large back pools. Overhangs also develop on the outer edge of these large front pools. Discharge aprons (Fig. 9C) occur where freshwater flows down the inclined bedrock (quartzite or meta-wacke). Growth

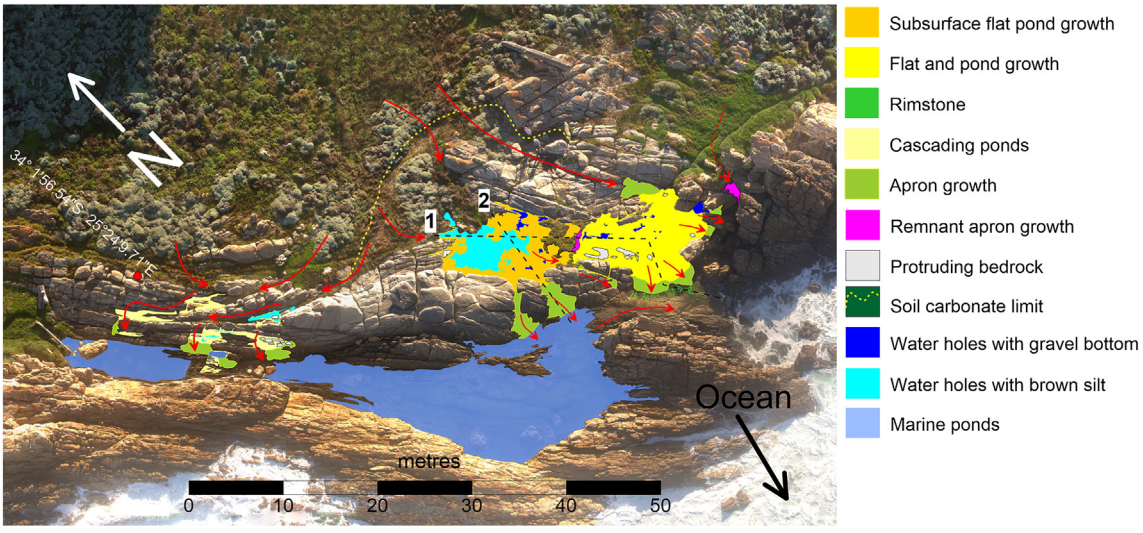

Fig. 8. High resolution orthophoto map of site D. Red arrows indicate flow direction of freshwater seeps. Dashed red arrows indicate abandoned flow paths. Dashed black lines indicate location of elevation profiles – Fig. 6 (1) and Fig. 7 (2). (For interpretation of the references to colour in this figure legend, the reader is referred to the web version of this article.)

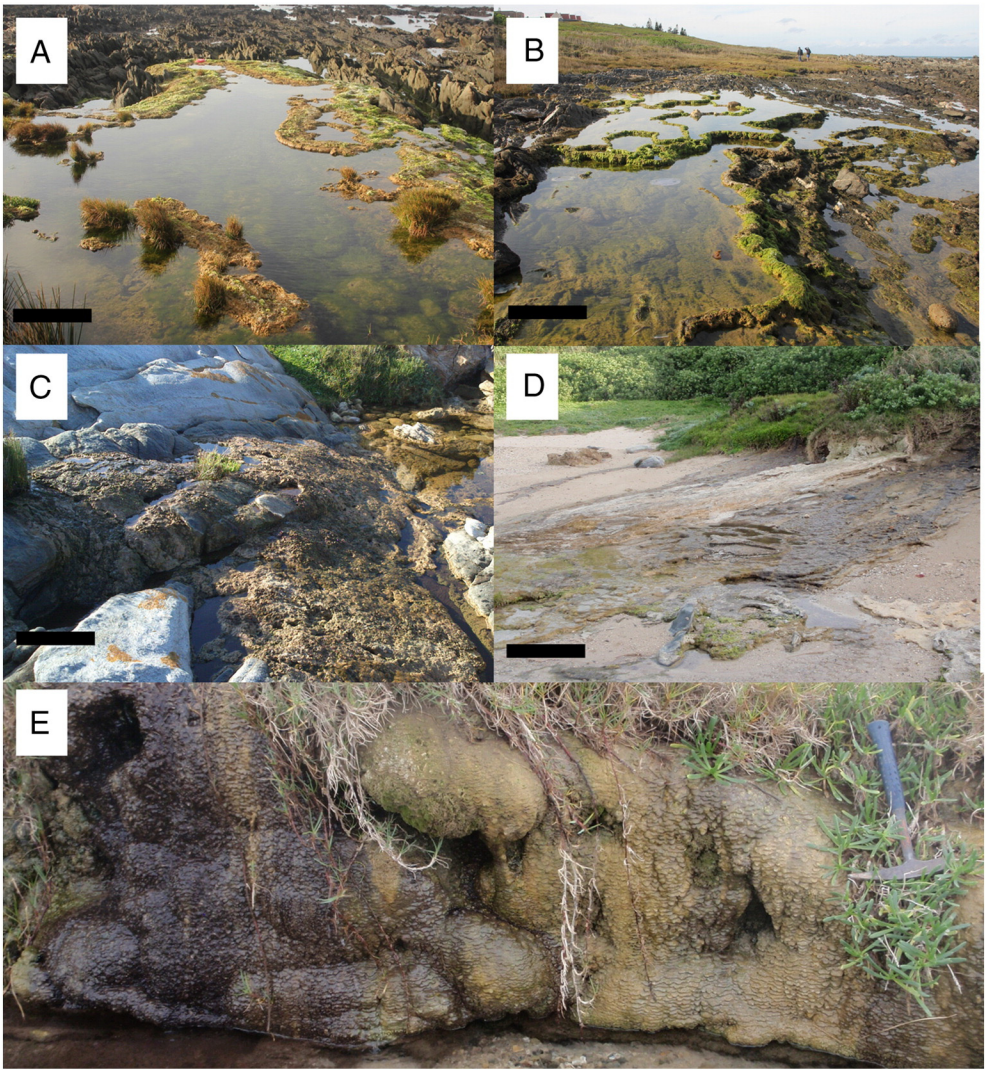

Fig. 9. (A) Barrage pool at site C1 (Photo: Antonia Liber, 16 July 2016), Scale bar indicates 50 cm. (B) Rimstone ponds at site C2, scale bar indicates 50 cm. (C) Discharge apron at site D, scale bar indicates 25 cm. (D) Beachrock formation occurring near a waterfall deposit at site B, scale bar indicates 100 cm. (E) Waterfall deposit at site B, geopick for scale.

is typically thinner than 10 cm but the surface area of a discharge apron is relatively extensive, as water is able to spread out over the rock slope (Fig. 9C).

Beachrock/conglomerate forms when water, high in $CaCO_3$ (Smith et al. 2011; Rishworth et al. 2017), seeps out and flows over and through sand, grit, shells and/or pebbles. The water penetrates the surface and cements grains together as $CaCO_3$ precipitates. Neumeier (1999) suggests that $CaCO_3$ precipitation that forms beachrock may be aided by microbial action. The beachrock/conglomerate here forms elongated layered macro-structures (Fig. 9D). The sand and grit, making up the body of the beachrock, supports a continuum of grain, shell fragment, and pebble sizes. "Waterfall deposits" (Fig. 9E) occur on sub-vertical slopes at the freshwater seepage zone. Growth here is thinner and appears to form on a diverse range of substrates, including vegetation, roots, mud and sand (Fig. 3). This type of growth is more similar to freshwater tufa than tufa stromatolite.

The internal fabric of waterfall deposits is mottled and discontinuous (Fig. 11A). The layering appears disrupted (Fig. 11A), possibly due to erosion by water flowing through the deposit during periods of increased water flow. Despite the lack of continuous layering in the sample, a continuous micro-algal layer is present at the subsurface of waterfall deposits (Fig. 11A). A similar micro-algae layer is also present at the subsurface of beachrock (Fig. 11B).

3.3. Meso-structures

Smith et al. (2011) described three distinct stromatolite meso-structures; pustular formations, colloform growth, and columnar deposits. All three of these medium scale structures are observed in the study areas. Four additional types were identified: wrinkled laminar, laminar flat, rhizoliths, and blistered type. Smith et al. (2011) also described a rimstone morphology, which is described herein as a meso-structure. The rimstone type is an early stage of barrage pool rims but has its own distinct meso-fabric before it matures and develops into a barrage pool rim meso-fabric type.

Pustular formations (Fig. 12A) are comprised of small (0.5–2 cm wide) irregular shaped nodules which often grow on discharge aprons or at the shallow margins of barrage pools. Deeper parts of barrage pools, pool walls, and boulders within the pool often display colloform growth (Fig. 12B). This type of growth has an interconnected bulbous appearance similar to that of malachite, but the margins are more irregular and often form small tunnels at the junction between three or more "bulbs". Colloform growth has a framboidal-like appearance although it is a meso-structure and not a micro-structure. Columns were only found in a single sample collected from the bottom of the inactive discharge apron at Kini Bay. The columns grew in the space where inclined growth intersected level ground. The columns show regular layering of two

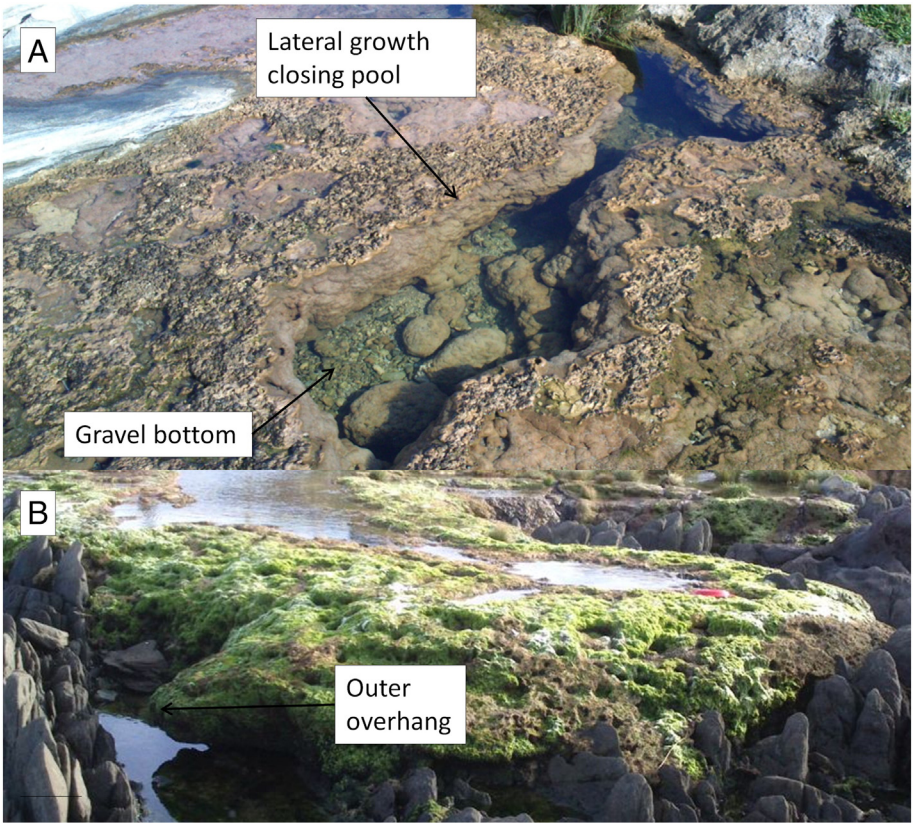

Fig. 10. (A) Back pool exhibiting extensive lateral growth, nearly closing the pool completely, and no bottom growth. (B) Barrage pool showing an outboard overhanging rim.

types of laminae that are continuous between columns (Fig. 12C). Type 1 growth corresponds to the lighter thicker layers, while the darker thinner layers most likely correspond to type 2 growth (Riding 2011). Rimstone has a matted fabric and is usually heavily bioturbated (Fig. 12D), giving it an irregular jagged morphology. This type of structure occurs at front pool rims and has an irregular shape. The typical stromatolite layering is not seen in this type of meso-structure.

The surface of waterfall deposits are typified by small (1–5 cm wide) drooping layers, hereafter referred to as wrinkles (Fig. 13A). These medium scale structures form discontinuous layers on the sub-vertical surface. Wrinkles may represent small layers advancing at different rates down the vertical surface. At Schoenmakerskop, waterfall deposits grade into beachrock (Fig. 13D), with the difference being that waterfall deposits seem to cover loose mud, sand, grit, pebbles and roots, while beachrock formation cements sand, pebbles and shell fragments together. Wrinkles are also observed on the surface of some of the beachrock if it is directly below a waterfall deposit. Laminar flat mat structures occur in well-developed areas of stromatolite growth. This type of meso-scale structure forms relatively continuous layers of type 1 and 2 stromatolite crust. It grows mostly in very shallow areas, discharge aprons or flat surfaces which are periodically covered by water. The internal structure of laminar growth shows relatively flat, continuous, alternating layers of type 1 and type 2 crusts (Fig. 13B). Rootcasts are formed at waterfall deposits that occur in areas that are highly vegetated. The roots and soil are covered in tufa and form a tufa covered network of rhizoliths (Fig. 13C).

In some areas, 1–3 cm wide dome-like structures appear to have burst open at the top resulting in a surface morphology that resembles blistering (Fig. 13D). Small areas at Seaview East and Kini Bay have blistered-type mats. The blistered mats observed in this study occur in flat areas which are often exposed to the air. This exposure to the air could cause the dome-like structures to dry up and burst open, leading to the open blister texture (Gerdesi and Krumbein 1994).

4. Discussion

4.1. Comparison with similar deposits

The macro- and meso-structures observed in this study are similar to those described elsewhere (Smith and Uken 2003; Smith et al. 2005; Forbes et al. 2010; Cooper et al. 2013). Similarities and differences are discussed below.

The physical and environmental description of the Morgan's Bay stromatolites (e.g., Smith and Uken 2003; Smith et al. 2005) reflects the structure of the stromatolites described in this study. However, this study includes four additional meso-structure types. In both instances, stromatolite growth occurs on a wave-cut rocky platform in and around rock pools. Growth occurs within the intertidal to supratidal zone, receiving freshwater via emerging mineral springwater at the base of the landward slopes, and seawater via periodic inundation by marine storms or wave splash. The mineral springwater is believed to be the source of carbonate required for stromatolite formation (Smith et al. 2011). The stromatolite colonies in Morgan's Bay are smaller and more spread out than the colonies found along the coast near Port Elizabeth. According to Perissinotto et al. (2014), at least 540 colonies occur along the coastline west of Port Elizabeth, ranging in size from <1 m^2 to >10 m^2. In contrast, only about 50 stromatolite colonies are found at Morgan's Bay, averaging about 3 m^2 in size (Smith et al. 2011). This difference in size and diversity of stromatolite colonies might suggest that the colonies near Port Elizabeth are older or that they undergo longer periods of active growth. Alternative explanations are that stromatolite colonies at Morgan's Bay are periodically eroded by unstable environmental conditions, or that the freshwater seeping out on the coast near Port Elizabeth is more enriched in $CaCO_3$ than that at Morgan's Bay. A detailed micro-structure and water chemistry study is currently underway in order to test this.

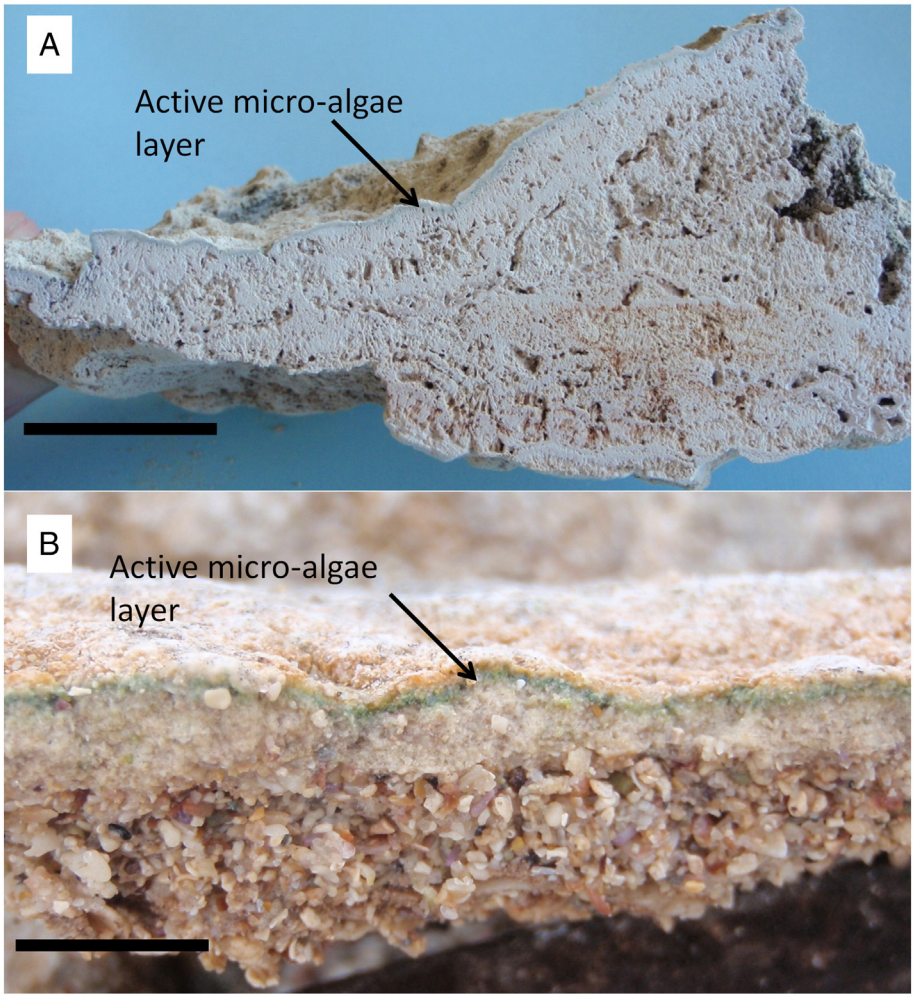

Fig. 11. (A) Waterfall deposit handsample showing mottled, discontinuous fabric and an active microalgae layer, scale bar indicates 2 cm. (B) Active micro-algae (green line), above type 1 (pioneer laminae) crust, in the subsurface of beachrock, scale bar indicates 1 cm. (For interpretation of the references to colour in this figure legend, the reader is referred to the web version of this article.)

Modern stromatolite formation requires a calcium carbonate source, binding/trapping of grains by cyanobacteria, and extreme environmental conditions in order for cyanobacteria to out-compete other organisms (Cooper et al. 2013). The stromatolites that occur at the Giant's Causeway, Northern Ireland, receive calcium carbonate from freshwater flowing from landward basaltic cliffs, underlain by chalk. The water seeps out of carbonate-rich storm swash terraces and into small pools in the supratidal zone of a wave cut rocky platform, where periodic marine water inundation occurs (Cooper et al. 2013). In this study, freshwater flowing through the carbonate rich aeolianites enters the supratidal and intertidal zones, where it meets marine water, providing the environmental conditions suitable to allow cyanobacteria to outcompete other organisms (Rishworth et al. 2017). The deposits in Northern Ireland exhibit similar macro- and meso- structures to those observed in the barrage pool and rimstone ponds in this study, only on a much smaller scale. Cooper et al. (2013) suggested that this very thin growth, at the Giant's Causeway, is because conditions suitable for stromatolite growth have only recently developed or that they are periodically destroyed by incompatible environmental conditions. The fact that the stromatolites along the Eastern Cape coast are significantly larger and more concentrated suggests that here environmental conditions are more favourable for stromatolitic growth. Also, beachrock/conglomerate and waterfall deposits do not appear at the Giant's Causeway, which is significantly colder and wetter than the Eastern Cape coast. This could suggest that these deposits are more sensitive to environmental conditions or that they require specific physical conditions to grow.

Forbes et al. (2010) described a number of tufa deposits, in Western Australia, that have similar structures to those observed in this study. Barrage pools, waterfall deposits, bulbous-like growth, and sheet-like growth are common structures at these tufa deposits. A few of the sites (Canal Rock, Quarry Bay, and Contos Springs barrage pools) exhibit similar features to the deposits described in this study. Barrage pools, which are structurally controlled by the bedrock, and discharge aprons are fed by freshwater seeps and form rimstone dams very similar to the Eastern Cape stromatolites (Forbes et al. 2010). Contos Springs' barrage pools occur in the supratidal zone and receive freshwater via seeps at the base of steep landward limestone slopes, a similar environment to that described here. These tufa deposits are most likely of a similar coastal facies to the deposits found along the Eastern Cape coast.

4.2. Deposition models

Two deposition models ('perched spring line' or 'slope system' and 'barrage pool model') are identified within this study area based on the classification scheme described by Ford and Pedley (1996). Schoenmakerskop represents the perched springline model, Seaview East and West represent the barrage pool model, and Kini Bay reflects a combination of these two end-member models.

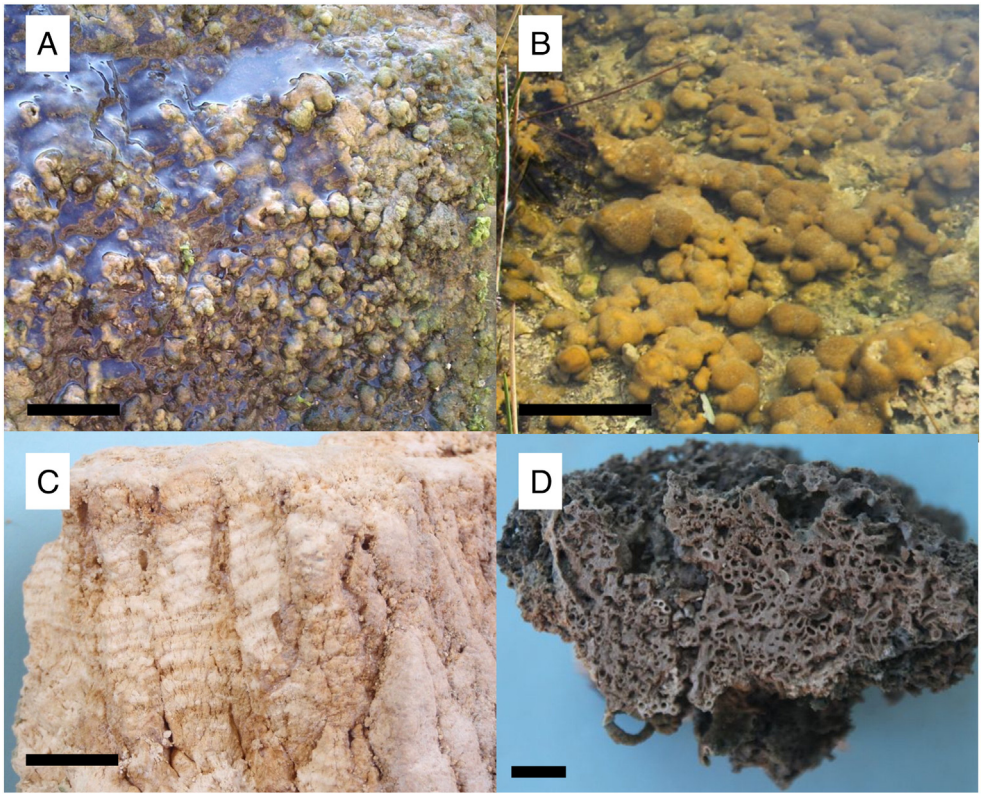

Fig. 12. (A) Pustular growth on discharge apron, scale bar = 5 cm. (B) Colloform growths occurring in back pool, scale bar indicates 10 cm. (C) Columnar growth found at site D, scale bar indicates 1.5 cm. (D) Cut surface of rimstone handsample showing extreme bioturbation and irregular jagged shape, scale bar indicates 1 cm.

Tufa growth in the perched springline model (e.g., Schoenmakerskop; Fig. 2) contains three distinct meso-fabric types: wrinkled laminar mats occurring on waterfall deposits, laminar flat mats occurring on beachrock/conglomerate, and rhizoliths occurring where vegetation roots outcrop in waterfall deposits. The type of growth that occurs seems to be controlled by the underlying slope angle and the substrate over which the spring water flows (Fig. 2). The underlying slope angle affects the flow velocity of the

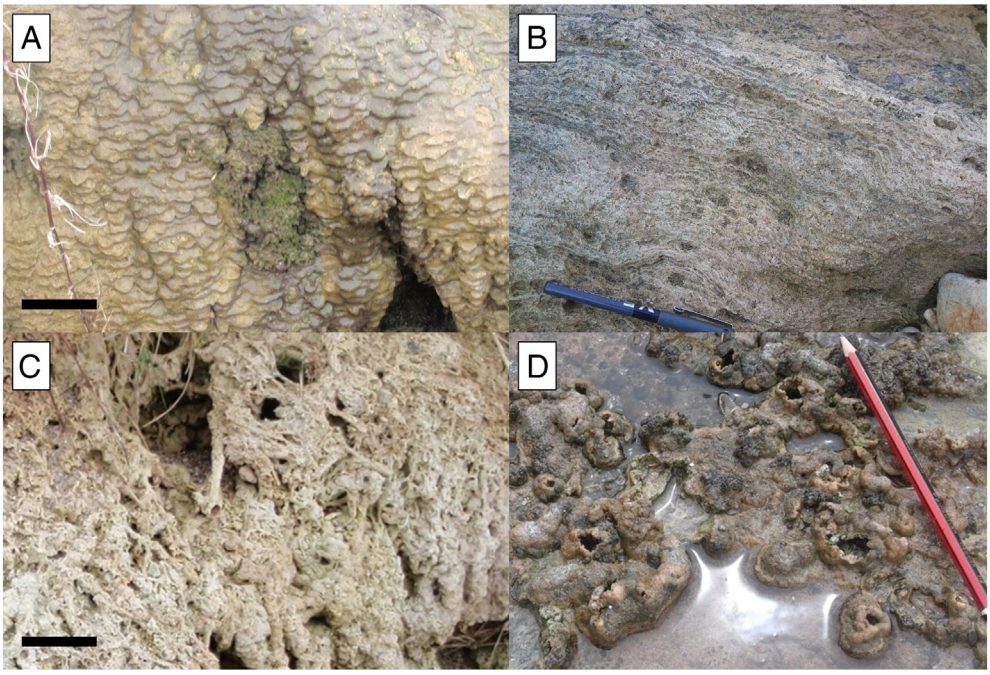

Fig. 13. (A) Wrinkled laminar meso-structures occurring on a waterfall deposit surface at site B1, scale bar indicates 5 cm. (B) Weathered surface of thick laminar flat growth showing alternating layers of type 1 and type 2 crusts, pen for scale. (C) Root cast network covered in tufa material (rhizolith), scale bar indicates 5 cm. (D) Blistered mat at site C1 showing blisters occurring where dome-like structures are aerially exposed (pencil for scale).

spring water, which in turn may control the growth type. Wrinkled laminae form on near vertical slopes where flow is fastest. Rhizoliths develop here too, however, only where spring water flows over exposed roots and vegetation (Fig. 2). Beachrock/conglomerate on the other hand forms on more gentle slopes with a sandy substrate and exhibits a thinner laminar flat tufa covering.

Carbonate precipitation on the steeper waterfall and rhizolith sites is most likely driven by enhanced inorganic CO_2 degassing, due to increased stream flow (Dreybrodt et al. 1992), coupled with microbial activity. The active microbial layers are seen as the green layer in Fig. 11. The layering is somewhat discontinuous, but lamina of different types are scattered throughout the sample. Thin, dark layers (type 2) are rare in waterfall deposits, suggesting that type 3 layering is present, but a more detailed micro-analysis is required to confirm this.

The surface of waterfall deposits is typified by wrinkled laminar formations, but the wrinkles become less obvious on the flat surface at the bottom of the deposit. At the junction between near horizontal shore and the near vertical waterfall deposit, surface morphology changes from wrinkled laminar to more laminar flat (Fig. 14). This marks the limit between beachrock/conglomerate and waterfall deposits, suggesting that wrinkled laminar grades into laminar flat. This gradation could be a function of slope angle and/or water flow velocity. Where wrinkles are seen on the beachrock this could indicate periods of higher flow (Fig. 2).

Small pools can form at the bottom of waterfall deposits but little growth occurs here. If the waterfall occurs directly above a sandy beach, it may form beachrock/conglomerate. Beachrock/conglomerate forms on the gentle slopes, as they are possibly less influenced by inorganic CO_2 degassing. This suggests that the microbial layer observed in beachrock (Fig. 11B) plays an important role in carbonate precipitation. Beachrock/conglomerate structures begin to form when water flows directly onto the beach and develops microbial layering (see area indicated in Fig. 3). As the microbial layer develops it begins to bind the loose sand, pebbles and shell fragments. At this stage, the microbial covering and the grit are very soft and can easily be eroded. If tufa growth continues without erosion, the rock can reach a mature phase. At this stage the sand, pebbles, and shell fragments are strongly cemented together and can resist much stronger erosional forces. Mature beachrock has a strong cement and a well lithified tufa covering (Fig. 15). Water penetrating beneath this layer appears to cement the clasts via calcification, while the layer above seems to be cemented due to biomineralization.

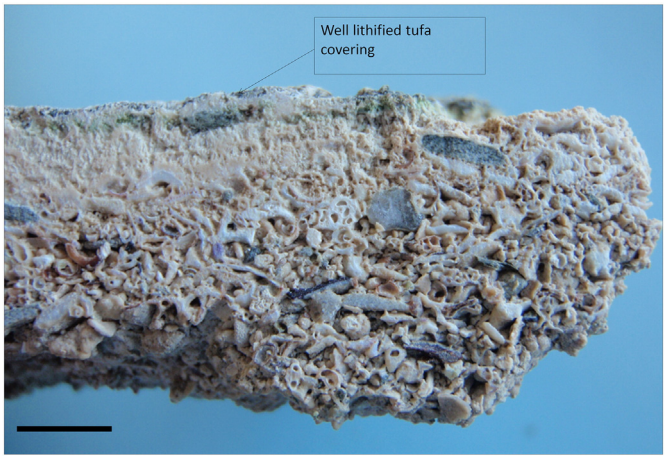

Fig. 15. Beachrock hand sample showing a well lithified tufa covering, scale bar indicates 1 cm.

Neumeier (1999) developed a laboratory model, which reproduced natural conditions of two types of beachrock (seaward-dipping beachrocks and subhorizontal beachrocks). Each set of conditions were reproduced with a microbial influence and separately in nearly sterile conditions as a control experiment. The results of this experiment showed that biomineralization plays an important role in the precipitation of beachrock cement. The experiments which included microorganisms resulted in a wide variety of crystal forms, ranging from 1 to 20 μm in size. The control experiment, however, produced significantly less developed precipitates, suggesting that the cementation process is largely dependent on microbial activity. The biomineralization accounts for micritic precipitation, which is responsible for initial cementation and consolidation of sedimentary grains. This micritic cement is essential to the formation of abiotic prismatic cement during periods of increased water circulation (Neumeier 1999). Therefore, the formation of beachrock can include biogenic and abiogenic precipitation of calcite cement and may require micro-bacterial influence to initiate formation. Given the location on a sandy shore, it is likely that the surface of the beachrock will be periodically covered by sediment. A repeat of the lithification processes would occur, resulting in the distinctive layering observed in the beachrock deposit (Fig. 10).

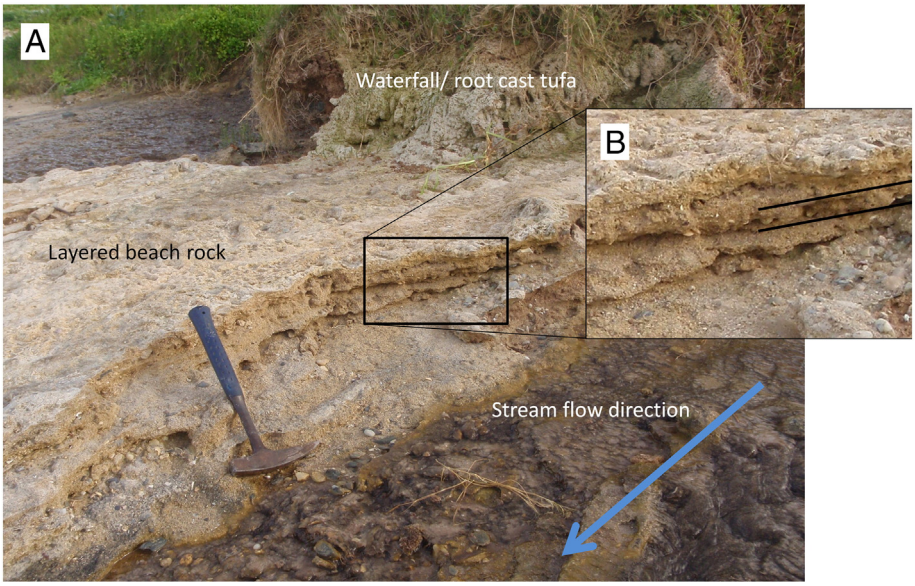

Fig. 14. (A) Layered beachrock below root cast network (geopick for scale). Arrow represents stream flow direction. (B) Close up of beachrock layering.

Pustular, colloform, blister type and rimstone tufa are associated with the barrage pool model (e.g., site C2; Fig. 4). At Seaview west and Seaview east, pustular and colloform growth occurs at back pool margins with the latter usually being observed at greater depths than the former (Fig. 12A, B). This suggests that a continuum exists between the two types of growth. First, the pustular type grows at pool margins and begins to build up pool walls, allowing pool depth to increase. Older pustules (now deeper in the pool) may grow and coalesce to form colloform type mats (Fig. 12B). If pool depth decreases via evaporation or stream diversion, pustules and bulbs are either eroded or become inactive. Blister type mats form outside the pool margins on flat wet areas with laminar and pustular tufa growth. This type of mat is believed to have formed by aerobic decomposition of organic matter underlying laminar flat growth (Gerdesi and Krumbein 1994). Blistered mats have been reported to be dome-like structures filled with methane. Here, however, the dome-like structures have split open and expelled any gas that may have been trapped inside (Fig. 12D).

Between the high-tide and low-tide levels, rimstone tufa develops on slightly elevated bedrock (Fig. 4). This results in the formation of the shallow (5–25 cm deep) cascading front ponds (Fig. 9B). Front ponds with well-developed phytoherms are observed at Seaview west (Fig. 9A). Inward lateral growth of pustular and colloform are found on the vertical surface while laminar and pustular growth occur on the top of the phytoherm. These ponds are regularly inundated by seawater and exhibit stratification during low-tide, exhibiting an upper freshwater lid and a saline bottom (Perissinotto et al. 2014). The vertical distribution of the bottom ponds as well as the lack of bottom growth suggests that high salinity levels prohibit tufa formation. This is consistent with Smith et al. (2011) who found that a salinity >20 prevents calcification and disrupted the microbial assemblage found in tufa stromatolite deposits. Smith et al. (2011) also found that tufa growth in barrage pools is controlled by physico-chemical variations with depth. The lower growth limit of tufa material on pool walls and boulders usually coincides with the depth of the freshwater lid. This would also appear to be the case for the large front ponds in this study.

The barrage pools at Kini Bay (Fig. 6) follow the same general deposition model as those at Seaview. The main differences at Kini Bay are the very well-developed back pools in the centre of the site (Fig. 6). Outflow from the back pools is via discharge aprons, and front rimstone pools with very little growth. Several smaller back pools occur to the east of the main pool. These pools have extensive lateral growth (Fig. 10A; some of which are completely closed) forming a relatively thick layer of tufa stromatolite, which exhibits pustular and colloform growth on pool walls and laminar, pustular and blister type growth above. As with the large front pools, the depth of the lateral growth for the deep back pools appears to be controlled by the periodic influx of sea water during storm events.

The slope system at Kini Bay (Fig. 6) is steeper than that at Seaview and as a result, tufa material forms discharge aprons on seaward dipping quartzite beds. The discharge aprons consist mainly of laminar flat growth with some small patches of pustular and blister type mats. These deposits can form by overtopping of barrage pools (Fig. 7), or by freshwater seeping directly onto the dipping quartzites (Fig. 9C). The bottom limit of this apron is thickest and extends outward over the top of saline water (Fig. 7). The lower limit of this apron is controlled by the water level of the saline pool.

Some pools (e.g., Kini Bay) have a layer of very fine brown material covering their floor (Fig. 16). This material could be fine clay and/or humic acid being brought in by the flowing freshwater. This brown substance sometimes covers tufa material and appears to temporarily prevent growth. If this material is deposited around the edges of bulbs or pustules it may prevent outward growth, but still allow upward growth to continue, thus forming columns. Supporting this hypothesis is that the only example of remnant columnar growth was found at Kini Bay. Here a landward wetland is situated, which produces fine muddy material that may represent the source of the fine brown substance.

Fig. 16. Photograph of fine brown material covering a pool bottom at Kini Bay, pencil for scale (Site D). (For interpretation of the references to colour in this figure legend, the reader is referred to the web version of this article.)

4.3. Evolution of peritidal stromatolite pool systems

The model for barrage pool and rimstone pond evolution can be separated into two types: back pool evolution (Fig. 17A) and front pool evolution (Fig. 17B). Back pools occur in the supratidal zone (e.g., Fig. 7), where freshwater is trapped by local depressions. The pools are often structurally controlled by outcropping bedrock and erosional surfaces (e.g., Fig. 4). Growth begins as pustular and colloform growths at pool margins and on boulders on the pool floor. As growth continues, pustular and colloform growths at pool margins coalesce to form pool rims (Fig. 13D). Some areas which are periodically covered by water can form a blistered mat-type growth. The rims continue growing with most of the growth occurring laterally, towards the pool centre forming inward overhangs (Fig. 9A). Inward rims eventually grow to cover the entire pool, thereby closing it off and trapping water inside a pocket-like structure (Fig. 10A). Growth on the pool walls underneath inward overhangs results in this “pocket” of water being significantly smaller than the original pond.

The front pools grow and evolve in a similar way to back pools (Fig. 17). In the early stage, at low-tide, freshwater collects in shallow pools formed by the differential weathering of the bedrock. Rimstone tufa begins to form where the freshwater overtops the low ridge. With time, more growth occurs, thereby forming thin, heavily bioturbated rims (Fig. 12D). As the rims thicken and increase in height, the pools will show salinity stratification during low tide which results in an inward developing overhang. The saline layer also prevents bottom growth. At this point more freshwater is trapped and the phytoherms change character, supporting pustular and colloform growth on vertical surface walls and laminar and pustular on the top. This change could be due to the variable water chemistry brought about by trapping freshwater. The freshwater may deter communities of burrowing marine organisms from the rimstone. At the mature stage growth eventually closes the entire system (Fig. 10A). As the phytoherms grow upward, overhangs will develop outboard the pools (Fig. 10B). As with the discharge aprons at Kini Bay, the base level of the outboard overhang is controlled by marine water that regularly inundates it.

The front pools can be abandoned before they reach a mature closing stage. This could be because of new rims developing up-stream or channels being eroded into the phytoherm and diverting freshwater flow elsewhere. The inactive area in the centre of Seaview west and the remnant pools at Seaview east appear to have developed as the groundwater seeps were diverted elsewhere. Channels likely formed by erosional processes also develop on mature rims and divert freshwater to a different area where a new system of pools may form. The erosion appears to be a result of the freshwater slowly dissolving the phytoherm, possibly due to slight CO_2 undersaturation. Alternatively rainwater may cause

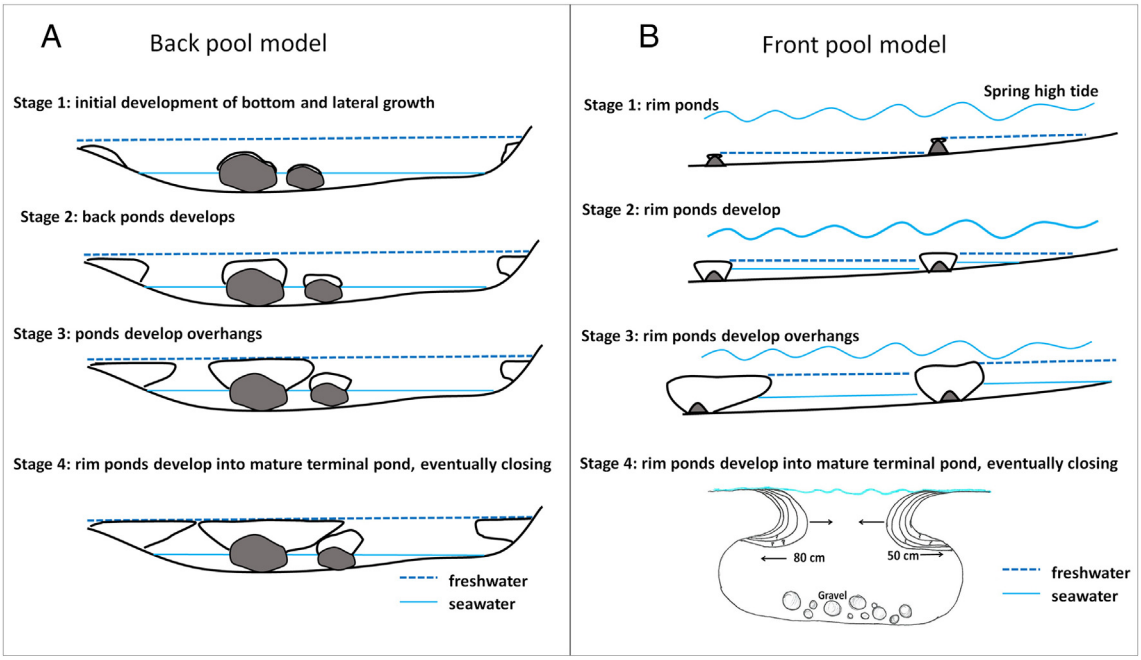

Fig. 17. (A) Diagram showing the different stages of back pool evolution. (B) Diagram showing the different stages of front pool evolution.

the dissolution of stromatolites, since rainwater is slightly acidic. Similar likely processes appear to have occurred at Kini Bay resulting in the inactive remnant rim towards the centre (Fig. 6).

5. Conclusions

The stromatolite deposits described in this study are similar to the deposits found elsewhere in South Africa (e.g., Kei Mouth), Northern Ireland, and Western Australia. All these deposits exhibit comparable macro- and meso-structures and occur in a similar environment to each other. A combination of the perched springline (slope system) and barrage pool deposition models described by Ford and Pedley (1996), used to describe the tufa stromatolites in Western Australia, best describes the deposits found along the Eastern Cape coast of South Africa. A further and more detailed analysis of the micro-structures, mineralogy, and chemistry of these stromatolites may be necessary to confirm a genetic or functional link between the various deposits. A micro-structure and chemical analysis may also provide insight into the microbial activity of these stromatolites and their formation.

A number of conclusions can also be drawn about the growth of tufa stromatolites investigated in this study. At the macro-scale, flow velocity of freshwater and the substrate over which it flows govern which type of macro-structure will form. The barrage pools and rimstone dams are structurally controlled by the local bedrock and form as a result of differential weathering. The amount of seawater entering the system is an important factor for stromatolite growth and is controlled by elevation with respect to sea level. Variation in the amount of seawater versus freshwater inflow can alter the morphology of tufa growth at the macro-scale as well as the meso-scale. Meso-structure morphology on flat and sloped areas varies with flow velocity (as a function of slope angle) and water depth. Stromatolite growth in pools, however, is controlled by vertical variations of physico-chemical properties in the pool water, and only occurs within the freshwater lid.

Acknowledgments

Martin Bentley is thanked for piloting the drone, and the stitching of aerial photos. Nelson Mandela Bay Municipality is also thanked for providing access to their high resolution aerial photographs. This work is based on the research supported by the South African Research Chairs Initiative of the Department of Science and Technology (DST) and the National Research Foundation (NRF) of South Africa. The Claude Leon Foundation is thanked for providing a postdoctoral fellowship to GMR. Any opinion, finding and conclusion or recommendation expressed in this material is that of the author(s) and the NRF does not accept any liability in this regard.

References

Awramik, S.M., Margulis, L., Barghoorn, E.S., Walter, M.R., 1976. Evolutionary processes in the formation of stromatolites. Stromatolites. Elsevier, Amsterdam, pp. 149–162.
Cooper, J.A.G., Smith, A., Arnscheidt, J., 2013. Contemporary stromatolite formation in high intertidal rock pools, Giant's Causeway, Northern Ireland: preliminary observations. Journal of Coastal Research 65, 1675–1680.
Council for Geoscience, 2000a. [Map] 3325CD & 3425AB Uitenhage, 1:50 000 Geological Series. Council for Geoscience, Pretoria.
Council for Geoscience, 2000b. [Map] 3325DC & DD, 3425BA Port Elizabeth, 1:50 000 Geological Series. Council for Geoscience, Pretoria.
Department of Water Affairs (n.d.). Abstract of the Port Elizabeth Brochure. Retrieved October 10, 2010, from https://www.dwa.gov.za/groundwater/maps/pebrochure.pdf.
Dreybrodt, W., Buhmann, D., Michaelis, J., Usdowski, E., 1992. Geochemically controlled calcite precipitation by CO_2 outgassing: field measurements of precipitation rates in comparison to theoretical predictions. Chemical Geology 97, 285–294.
Dupraz, C., Reid, R.P., Braissant, O., Decho, A.W., Norman, R.S., Visscher, P.T., 2009. Processes of carbonate precipitation in modern microbial mats. Earth-Science Reviews 96, 141–162.
Eckman, J.E., Andres, M.S., Marinelli, R.L., Bowlin, E., Reid, R.P., Aspden, R.J., Paterson, D.M., 2008. Wave and sediment dynamics along a shallow subtidal sandy beach inhabited by modern stromatolites. Geobiology 6, 21–32.
Forbes, M., Vogwill, R., Onton, K., 2010. A characterisation of the coastal tufa deposits of south–west Western Australia. Sedimentary Geology 232, 52–65.
Ford, T.D., Pedley, H.M., 1996. A review of tufa and travertine deposits of the world. Earth Science Reviews 41, 117–175.
Gerdesi, G., Krumbein, W.E., Bertrand-Safarti, J., 1994. Peritidal potential stromatolites - a synopsis. In: Monty, C. (Ed.), Phanerozoic Stromatolites II. Kluwer Academic Publishers, pp. 101–129.
Kano, A., Matsuoka, J., Kojo, T., Fujii, H., 2003. Origin of annual laminations in tufa deposits, southwest Japan. Palaeogeography, Palaeoclimatology, Palaeoecology 191, 243–262.
Le Roux, F.G., 1989. The Lithostratigraphy of Cenozoic Deposits along the South-East Cape Coast as Related to Sea-level Changes. Unpublished MSc dissertation. University of Stellenbosch.
Logan, B.W., 1961. Cryptozoon and associate stromatolites from the recent, Shark Bay, Western Australia. The Journal of Geology 69, 517–533.
Lomberg, C.R., Rosewarne, P.N., Raymer, D.A., Devey, D.G., 1996. Research into groundwater abstraction in the Port Elizabeth municipal area. WRC Report No 515/1/97. Water Research Commission, South Africa.

Miller, W., Armstrong, R., de Wit, M.J., 2016. Geology and U/PB geochronology of the Gamtoos Complex and lower Paleozoic Table Mountain Group, Cape Fold Belt, Eastern Cape, South Africa. South African Journal of Geology 119, 147–170.
Neumeier, U., 1999. Experimental modelling of beachrock cementation under microbial influence. Sedimentary Geology 126, 35–46.
Pedley, H.M., 1990. Classification and environmental models of cool freshwater tufas. Sedimentary Geology 68, 143–154.
Perissinotto, R., Bornman, T.G., Steyn, P.-P., Miranda, N.A.F., Dorrington, R.A., Matcher, G.F., Strydom, N., Peer, N., 2014. Tufa stromatolite ecosystems on the South African south coast. South African Journal of Science 110, 1–8.
Reid, R.P.P., Visscher, P.T.T., Deche, A.W., Stoltz, J.F., Bebout, B.M.M., Dupraz, C., Macintyre, I.G., Paerl, H.W., Pinckney, J.L., Prufert-Bebout, L., Steppe, T.F., DesMarais, D.J.J., 2000. The role of microbes in accretion, lamination and early lithification of modern marine stromatolites. Nature 406, 989–992.
Riding, R., 2000. Microbial carbonates: the geological record of calcified bacterial-algal mats and biofilms. Sedimentology 47, 179–214.
Riding, R., 2011. The nature of stromatolites: 3,500 million years of history and a century of research. In: Reitner, J., Quéric, N.-V., Arp, G. (Eds.), Advances in Stromatolite Geobiology. Springer, Berlin Heidelberg, Berlin, Heidelberg, pp. 29–74.
Rishworth, G.M., van Elden, S., Perissinotto, R., Miranda, N.A.F., Steyn, P.-P., Bornman, T.G., 2016. Environmental influences on living marine stromatolites: insights from benthic microalgal communities. Environmental Microbiology 18, 503–513.
Rishworth, G.M., Perissinotto, R., Bornman, T.G., Lemley, D.A., 2017. Peritidal stromatolites at the convergence of groundwater seepage and marine incursion: patterns of salinity, temperature and nutrient variability. Journal of Marine Systems 167, 68–77.
Schumann, E.H., 2013. Sea level variability in South African estuaries. South African Journal of Science 109, 1–7.
Schumann, E.H., Perrins, L.-A., 1982. Tidal and inertial currents around South Africa. Proceedings of 18th Conference on Coastal Engineering, Cape Town, South Africa. American Society of Civil Engineers, New York, pp. 2562–2580.
Smith, A.M., Uken, R., 2003. Living marine stromatolites at Kei River mouth. South African Journal of Science 99, 200.
Smith, A.M., Uken, R., Thackeray, Z., 2005. Cape Morgan peritidal stromatolites: the origin of lamination. South African Journal of Science 101, 107–108.
Smith, A.M., Andrews, J.E., Uken, R., Thackeray, Z., Perissinotto, R., Leuci, R., Marca-Bell, A., 2011. Rock pool tufa stromatolites on a modern South African wave-cut platform: partial analogues for Archaean stromatolites? Terra Nova 23, 375–381.

Journal of African Earth Sciences 153 (2019) 1–8

Contents lists available at ScienceDirect

Journal of African Earth Sciences

journal homepage: www.elsevier.com/locate/jafrearsci

Modern active microbialite-metazoan relationships in peritidal systems on the Eastern Cape coast of South Africa: Ecological significance and implication for the palaeontological record

Gavin M. Rishworth[a,*], Mark J.K. Edwards[a,b], Carlos Cónsole-Gonella[c], Renzo Perissinotto[a]

[a] DST/NRF Research Chair: Shallow Water Ecosystems, Institute for Coastal and Marine Research (CMR), Nelson Mandela University, Port Elizabeth, 6031, South Africa
[b] Department of Geosciences, Nelson Mandela University, Port Elizabeth, 6031, South Africa
[c] Instituto Superior de Correlación Geológica (INSUGEO), Universidad Nacional de Tucumán-CONICET, Miguel Lillo 205, Tucumán, Argentina

ARTICLE INFO

Keywords:
Bioturbation
Ichnology
Neoichnology
Palaeoecology
Refugia
Upper shoreface

ABSTRACT

Modern microbialites are useful partial analogues of their ancient counterparts and especially can provide clues on the conditions to which they were once exposed to. One of the conundrums which has been slow to solve is the role that grazing and burrowing metazoans had towards disrupting the Phanerozoic microbial mats that formed microbialites, especially those of the laminar variety, stromatolites. Here we use a modern occurrence where rare active microbialites along the southern African coastline are forming in direct association with a metazoan community. We show that these associations demonstrate clear evidence of burrows and trace marks from the metazoans, reflecting direct occupation of the microbialite matrix by some taxa. Importantly, these permanent burrows appear to form (mostly) without disruption to the microbialite consolidation, but rather are constructed along the same axis of that of the microbialite. Furthermore, stromatolitic layering is also observed in direct association with active metazoans. This provides further evidence for the refugia hypothesis which suggests that under certain conditions metazoans are not necessarily restrictive of microbialite integrity. This is explained by the selective forces acting against the destructive influence of metazoans because of the refugia benefits (oxygen, predation, exposure) that they accrue from this habitat. This calls for a reinterpretation of some palaeontological observations.

1. Introduction

The Ediacaran-Cambrian boundary reflects a dramatic shift in the structure of shallow aquatic habitats (Bottjer et al., 2000; Mángano and Buatois, 2017), largely attributed to the bioturbation effects introduced by emergent mobile metazoans (Tarhan, 2018). This transition resulted in a shift away from predominantly stable sediment surfaces, which were only oxygenated at the surface by photosynthetic microbial mats, towards well-mixed (and therefore oxygenated) three-dimensional environments. Not only did this change the dynamics of the benthic habitat, but it created unoccupied niches into which evolving, burrowing taxa could enter. Concomitantly, an “explosion” in evolutionary radiation of life occurred, diversifying into all major metazoan lineages known today (Darroch et al., 2018). While the drivers of the Cambrian Explosion are likely diverse (Fox, 2016), burrowing and bioirrigation (through the fluid flow of nutrients and oxygen) played a large role in driving this diversification because of the multitude of niches made available (Herringshaw et al., 2017).

Following this major shift in habitat ecology, well-consolidated microbial mats subsequently became scarce owing to the destructive grazing and burrowing behaviours of diversifying metazoans (Mata and Bottjer, 2012; Riding, 2006). Today, modern microbial mats are mostly well-mixed environments. However, under certain conducive conditions microbial mats can persist as an ordered matrix and, if exposed to a suitable suite of chemical factors, they can accrete as a layered structure. This comprises the biologically-mediated precipitation of calcium carbonate by microorganisms or the trapping and binding of sediment by microalgae to develop these layered accretions (Dupraz et al., 2009; Frantz et al., 2015; Reid et al., 2000). Precambrian conditions would have suited the formation of such structures (known as ‘microbialites’, or in their well-layered form as ‘stromatolites’) and consequently microbialites have been observed extensively in the fossil record as far back as 3,5 bya (Riding, 2000), dominating most shallow aquatic environments. Acting together, the influence of metazoans and a modern decline in oceanic carbonate availability (which is now taken

* Corresponding author.
E-mail addresses: gavin.rishworth@gmail.com, gavin.rishworth@mandela.ac.za (G.M. Rishworth).

https://doi.org/10.1016/j.jafrearsci.2019.02.013
Received 30 December 2018; Received in revised form 5 February 2019; Accepted 6 February 2019
Available online 13 February 2019
1464-343X/

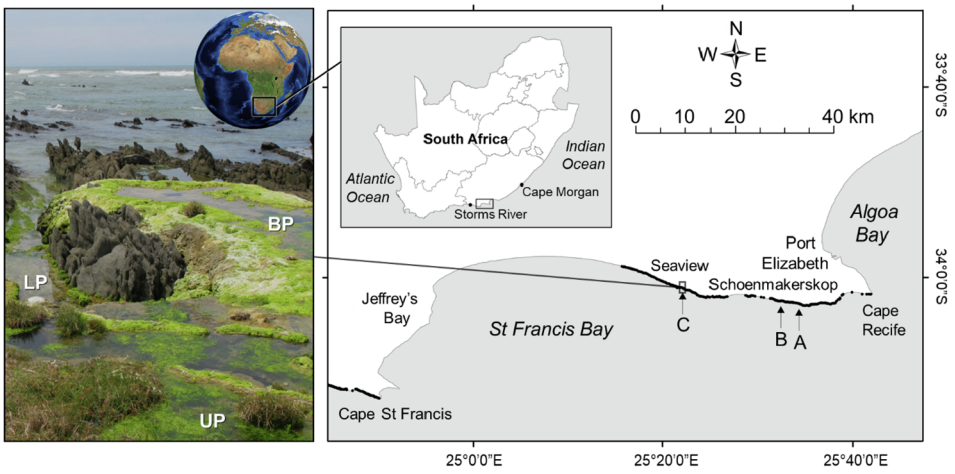

Fig. 1. The location of the peritidal microbialite study sites sampled along the South African coast (sites A, B, and C), as well as an example of a barrage pool (BP) forming at Seaview (site C), showing the location of the freshwater-dominated upper pool (UP) and marine lower pool (LP) regions. Adapted from Rishworth et al. (2017a); inset globe image used with permission from https://pixabay.com.

up by reef- and shell-forming organisms) result in few active extant microbialites (Grotzinger, 1990; Riding, 2006). Only in environments where abrasive (e.g. Exuma Cays, Bahamas: Andres et al., 2009; Bowlin et al., 2012) or hypersaline (e.g. high-altitude lakes in the Argentinean Puna: Farías et al., 2011, 2013; Hamelin Pool, Western Australia: Suosaari et al., 2016) conditions restrict metazoan establishment or where heightened levels of calcium carbonate concentrations result in rapid levels of microbialite accretion (e.g. Cuatro Cienegas, Mexico: Garcia-Pichel et al., 2004) do modern microbialites occur. Given the important predominance of microbialites throughout Earth's history – for example, the cyanobacteria in microbialites contributed to oxygenating the atmosphere ~2 bya (Knoll et al., 2016; Ward et al., 2016) – modern examples are hypothesised to act as partial analogues for their ancient counterparts and possibly provide clues on the conditions to which they were historically exposed (Bosak et al., 2013; Smith et al., 2018).

Covariation between metazoans and microbialites would be unusual given the bioturbation influence of the former, which has comprised the "metazoan-microbialite exclusion" hypothesis (Tarhan et al., 2013). However, both modern (Ricardi-Branco et al., 2018; Rishworth et al., 2016a) and Phanerozoic (Cónsole-Gonella and Marquillas, 2014; Mata and Bottjer, 2012; Pruss and Knoll, 2017) examples suggest that under certain conditions co-occurrence between these usually preclusive taxa can result. Rishworth et al. (2016a) hypothesised that the metazoans occupying the stromatolites off the coast of South Africa were not destroying their infaunal habitat because this provided a refugium against the harsh (and sometimes anoxic) conditions of the peritidal environment. Stable isotope evidence similarly suggested that the metazoans were largely not consuming the stromatolite microalgae, thereby allowing the accretion process to continue relatively unabated (Rishworth et al., 2017b, 2018). Similar refugia hypotheses have been proposed for microbialites, highlighting them as anti-predator (Dinger et al., 2006) or oxygen (Gingras et al., 2011; Mobberley et al., 2015) sanctuaries. Interestingly, the oxygen benefit offered by microbial mats might have driven the evolution of metazoan mobility: organisms that could move between an oxygenated refuge and a food-rich water column would have been at an evolutionary advantage over their sessile counterparts (Gingras et al., 2011).

Few studies have documented the direct metazoan impact in terms of neoichnological traces of burrowing and bioturbation on modern microbialites and the persistence of these impacts remaining in the accreted matrix (e.g. Ricardi-Branco et al., 2018). However, knowledge of these processes would be useful in terms of interpreting the fossil record where similar ichnological features are recorded (Cónsole-Gonella and Marquillas, 2014). Our aim for this study was to investigate the sites in South Africa where metazoan-microbialite coexistence is known (Rishworth et al., 2016a) and provide a preliminary assessment of what structures the metazoans are engineering and also what modern and palaeontological significance this might be having on the microbialites.

2. Local context

This study was confined to peritidal tufa microbialite locations along the South African coastline that have previously been well-studied in terms of geochemistry (Dodd et al., 2018; Rishworth et al., 2017c), geology (Edwards et al., 2017), and ecology (e.g. Rishworth et al., 2016a; Rishworth et al.,2017b, 2018). These sites are located just west of Cape Recife (site A; 34°02′42.13″S, 25°34′07.50″E), at Schoenmakerskop (site B; 34°02′28.23″S, 25°32′18.60″E), Seaview (site C; 34°01′03.16″S, 25°21′56.48″E) (Fig. 1) and Kini Bay (site D; see Edwards et al., 2017). The region is dominated by the influence of the Agulhas Current, with coastal water temperature varying between 10 and 25 °C depending on local upwelling (Goschen et al., 2012). Regular high-energy south-westerly swells berate the coastline, which experiences microtidal (< 2 m) sea-level fluctuations (Goschen et al., 2012). The bedrock geology of the coast in this region is dominated by the Cape Supergroup, while interspersed inland are regular deposits of calcareous sediments of the Algoa Group as well as more-recent aeolian deposits of the Nanaga Formation (Dodd et al., 2018; Edwards et al., 2017; Le Roux, 1989, 1990).

Peritidal microbialites form at locations where carbonate-rich groundwater seeps from the dune cordon (Dodd et al., 2018) and exchanges regularly with ocean storm surges or spring high tides (Rishworth et al., 2017c). Although the age of these structures has not yet been chronologically dated, interpretation of their necessary formative position associated with sea-level (Rishworth et al., 2017c), and given the reconstructed trends in local sea-level stability (Cooper et al., 2018), the age of the active accretions at these sites is taken as approximately 6 ka. Although there is much evidence for pre-Holocene peritidal microbialites (e.g. Mata and Bottjer, 2011), no known association of these structures has been linked directly with groundwater seepage, possibly due to difficulties in assessing the chemical signature of microbialites formed in marine-freshwater convergence zones (C. Dodd, pers. comm.).

Edwards et al. (2017) hypothesised that microbialite evolution at these sites initiates when microorganisms attached to a hard substrate (principally cyanobacteria and diatoms: Rishworth et al., 2016b) accumulate the inflowing groundwater by accreting and trapping sediment, thereby forming rimstone dams which later evolve into deeper barrage pools (sensu Forbes et al., 2010). A variety of mesofabric structures later develop in mature pools (rimstone, pustular, colloform, laminar flat and wrinkled laminar), which seem to arise both as a function of pool features such as depth, position and water flow (Edwards et al., 2017) but also as a result of microorganism

Table 1
Dominant metazoans (following Rishworth et al., 2017a,b) encountered within the peritidal microbialite sites along the southern coastline of South Africa, showing their mean abundance, consistency of occurrence in cores and presence within differing mesofabric types (see Weston et al., 2018), as well as general ecology or behaviour. LF – laminar flat; WL – wrinkled laminar; Co – colloform; Pu – pustular; Ri – rimstone; Mo – mobile; Bu – burrower; Gr – grazer; Pr – predator; De – detritivore; unid. – unidentified.

Class	Order	Species[a,b]	Abundance[b]	Occurence[c]	Mesofabric[c]					Ecology/Habit[a,d]				
			n m^{-2}	%	LF	WL	Co	Pu	Ri	Mo	Bu	Gr	Pr	De
Clitellata	Haplotaxida	unid. (Naididae, Enchtraeidae)	253 ± 478	71	x	x	x	x	x		x			x
Malacostraca	Amphipoda	*Euorchestia rectipalma*	245 ± 436	75	x	x	x	x	x	x		x		x
		Melita zeylanica	37 ± 65		x	x	x	x		x		x		x
		Americorophium triaenonyx	14 ± 82			x	x	x			x	x		x
	Tanaidacea	*Sinelobus stromatoliticus*	197 ± 318	61	x	x	x	x	x		x	x		x
	Isopoda	*Pseudosphaeroma barnardi*	67 ± 329	44	x	x	x	x	x	x		x		x
		Cyathura estuaria	13 ± 37		x	x	x				x	x	x	
Polychaeta	Phyllodocida	*Composetia* cf. *keiskama*	105 ± 127	76	x	x	x	x	x	x	x	x	x	x
Insecta	Diptera	unid. (Chironomidae)	52 ± 106	32	x	x	x	x	x	x		x		
		Dasyhelea sp.	7 ± 25			x		x	x	x		x		
Ostracoda	Pocopida	*Physocypria capensis*	32 ± 187	7	x	x	x	x		x				x
Gastropoda	Littorinimorpha	*Assiminea* cf. *capensis*	27 ± 140	2			x	x		x		x		x

[a] Rishworth et al. (2017b).
[b] Rishworth et al. (2017a).
[c] Weston et al. (2018): per Order.
[d] Rishworth et al. (2016a).

composition (Weston et al., 2019). Other peritidal microbialite macrofabrics (beyond the barrage pool facies) may develop depending on the depositional environment, such as waterfall deposits (on steep slopes), beachrock/conglomerate (on semi-consolidated sediment rather than bedrock) or discharge aprons (at the groundwater outflow), as described in Edwards et al. (2017). Beyond this macro- and mesofabric variability, the salinity gradient forming within the peritidal zone creates distinct regions, such that the barrage pool experiences brackish salinity conditions while the upper pool regions are usually fresh and the lower pools marine (Fig. 1; Rishworth et al., 2017c). The frequent exchange between marine- and freshwater provides the nutrients (phosphorus and nitrogen, respectively) required for the phototrophic microbialite-forming microorganisms to thrive, creating an optimum nutrient convergence zone in the barrage pool where microbialite biomass is maximised (Rishworth et al., 2016b, 2017c). This water exchange also excludes most metazoans that are not halotolerant of the dramatic salinity shifts (Rishworth et al., 2017a).

3. Materials and methods

Sampling occurred in both a structured and opportunistic approach at the peritidal locations surrounding the sites described above. Hand samples were collected from representative macrofabrics of all structures identified by Edwards et al. (2017): waterfall deposits, beachrock/conglomerate, discharge aprons and barrage pools (n = 25). Thin sections were then cut from each of these at locations of interest (n = 25). These were examined and interpreted under a Nikon SMZ25 stereo microscope. Given the brittle nature of some of the samples, resin was first impregnated into the sample, following which a flat section could be cut and used for making the thin sections.

Modern metazoans active within the microbialite matrix were identified and quantified using macrofaunal cores (1.7 cm internal diameter, 2 cm depth: Rishworth et al., 2016a, 2017a) taken from each of the three pool regions (upper, barrage and lower) during a year-long monthly assessment conducted in 2014 at all three sites. This sampling technique ensured that the microbialite matrix was disturbed minimally during the repeated site visits. The data of this assessment are presented elsewhere in detail (Rishworth et al., 2016a, 2017a), but are reinterpreted here with regards to neoichnology. *In situ* photographs of metazoan burrows and features were also taken as they were observed in the field, with the burrow features interpreted against known species ecology of those metazoans identified following the assessment described above.

4. Neoichnology

4.1. Metazoan community

In terms of numerical abundance, the metazoan community inhabiting the active peritidal microbialites on the South African coast is dominated by oligochaetes, amphipods, tanaids and burrowing polychaetes (Table 1). Of these, *Sinelobus stromatoliticus*, *Americorophium triaenonyx* and *Cyathura estuaria* are tube-forming, actively constructing encasements from which they occupy the microbialite matrix. The oligochaetes and polychaetes instead move freely within the matrix, remaining on or below the sediment surface, while the remaining dominant taxa move both within the microbialite crevices and beyond into the water column or adjacent substrate. The persistent metazoan community is dominated by grazers and detritivores, and these largely occupy all mesofabric types (Table 1).

The burrows formed by the metazoans remain as tubular formations within the matrix and also do not appear to disrupt the entirety of the stromatolitic layering, as evidenced by metazoans (e.g. Naididae oligochaetes) observed directly adjacent to such lamination (Fig. 2a). Most burrows tend to form in a vertical orientation, suggestive of tubular growth along the same axis as that of the accreting microbialite (Fig. 2b and c).

4.2. Hand and thin sections

Calcified metazoan tunnels were observed in a number of the hand samples assessed, however, these were primarily observed from rimstone, beachrock or discharge apron macro-structures. Of these, only a single discharge apron sample contained metazoan tunnels (Fig. 3a). The tunnels were much more common in rimstone and beachrock samples. These calcified tunnels appear most commonly within or near cavities in the tufa (e.g. Fig. 3a). However, occasionally, the tunnels do appear integrated with the matrix and on the exterior of tufa (Fig. 3b), as was also observed in situ (Fig. 2). Gastropod shells were also preserved within the surface of the tufa (Fig. 3c). The beachrock hand samples (Fig. 3b) were overall unconsolidated in appearance, containing tufa-encrusted metazoan tunnels within the fine-grained matrix as well as within the rock and shell fragments, the latter of which are loosely cemented by tufa. In contrast to some in situ observations (Fig. 2), all hand samples that showed calcified metazoan tunnels did not display the typical stromatolite layering. However, the layering of

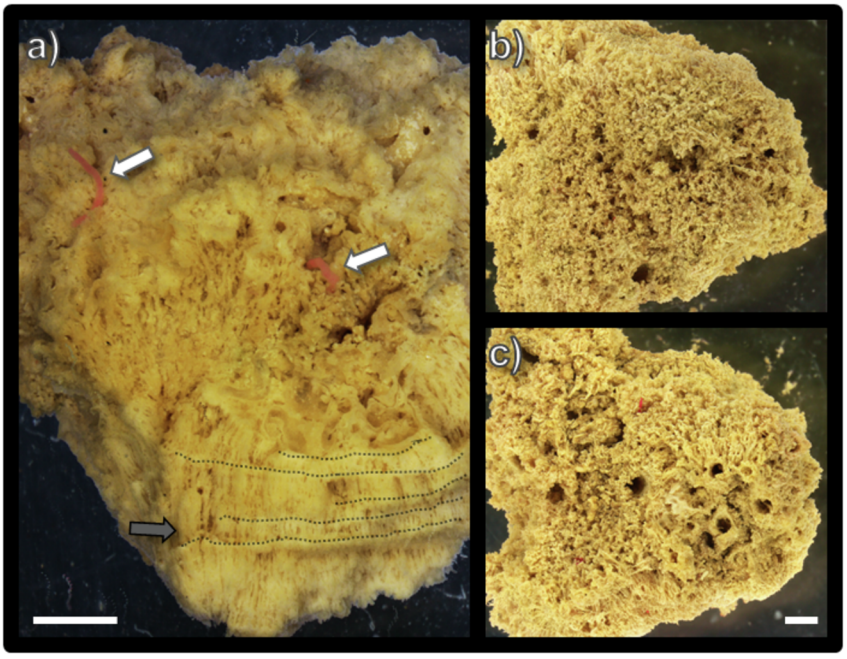

Fig. 2. (**a**) Naididae oligochaetes (white arrows) observed within an active peritidal microbialite, showing the proximal stromatolite layering (superimposed grey lines and arrow) which is not disrupted by the burrowing. Dorsal (**b**) and ventral (**c**) views of the burrows formed by active metazoans are also shown. Scale bars: 1 mm. Taken from figures in Rishworth et al. (2016a).

stromatolites is not always directly apparent without magnification.

The thin-section analysis revealed that metazoan tunnels most commonly appear where there is no layering. In fact the tunnels are usually found within tufa cemented sediments (Fig. 4a and b), filling moulds and casts within the tufa. In thin-section, the tunnels represent tufa-encrusted voids (as evidenced by the central grey-space in the tunnels of Fig. 4) rather than peloids or oncoids. Some thin sections did demonstrate a layered matrix, fitting the description of a stromatolite, together with calcified metazoan tunnels in close proximity (Fig. 4c). While the tunnels do not appear to intersect the layered feature, the close proximity suggests it is possible to have both features occurring simultaneously.

4.3. In situ observations

Burrows observed in the field were common in most mesofabric types, particularly pustular, colloform and laminar flat (Fig. 5). All of these were present with clear, consolidated tunnel entrances, slightly raised above the microbialite surface, suggesting that these are constructed rather than excavated (as simple holes) within the microbialite matrix. Furthermore, burrows were also observed adjacent to clear 'natural' cavities in the microbialite surface (Fig. 5b). The variable size of burrows suggests that these are formed by a variety of taxa, the larger of which are likely attributed to *Cyathura estuaria* and the smaller to *Sinelobus stromatoliticus* or *Americorophium triaenonyx*, all of which are known tube-forming malacostracans. The position of the burrow entrances in situ, as well as cross-section analysis demonstrate single-entrance cavities rather than dual-entrance or u-shaped tunnels.

Although not as yet documented, an impromptu field visit to the peritidal tufa sites in Western Australia (see Forbes et al., 2010) revealed that similar burrows are observed in these systems compared to those in South Africa (Fig. 6).

5. Discussion

5.1. Ecological and environmental significance

This preliminary assessment of the burrows, tube-encasements and bioturbation effects of the metazoans known to coexist with tufa microbialites along the southern coastline of South Africa demonstrates that the matrix is operating as a functional home for many of these metazoans rather than only as an occassional substrate through which the metazoans inhabit. This is cohesive with prior studies which hypothesised that for most metazoans the microbialite matrix is a refuge against the harsh conditions of the peritidal zone: selective pressures likely favour preservation rather than destruction of this habitat from a metazoan perspective (Rishworth et al., 2016a, 2017b; Shinn, 1972). It is an unusual occurrence for microbial mats to not be homogenised by metazoan grazers and burrowers, given the substantial abrasive forces that these mobile taxa often possess (Fenchel, 1998). However, the dynamic salinity regime at these sites (Rishworth et al., 2017c) likely restricts a large portion of metazoans that would otherwise act to disrupt the microbial mat – for example, most marine or freshwater taxa. Additionally, the halotolerant species that can and do co-occur in these systems instead rely on other nutritive sources rather than the microbial mat for food (Rishworth et al., 2017b). In contrast, the limited grazer effect that these metazoans are enacting to bioturbate the matrix may secondarily drive the alternating thick and thin stromatolite lamination (Rishworth et al., 2018). This was hypothesised following the seasonal proliferation and depletion of adjacent macroalgae, the preferred food source for most metazoans (Rishworth et al., 2017b), such that during times of higher macroalgae availability microbialite growth and accretion is optimised (Rishworth et al., 2018).

One obvious grazer assemblage that is largely absent from the South African peritidal microbialite pools are the gastropods, these instead being largely confined to the marine or freshwater margins of these structures (Rishworth et al., 2017a). In other microbialite systems, gastropods are a dominant bioturbating influence (Elser et al., 2005; Garcia-Pichel et al., 2004) such that their behaviour can potentially negate the accretion rate of the microbialites. The limited gastropod presence in the South African microbialites is likely a feature of the salinity tolerance of the local species. Some gastropods shells are found preserved in the microbialite matrix (see Fig. 3c), but these are likely introduced as wash-in from tide and storm surges. Living gastropods are rare in the main microbialite pools (Rishworth et al., 2017a) and consume limited microbialite material (Rishworth et al., 2017b).

Weston et al. (2018) sought to examine how the coexisting metazoans might be structuring the microbialite in terms of mesofabric formation. However, they found little evidence for this top-down role of metazoans (Weston et al., 2018). Instead, the mesofabric variability is

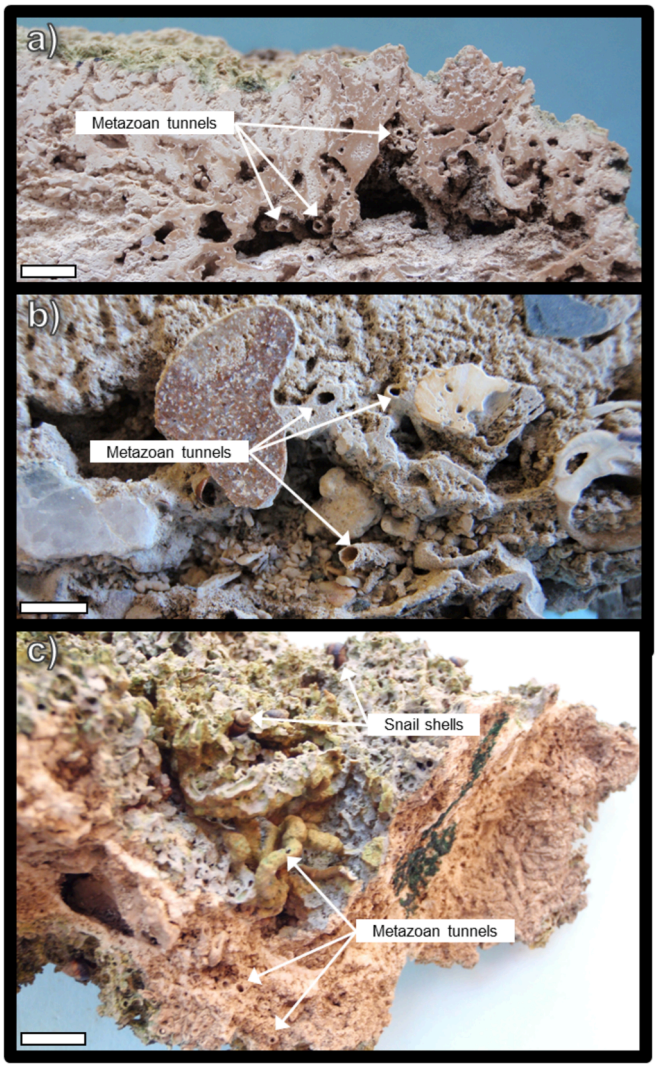

Fig. 3. (**a**) Discharge apron hand-sample showing tunnels, made by metazoans, near a cavity within the tufa. Sample taken from the bottom of a discharge apron which entered a barrage pool at site D. (**b**) Beachrock hand-sample showing metazoan tunnels occurring amongst pebbles, shells, and grit. Sample taken from a beachrock formation at Site B. (**c**). Rimstone hand-sample showing metazoan tunnels on the interior and exterior of the tufa. Gastropod shells are also shown at the top surface of the deposit. Sample taken from a rimstone pool at site C. Scale bars = 1 cm. Photographs: MJKE.

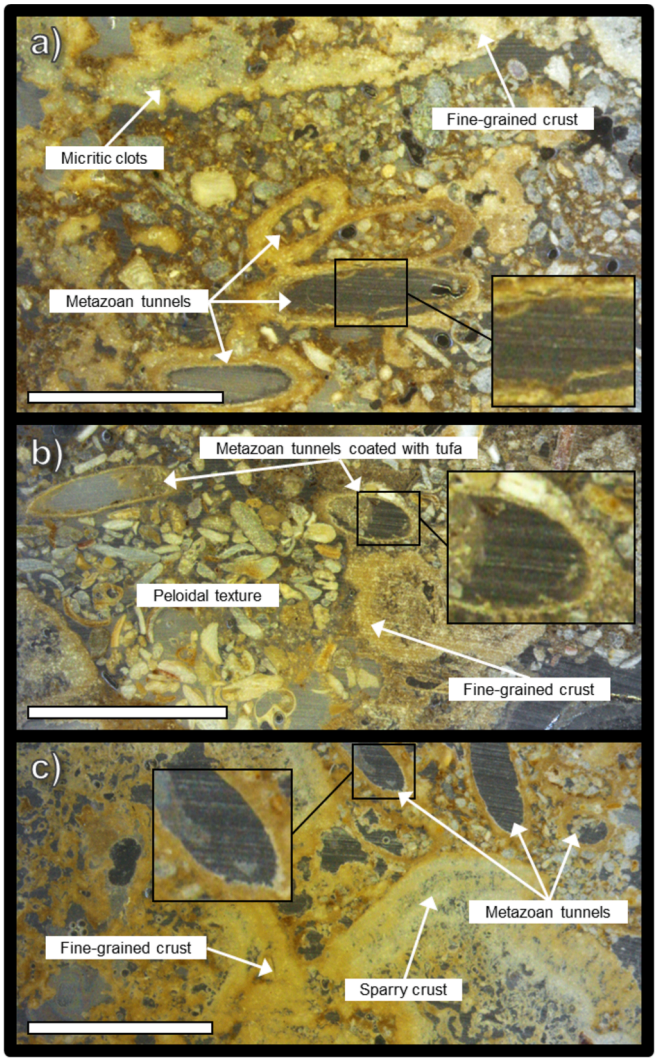

Fig. 4. (**a**) Thin section image (from sample 'FP2') of rimstone growth from site C showing fine-grained crust, sections of tufa-cemented sediments, and tunnels formed by metazoans. (**b**) Beachrock (from sample 'BRC1') showing peloidal texture as well as tunnels formed by metazoans. These tunnels are internally-coated in a layer of tufa. (**c**) Thin section image (from sample 'FP1') of rimstone growth from site D showing a layered sparry structure, tunnels made by metazoans, cemented sediments, and abundant void space. Inset images show a higher-magnification view of the metazoan tunnels, highlighting the tufa-encrusted edge and void, resin-filled grey space in the centre. Scale bars = 5 mm. Photographs: MJKE.

likely driven by bottom-up control, from both abiotic features such as salinity, nutrients and carbonate availability (Dodd et al., 2018; Rishworth et al., 2016b, 2017c), as well as the inherent accretionary properties of the microbialite microalgae and microbial consortia (Weston et al., 2019). We hypothesise that the consolidated nature of the microbialite may in fact be beneficial to those organisms that rely on well-constructed tubes in which to dwell (Table 1). Should the microbial mat be in a constant state of flux and disruption, preservation of these tubes would be limited, and therefore the optimal conditions for these taxa would be reduced. For example, the tube-dwelling tanaid *Sinelobus stromatoliticus*, which thus far has only been observed in the tufa peritidal systems of South Africa (Rishworth et al., in press), relies on a consolidated tube in which to inhabit. Interestingly, a morphologically-similar example of this taxon has been observed in one of the few other microbialites to support coexisting macrofauna (Ricardi-Branco et al., 2018). The *Sinelobus* genus in general requires consolidated, semi-permanent substrate in which to form its burrows (Rishworth et al., in press). The selection pressures on species of this genus would therefore favour limited destruction of the microbialite matrix, hence its relatively high abundance within this habitat.

Those taxa which do not construct tubes but do inhabit the unconsolidated, disrupted parts of the tufa microbialite (e.g. the rimstone, beachrock or colloform mesofabric) would likely opportunise on the crevices and holes naturally formed during the microbialite accretionary process (e.g. the oligochaetes and polychaetes are hypothesised to do this: Fig. 2). The semi-consolidated feature of these mesostructures provides a three-dimensional habitat, thereby creating an environment which offers both habitable space and refuge from predation or ambient conditions, for example. It is likely that these organisms burrow through loose sediment, especially at the marine margins, and then occupy (or partially maintain) the cavities of the tufa as these develop. Subsequent accretionary processes during tufa formation would then later cement together these cavities or calcified tunnels as the metazoans evacuate or the tufa accretes. This kind of strategy was observed in other modern intertidal environments. Shinn

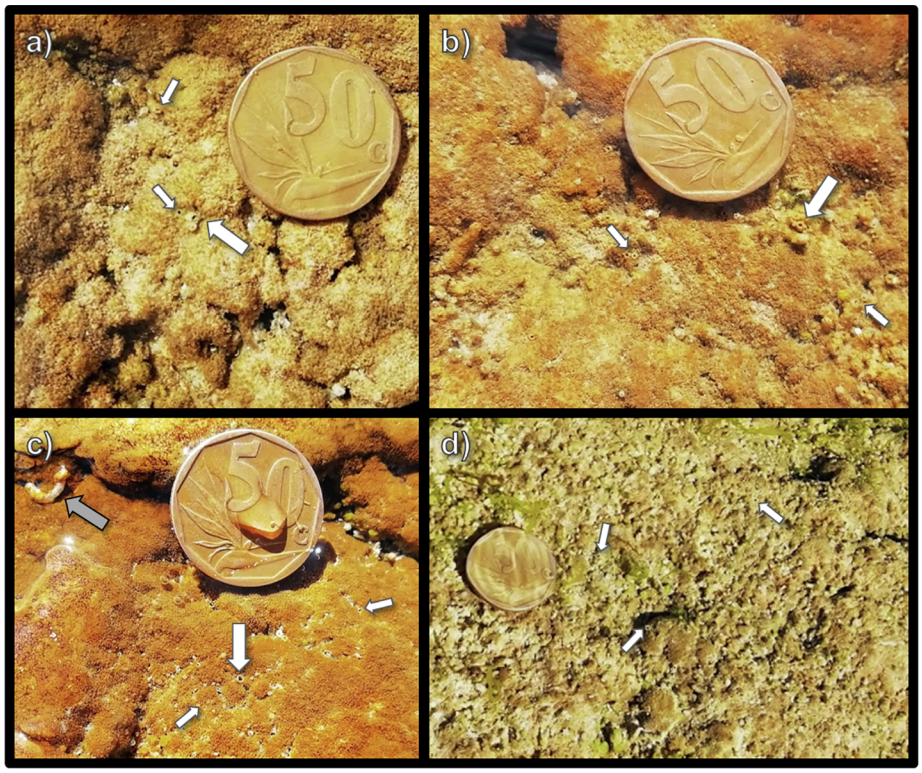

Fig. 5. Ventral view of in situ metazoan burrows at Seaview within pustular (**a**), colloform (**b**) and laminar flat (**c**) mesofabric types, and at Schoenmakerskop within pustular (**d**) mesofabric of active peritidal microbialites along the coastline near Port Elizabeth, South Africa. Tube-like burrows of varying sizes are indicated, likely formed by *Cyathura estuaria* (large white arrows) or *Sinelobus stromatoliticus* and *Americoropium triaenonyx* (small arrows). A hyperbenthic tube of a sessile, filter-feeding polychaete (grey arrow) is also indicated in panel C. Photographs: GMR. Coin width = 22 mm.

Fig. 6. Tube-like metazoan burrows preserved within a spent peritidal microbialite at Quarry Bay, Western Australia. Photograph: GMR. Coin width = 22 mm.

(1972) reported present day stromatolites with noticeable biogenic worm-hosting structures, which have been formed by intergrowth between the two. These worms are likely excavating polychaetes (cf. *Marphysa sanguinea*) (Shinn, 1972).

5.2. Implications for the palaeontological record and concluding remarks

From a stromatolite perspective, these findings provide additional support for the concept that metazoans can both co-occur with stromatolites, but also can form active tubes and burrows within the matrix without always disrupting the layered formation. This observation is not unique to the South African systems (Rishworth et al., 2016a), and has been observed elsewhere (e.g. Ricardi-Branco et al., 2018; Tarhan et al., 2013). Recognition of this has important implications.

Although the palaeontological record suggests the coexistence or even intergrowth between stromatolites and metazoans (see review in Cónsole-Gonella and Marquillas, 2014), the destructive influence of metazoans has long been hypothesised as the Phanerozoic cause of stromatolite (and also microbialite) decline (Awramik, 1971). This concept has been questioned through several phases (Pratt, 1982; Riding, 2006), especially given those periods in the fossil record where the two groups do not demonstrate an inverse relationship (Mata and Bottjer, 2011). Following the post-Cambrian emergence of metazoans, the microbialites have tended to resurge when niches were made available following extinction events which reduced metazoan abundance (Mata and Bottjer, 2012). However, it is now generally accepted that the rise and fall of the microbialites is not solely attributable to the presence of metazoans, but rather other factors such as seawater chemistry and ambient conditions have played a role (Riding et al., 2019). This study, and those also presenting similar observations (Ricardi-Branco et al., 2018), demonstrate modern examples of active microbialites which similarly suggest that there is more to this 'story' than simply the destructive nature of metazoans.

Perhaps the most interesting finding which has emerged from this and other recent studies is that in some cases metazoans may in fact benefit from the non-destructive preservation of the microbialite matrix. This has been noted at the South Africa sites, in terms of the benefit provided by the microbialite matrix from the harsh peritidal conditions (Rishworth et al., 2016a, 2017b), but has also been recognised for other microbialite habitats, in terms of an anti-predation refuge, for example (Dinger et al., 2006). Historically, the foremost emergence of the metazoans and the subsequent features which they evolved may have been linked to some of the niche-benefits which they gained from the microbialites. For example, the oxygen refugia of the microbialites (see Mobberley et al., 2015) likely provided a metabolic benefit for those metazoans that could move between oxygen-rich microbialites and food-rich regions elsewhere (Gingras et al., 2011). Clearly the interpretation of the fossil record in terms of microbialites exclusive of metazoans is not straightforward and should be considered carefully while understanding the environmental setting of the observation in question.

The peritidal environment has often been considered as a harsh

habitat in which to thrive, certainly in terms of modern interpretations (Menge, 2000). Similarly, microbial structures discovered from past peritidal habitats have been interpreted as being too harsh or dynamic to preserve the signatures of metazoan occupation (Mata and Bottjer, 2011). For example, no ichnofossils were observed in the peritidal structures studied by Mata and Bottjer (2011) and this was directly attributed to the destructive forces (wave and sediment dynamics) in this tidal setting being unconducive to their preservation. Our study instead shows that incipient ichnofossils (burrows and tunnels) are clearly preserved in spent (inactive) microbialite facies, which suggests that when suitable conditions are promoted, similar peritidal systems would likely preserve the traces of metazoan activity.

Admittedly, this study remains only a preliminary assessment of the metazoan activity on these tufa microbialite habitats. Further work would be interesting in terms of studying factors such as burrow maintenance, metazoan exclusions and their effects on mesofabric structure, three-dimensional burrow characteristics, nutrient fluxes from metazoan-influenced microbialites, or sediment supply and turnover dynamics. Additionally, those other known systems globally need to be assessed in terms of these features (Cooper et al., 2013; Forbes et al., 2010), especially given the suggestion that similar metazoan influence might be apparent (Fig. 6).

Declaration of interest

The authors declare no conflict of interest.

Acknowledgements

This work is funded by the South African DST/NRF Research Chairs Initiative (grant number 84375). All findings presented are those of the authors and not necessarily attributable to the funding institutions. The Claude Leon Foundation is thanked for a postdoctoral fellowship provided to GMR. Carla Dodd is thanked for providing input on hydrochemistry interpretations.

References

Andres, M.S., Reid, R.P., Bowlin, E., Gaspar, A.P., Eisenhauer, A., 2009. Microbes versus Metazoans as Dominant Reef Builders: Insights from Modern Marine Environments in the Exuma Cays, Bahamas, Perspectives in Carbonate Geology. John Wiley & Sons, Ltd, pp. 149–165.
Awramik, S.M., 1971. Precambrian columnar stromatolite diversity: reflection of metazoan appearance. Science 174, 825–827.
Bosak, T., Knoll, A.H., Petroff, A.P., 2013. The meaning of stromatolites. Annu. Rev. Earth Planet Sci. 41, 21–44.
Bottjer, D.J., Hagadorn, J.W., Dornbos, S.Q., 2000. The Cambrian substrate revolution. GSA Today (Geol. Soc. Am.) 10, 1–8.
Bowlin, E.M., Klaus, J.S., Foster, J.S., Andres, M.S., Custals, L., Reid, R.P., 2012. Environmental controls on microbial community cycling in modern marine stromatolites. Sediment. Geol. 263–264, 45–55.
Cónsole-Gonella, C., Marquillas, R.A., 2014. Bioclaustration trace fossils in epeiric shallow marine stromatolites: the Cretaceous-Palaeogene Yacoraite Formation, Northwestern Argentina. Lethaia 47, 107–119.
Cooper, J.A.G., Green, A.N., Compton, J.S., 2018. sea-level change in southern Africa since the last glacial maximum. Quat. Sci. Rev. 201, 303–318.
Cooper, J.A.G., Smith, A.M., Arnscheidt, J., 2013. Contemporary stromatolite formation in high intertidal rock pools, Giant's Causeway, Northern Ireland: preliminary observations. J. Coast Res. 65, 1675–1680.
Darroch, S.A.F., Smith, E.F., Laflamme, M., Erwin, D.H., 2018. Ediacaran extinction and cambrian explosion. Trends Ecol. Evol. 33, 653–663.
Dinger, E.C., Hendrickson, D.A., Winsborough, B.M., Marks, J.C., 2006. Role of fish in structuring invertebrates on stromatolites in Cuatro Ciénegas, México. Hydrobiol. (Sofia) 563, 407–420.
Dodd, C., Anderson, C.R., Perissinotto, R., du Plooy, S.J., Rishworth, G.M., 2018. Hydrochemistry of peritidal stromatolite pools and associated freshwater inlets along the Eastern Cape Coast, South Africa. Sediment. Geol. 373, 163–179.
Dupraz, C., Reid, R.P., Braissant, O., Decho, A.W., Norman, R.S., Visscher, P.T., 2009. Processes of carbonate precipitation in modern microbial mats. Earth Sci. Rev. 96, 141–162.
Edwards, M.J.K., Anderson, C.R., Perissinotto, R., Rishworth, G.M., 2017. Macro- and meso-fabric structures of peritidal tufa stromatolites along the Eastern Cape coast of South Africa. Sediment. Geol. 359, 62–75.
Elser, J.J., Schampel, J.H., Garcia-Pichel, F., Wade, B.D., Souza, V., Eguiarte, L., Escalante, A.N.A., Farmer, J.D., 2005. Effects of phosphorus enrichment and grazing snails on modern stromatolitic microbial communities. Freshw. Biol. 50, 1808–1825.
Farías, M.E., Poiré, D.G., Arrouy, M.J., Albarracin, V.H., 2011. Modern stromatolite ecosystems at alkaline and hypersaline high-altitude lakes in the Argentinean Puna. In: Tewari, V., Seckbach, J. (Eds.), Stromatolites: Interaction of Microbes with Sediments. Springer Netherlands, Dordrecht, pp. 427–441.
Farías, M.E., Rascovan, N., Toneatti, D.M., Albarracín, V.H., Flores, M.R., Poiré, D.G., Collavino, M.M., Aguilar, O.M., Vazquez, M.P., Polerecky, L., 2013. The discovery of stromatolites developing at 3570 m above sea level in a high-altitude volcanic lake Socompa, Argentinean Andes. PLoS One 8 e53497.
Fenchel, T., 1998. Formation of laminated cyanobacterial mats in the absence of benthic fauna. Aquat. Microb. Ecol. 14, 235–240.
Forbes, M., Vogwill, R., Onton, K., 2010. A characterisation of the coastal tufa deposits of south–west Western Australia. Sediment. Geol. 232, 52–65.
Fox, D., 2016. What sparked the Cambrian explosion? Nature 530, 268–270.
Frantz, C.M., Petryshyn, V.A., Corsetti, F.A., 2015. Grain trapping by filamentous cyanobacterial and algal mats: implications for stromatolite microfabrics through time. Geobiology 13, 409–423.
Garcia-Pichel, F., Al-Horani, F.A., Farmer, J.D., Ludwig, R., Wade, B.D., 2004. Balance between microbial calcification and metazoan bioerosion in modern stromatolitic oncolites. Geobiology 2, 49–57.
Gingras, M., Hagadorn, J.W., Seilacher, A., Lalonde, S.V., Pecoits, E., Petrash, D., Konhauser, K.O., 2011. Possible evolution of mobile animals in association with microbial mats. Nat. Geosci. 4, 372–375.
Goschen, W.S., Schumann, E.H., Bernard, K.S., Bailey, S.E., Deyzel, S.H.P., 2012. Upwelling and ocean structures off Algoa Bay and the south-east coast of South Africa. Afr. J. Mar. Sci. 34, 525–536.
Grotzinger, J.P., 1990. Geochemical model for Proterozoic stromatolite decline. Am. J. Sci. 290-A, 80–103.
Herringshaw, L.G., Callow, R.H.T., McIlroy, D., 2017. Engineering the Cambrian explosion: the earliest bioturbators as ecosystem engineers. In: Brasier, A.T., McIlroy, D., McLoughlin, N. (Eds.), Earth System Evolution and Early Life: a Celebration of the Work of Martin Brasier. Geological Society, London, Special Publications.
Knoll, A.H., Bergmann, K.D., Strauss, J.V., 2016. Life: the first two billion years. Phil. Trans. Biol. Sci. 371, 20150493.
Le Roux, F., 1989. The Lithostratigraphy of Cenozoic Deposits along the South-East Cape Coast as Related to Sea-Level Changes. University of South Africa, Stellenbosch, South Africa.
Le Roux, F., 1990. Algoa group (cenozoic). In: Johnson, M. (Ed.), Catalogue of South African Lithostratigraphic Units. SA Committee for Stratigraphy.
Mángano, M.G., Buatois, L.A., 2017. The Cambrian revolutions: trace-fossil record, timing, links and geobiological impact. Earth Sci. Rev. 173, 96–108.
Mata, S.A., Bottjer, D.J., 2011. Origin of Lower Triassic microbialites in mixed carbonate-siliciclastic successions: ichnology, applied stratigraphy, and the end-Permian mass extinction. Palaeogeogr. Palaeoclimatol. Palaeoecol. 300, 158–178.
Mata, S.A., Bottjer, D.J., 2012. Microbes and mass extinctions: paleoenvironmental distribution of microbialites during times of biotic crisis. Geobiology 10, 3–24.
Menge, B.A., 2000. Top-down and bottom-up community regulation in marine rocky intertidal habitats. J. Exp. Mar. Biol. Ecol. 250, 257–289.
Mobberley, J.M., Khodadad, C.L., Visscher, P.T., Reid, R.P., Hagan, P., Foster, J.S., 2015. Inner workings of thrombolites: spatial gradients of metabolic activity as revealed by metatranscriptome profiling. Sci. Rep. 5, 12601.
Pratt, B.R., 1982. Stromatolite decline—a reconsideration. Geology 10, 512–515.
Pruss, S.B., Knoll, A.H., 2017. Environmental covariation of metazoans and microbialites in the lower ordovician boat harbour formation, newfoundland. Palaeogeogr. Palaeoclimatol. Palaeoecol. 485, 917–929.
Reid, R.P., Visscher, P.T., Decho, A.W., Stolz, J.F., Bebout, B.M., Dupraz, C., Macintyre, I.G., Paerl, H.W., Pinckney, J.L., Prufert-Bebout, L., Steppe, T.F., DesMarais, D.J., 2000. The role of microbes in accretion, lamination and early lithification of modern marine stromatolites. Nature 406, 989–992.
Ricardi-Branco, F., Callefo, F., Cataldo, R.A., Noffke, N., Pessenda, L.C.R., Vidal, A.C., Branco, F.C., 2018. Microbial biofacies and the influence of metazoans in holocene deposits of the lagoa salgada, rio De janeiro state, Brazil. J. Sediment. Res. 88, 1300–1317.
Riding, R., 2000. Microbial carbonates: the geological record of calcified bacterial–algal mats and biofilms. Sedimentology 47, 179–214.
Riding, R., 2006. Microbial carbonate abundance compared with fluctuations in metazoan diversity over geological time. Sediment. Geol. 185, 229–238.
Riding, R., Liang, L., Lee, J.-H., Virgone, A., 2019. Influence of dissolved oxygen on secular patterns of marine microbial carbonate abundance during the past 490 Myr. Palaeogeogr. Palaeoclimatol. Palaeoecol. 514, 135–143.
Rishworth, G.M., Perissinotto, R., Bird, M.S., 2016a. Coexisting living stromatolites and infaunal metazoans. Oecologia 182, 539–545.
Rishworth, G.M., Perissinotto, R., Bird, M.S., 2017a. Patterns and drivers of benthic macrofaunal communities dwelling within extant peritidal stromatolites. Limnol. Oceanogr. 62, 2227–2242.
Rishworth, G.M., Perissinotto, R., Bird, M.S., Pelletier, N., 2018. Grazer responses to variable macroalgal resource conditions facilitate habitat structuring. R. Soc. Open Sci. 5, 171428.
Rishworth, G.M., Perissinotto, R., Bird, M.S., Strydom, N.A., Peer, N., Miranda, N.A.F., Raw, J.L., 2017b. Non-reliance of metazoans on stromatolite-forming microbial mats as a food resource. Sci. Rep. 7, 42614.
Rishworth, G.M., Perissinotto, R., Blazewicz, M., (in press). *Sinelobus stromatoliticus* sp. nov. (Peracarida: tanaidacea) found within extant peritidal stromatolites. Mar. Biodivers..
Rishworth, G.M., Perissinotto, R., Bornman, T.G., Lemley, D.A., 2017c. Peritidal

stromatolites at the convergence of groundwater seepage and marine incursion: patterns of salinity, temperature and nutrient variability. J. Mar. Syst. 167, 68–77.
Rishworth, G.M., van Elden, S., Perissinotto, R., Miranda, N.A.F., Steyn, P.-P., Bornman, T.G., 2016b. Environmental influences on living marine stromatolites: insights from benthic microalgal communities. Environ. Microbiol. 18, 503–513.
Shinn, E.A., 1972. Worm and algal-built columnar stromatolites in the Persian Gulf. J. Sediment. Res. 42, 837–840.
Smith, A., Cooper, A., Misra, S., Bharuth, V., Guastella, L., Botes, R., 2018. The extant shore platform stromatolite (SPS) facies association: a glimpse into the Archean? Biogeosciences 15, 2189–2203.
Suosaari, E.P., Reid, R.P., Araujo, T.A.A., Playford, P.E., Holley, D.K., McNamara, K.J., Eberli, G.P., 2016. Envrionmental pressures influencing living stromatolites in Hamelin pool, shark Bay, western Australia. Palaios 31, 483–496.
Tarhan, L.G., 2018. The early Paleozoic development of bioturbation—evolutionary and geobiological consequences. Earth Sci. Rev. 178, 177–207.
Tarhan, L.G., Planavsky, N.J., Laumer, C.E., Stolz, J.F., Reid, R.P., 2013. Microbial mat controls on infaunal abundance and diversity in modern marine microbialites. Geobiology 11, 485–497.
Ward, L.M., Kirschvink, J.L., Fischer, W.W., 2016. Timescales of oxygenation following the evolution of oxygenic photosynthesis. Orig. Life Evol. Biosph. 46, 51–65.
Weston, R.-L.A., Perissinotto, R., Rishworth, G.M., Steyn, P.P., 2018. Macroinvertebrate variability between microhabitats of peritidal stromatolites along the South African coast. Mar. Ecol. Prog. Ser. 605, 37–47.
Weston, R.-L.A., Perissinotto, R., Rishworth, G.M., Steyn, P.P., 2019. Benthic microalgal variability associated with peritidal stromatolite microhabitats along the South African coast. Aquat. Microb. Ecol. 82, 253–264.